SLHC - PP

Large Hadron Collider Upgrade Preparatory Phase

http://cern.ch/slhc-pp

EDMS nb. **1133541**	Creation Date: 06-August-2010	Version: 1
	Last Update: 3/31/2011 4:43:00 PM	Nb of pages: 70

This document can be found at:

Plasma generation and study of the thermal and vacuum conditions

Authors	Approved by	
A. Castel		
E. Chaudet		
P. Chiggiato		
S. Clement		
J.-F. Ecarnot		
D. Faircloth		
G. Favre		
F. Fayet		
R. Gauthier		
J.-M. Geisser		
M. Haase		
A. Habert		
J. Hansen		
S. Joffe		
M. Kronberger		
D. Küchler		
J. Lettry		
D. Lombard		
A. Marmillon		
J. Marques Balula		
S. Mathot		
P. Moyret		
D. Nisbet		
M. O'Neil		
M. Paoluzzi		
H. Pereira		
L. Prever-Loiri		
J. Sanchez Arias		
C.-S. Schmitzer		
R. Scrivens		
D. Steyaert		
H. Vestergard		
M. Wilhelmsson		

Distribution List

History of changes

Version	Date	Responsible	Modification
0.1	2011-03-24	M. Kronberger	Creation of document
1.0	2011-03-29	M. Kronberger	Full document
2.0	2011-03-30	M. Kronberger	Full document, first revision

Abstract.

The Superconducting Proton linear (SPL) accelerator study requires an ion source operating at 50 Hz repetition rate. The study of a radio frequency (RF) driven hydrogen plasma generator extrapolated from CERN's Linac4-DESY volume ion source to a duty factor suitable for the SPL source is described in this report.

In the SPL plasma generator, the plasma is induced by an RF antenna. A multipole cusp field created by permanent magnets confines electrons in the plasma, reduces plasma losses, and increases the plasma density. The thermal load from the hydrogen plasma and the heat produced by induced ohmic losses in the surrounding materials must be evacuated during operation. The RF coupling efficiency to the plasma, the efficiency of the plasma chamber cooling systems and the plasma characteristics are essential figures of merit of the plasma generator design reported herein.

Starting with the DESY ion source configuration, the temperature distribution in the plasma generator was studied under the assumption of 100 kW RF power dissipated in the plasma for a duty factor of 6%. The obtained temperature distributions showed that numerous parts would be brought well beyond their operational conditions in absence of an efficient cooling system. A list of improvements including the selection of high heat conductivity materials (AlN, Cu), the minimization of heat diffusion barriers by brazing electrical insulators onto conductors, and the implementation of cooling circuits, was proposed. Three-dimensional finite-element models were produced and studied with computational fluid dynamics (CFD), thermal-structural, and electromagnetic simulation codes. After only few iterations, a promising model was obtained and a prototype designed and produced.

For the multipole magnetic cusp configuration, it was aimed to keep the field strength and gradient at the plasma chamber wall similar to that of the DESY source. Two options were proposed and tested: a dodecapole and an octopole magnetic cusp configuration. In both cases, Halbach elements were used instead of standard N-S magnetized magnets in order to increase the field strength inside the plasma volume.

Increasing the RF field to reach a peak power of 100 kW requires better insulation. Air ionization in gaps left between insulation layers and the RF-shielding of permanent magnets and around sharp edges was observed on the first prototype. Simulations showed that rounded edges and a minimum of air gaps are essential design parameters for inductively coupled RF heated plasma generators.

In an inductively coupled system, the induced current is at the origin of the field accelerating the electrons. The first few electron-ion pairs are obtained via an electric discharge in a spark gap that requires a minimal H_2-thickness to be operational according to the Paschen curve. This factor limits the pressure range where plasma can be ignited at low RF power and low repetition rate. When operated at 50 Hz and above an average RF power of 1 kW, the ignition system can be switched off.

A test stand was built to test the plasma generator and its subsystems. All power supplies, water and gas distribution, safety, triggering, vacuum, timing and monitoring systems required for plasma generator operation were installed and commissioned. The laboratory is equipped with resistive and infrared temperature measurement systems, optical emission spectroscopy, rest gas mass spectrometry, High resolution oscilloscopes and a mobile plasma monitoring Langmuir gauge for diagnostics and monitoring.

The plasma generator prototype was successfully produced and tested, and first results presented in refereed journal papers. At low repetition rate the plasma generator could be operated up to the nominal 100 kW peak RF power. At 50 Hz repetition rate, operation was achieved for up to 3 kW average RF power. During the tests, the validity of the cooling system was demonstrated. The plasma was fully characterized via optical emission spectroscopy with 25 µs resolution. The RF coupling efficiency to the plasma is measured for each RF cycle.

This first prototype is promising and will be further operated to systematically study the influence of each operation parameters around its nominal value. The result is a relevant contribution to the upgrade of CERN's Linac4 ion source. Pictures of the first plasma ignition, RF induced plasma pulse and high power 50 Hz plasma seen from the extraction region are shown below.
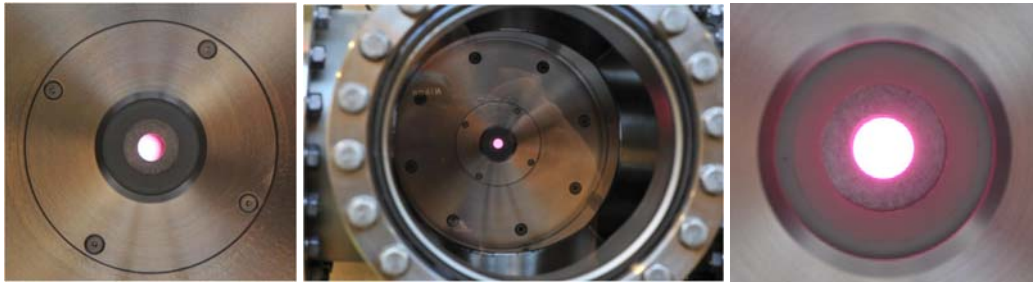
First spark gap ignition	First RF sustained plasma	50 Hz, 50 kW, 1.2 ms plasma operation

1. Introduction

The H$^-$ ion source specification of CERN's future 160 MeV linear accelerator (Linac4) [1] is to deliver a 80 mA H$^-$ beam with 0.7 ms pulse length at a repetition rate of 1 or 2 Hz. Its first prototype was derived from the DESY ion source [2]. The High Power Superconducting Proton Linac (HP-SPL) [3] project requires 40-80 mA and 0.4-0.8 ms pulses of H$^-$ ions after suppression of typically 100 µs head and tail instabilities. The HP-SPL will be operated at a repetition rate of 50 Hz. A non caesiated plasma generator has been developed [4] and designed to operate at the two orders of magnitude larger duty factor (> 5%) required by the SPL. The two leading aspects of this upgrade are the handling of the high power density deposited by the RF into the plasma (typically 50% of the RF power is transmitted to the components of the plasma generator and matching network) and also the 25 times higher gas injection. Efficient pumping is currently achieved at Linac4 by two 500 l/s turbo molecular pumps while few thousand l/s are required to at the RAL-ISIS facility which operates at 50 Hz. This solution can be implemented at the SPL, however, an innovative pumping system with high molecular capture efficiency especially for H$_2$ would be a real asset to increase effective pumping speed and minimize the required space.

Once the plasma generator will be incorporated into an ion source, utmost reliability and high performance diagnostics are mandatory. In the course of the present study, fundamental aspects of monitoring, and diagnostics were addressed. RF energy balance and plasma characterization by means of optical emission spectroscopy were investigated and will effectively complement the standard ion source current and emittance measurement techniques.

2. SPL plasma generator design

2.1. Overview

The fully assembled SPL plasma generator prototype is shown in Figure 1. Figure 2 shows a 3D section view of the plasma generator and its key components. The design of each component is detailed in the following chapter and the modifications to the original DESY design are described.
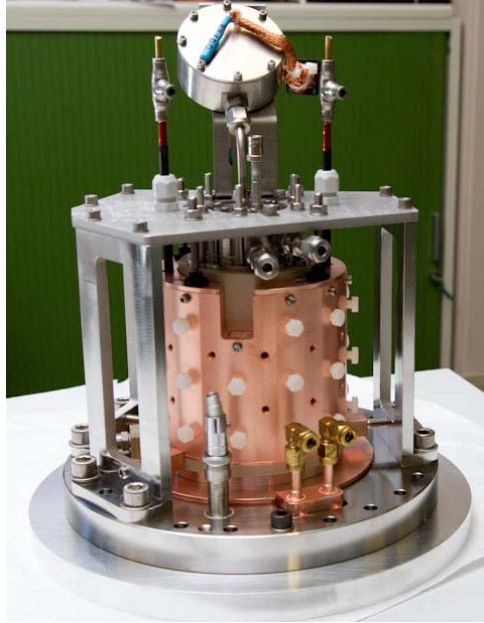
Figure 1: Assembled SPL plasma generator.
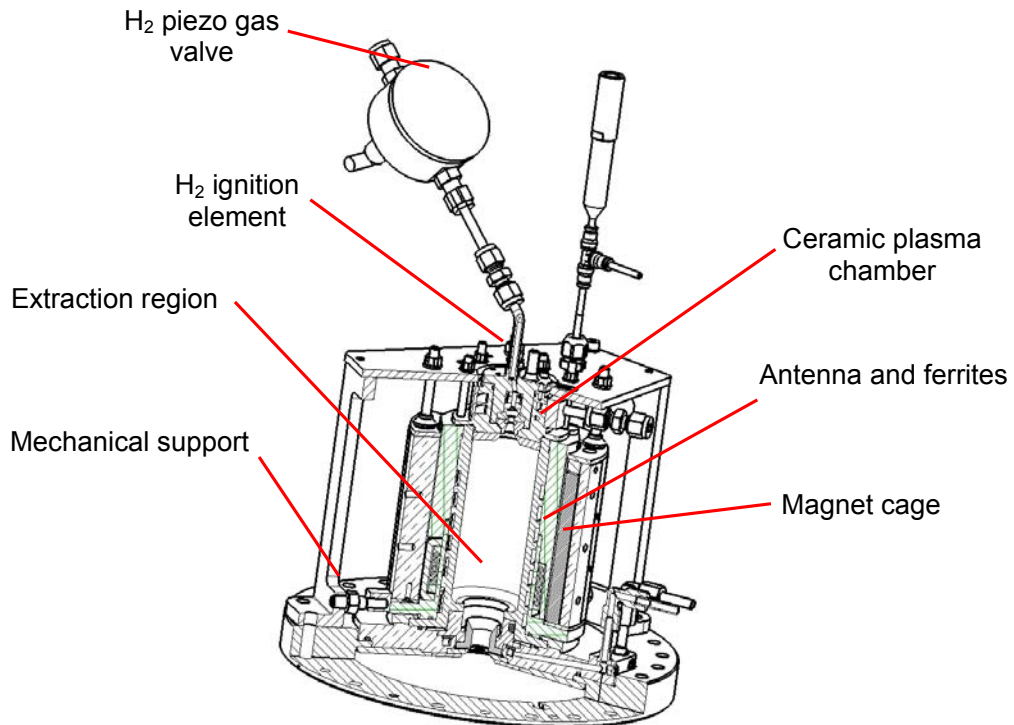
Figure 2: A 3D section view of the SPL plasma generator prototype and the key components.

2.2.   H$_2$ piezo gas valve

The purpose of the H$_2$ piezo gas valve is to accurately inject a burst of gas into the ignition chamber.

The stainless steel pipe between the piezo gas valve and the ignition element body has been extended to avoid possible sparking between the valve and the electrical connectors of the antenna. This extension can be exchanged by a T piece onto which a pressure gauge can be mounted for characterizing the system.

In order to stabilize DC and pulsed mode gas injection, the temperature of the piezo gas valve is regulated by means of an external cooling system shown in Figure 3. The gas valve is sandwiched between two copper plates coupled to a water cooling circuit. A thermostat (Lauda Alpha RA8) is used to regulate the temperature of the valve to a precision of < 0.1°C.
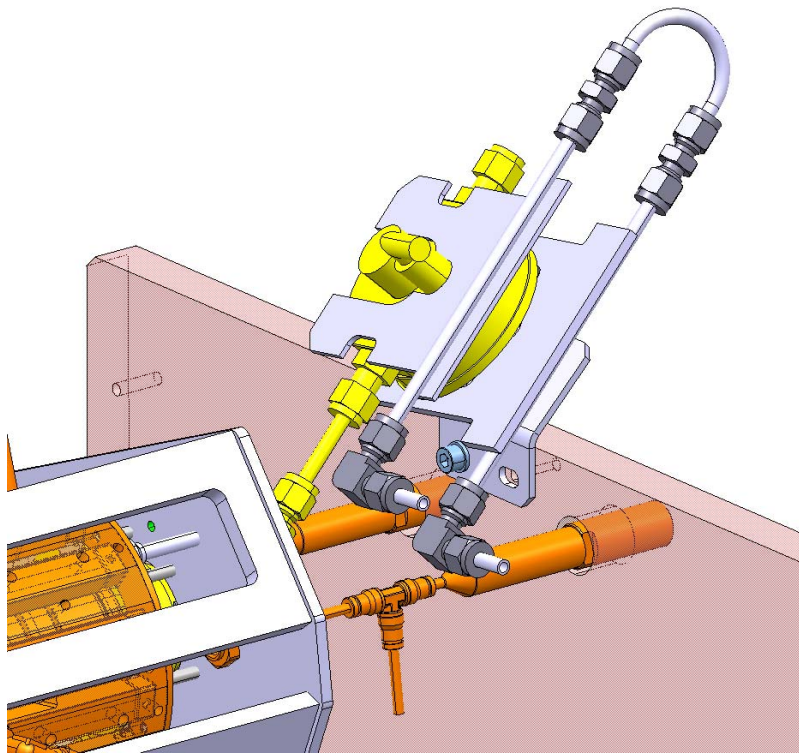
Figure 3: 3D view of the piezo gas valve equipped with the external temperature control system.

2.3.   H$_2$ ignition element

2.3.1. Overview

The purpose of the H$_2$ ignition element is to pre-ionize the H$_2$ before injection into the plasma chamber. Figure 4 shows a cross section through the ignition element and the key components discussed in this section.
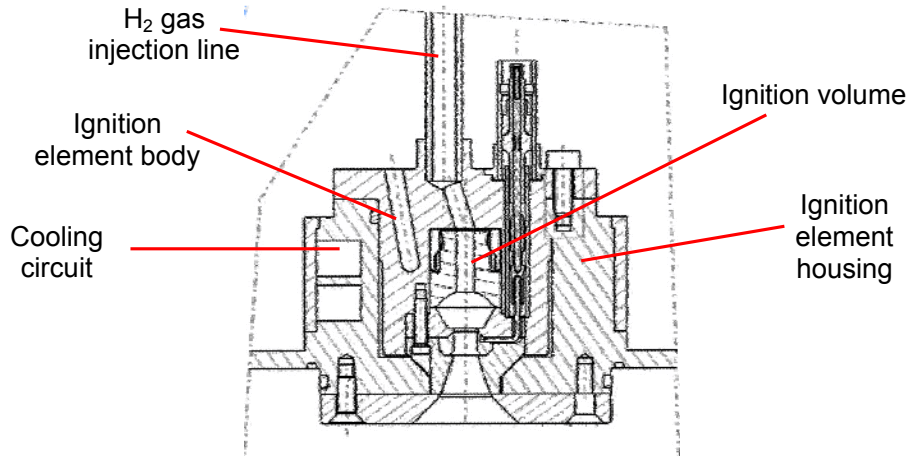
Figure 4: The ignition element assembly.

2.3.2. Ignition volume

The ignition volume comprises a cathode, an anode, two insulators separating the anode from any grounded metallic components, and the wire connecting the anode to the Lemo high voltage supply (see Sect. 2.3.4) Figure 5 shows a cross section through the ignition volume.
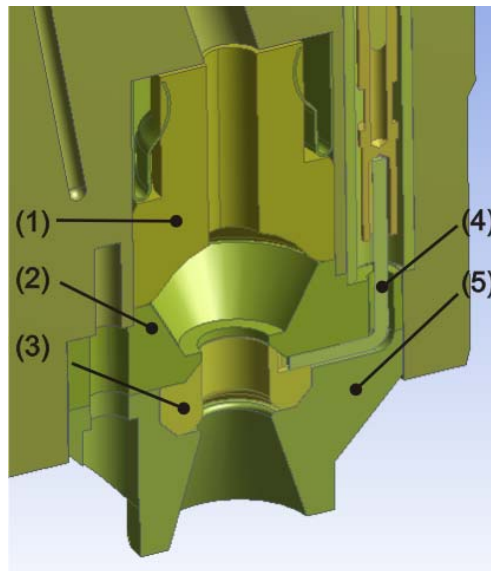
Figure 5: 3D section view of the ignition volume: (1) cathode; (2) AlN disk; (3) anode; (4) anode wire; (5) AlN clamp collar.

Good mechanical stability is ensured by a metallic clip holding the cathode in place. The clip also establishes a good electrical and thermal contact between the cathode and the ignition element body. The rounded shape of the cathode provides uniform field emission. For optimum thermal flow, all insulators are made of high thermal conductivity aluminum nitride (AlN) ceramic. In order to avoid unwanted sparking, the anode wire is fully coated with Kapton, and the crimp connecting the wire with the Lemo high voltage connector (Sect. 2.3.4), is insulated by an Al_2O_3 tube.

Apart from the spark gap design presented in Figure 5, other solutions were also tested in order to identify a design with minimum ignition voltage and average power

consumption (Figure 6). Other means of plasma ignition (radioactive sources, microwaves) may be tested in the future.
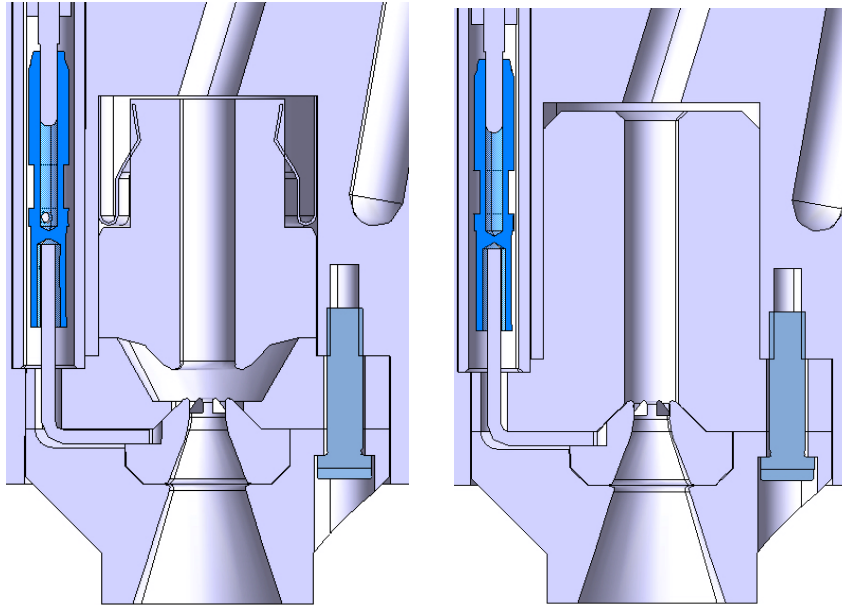
Figure 6: Section views of alternative ignition volume designs. Left: changed anode and cathode design for E-field maximization. Right: cathode replaced with an insulator to increase the product of sparking distance and H_2 pressure.

2.3.3. Ignition element body

Figure 7 shows a 3D section view through the stainless steel ignition element body. The optical port used in the Linac4 plasma generator for monitoring has been removed to leave space for the cooling circuit, allowing the gas injection line and the HV Lemo connector for the anode power supply to be moved closer to the center. The gas injection line now opens to the center of the ignition element which provides homogeneous injection of H_2 into the spark gap. An additional hole in the element body allows for measurement of the temperature close to the cathode with a thermocouple.

2.3.4. Ignition element housing

Figure 8 shows a 3D section of the modified ignition element housing. A cooling channel with a rectangular cross-section of 6 x 7.5 mm^2 is engraved into the outside wall. Then a stainless steel sleeve containing connections for the inlet and outlet tubes is welded onto the outside to close the circuit. The entry disk is made of AlN to improve the heat transportation from plasma volume towards the coolant circuit. CFD and thermal simulations performed for this design [5] predict non-critical temperatures in all components for a coolant flow rate of 0.36 l/min and for 100 kW, 1.2 ms, 50 Hz operation.
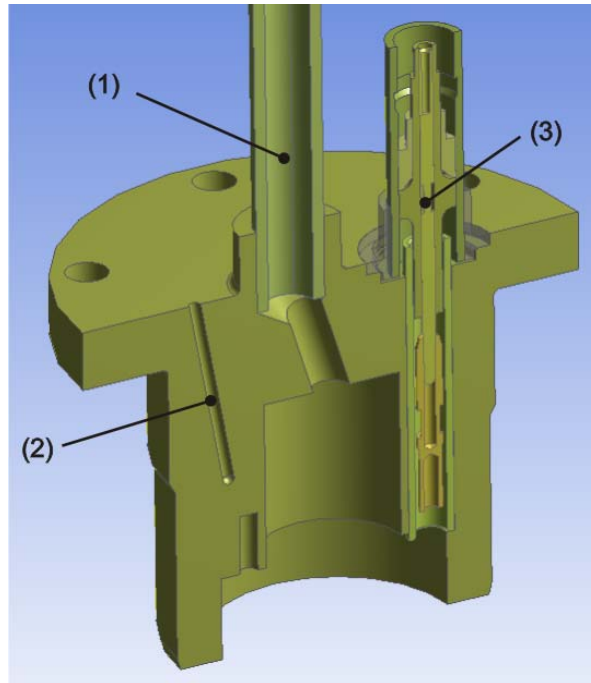
Figure 7: 3D section view of the ignition element body:. (1) gas injection line; (2) thermocouple probe hole; (3) Electrical connector for anode power supply.
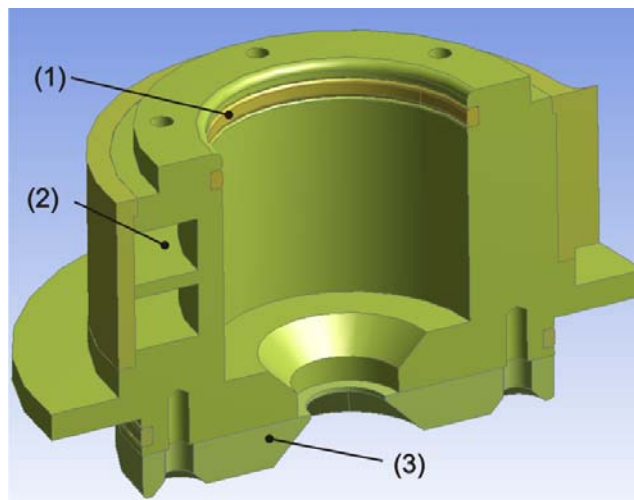
Figure 8: 3D section view of the ignition element housing. (1) O-ring. (2) Cooling channel. (3) Entry disk.

2.4.   Ceramic plasma chamber

The purpose of the plasma chamber is to provide a confinement vessel for the plasma. A 3D section view of the ceramic plasma chamber and the adjacent components is shown in Figure 9. A comparison with the Linac4 plasma chamber is given in [5]. The new design comprises an outer flange at the front end that simplifies the assembly with the extraction collar, and an inner flange partially shielding the collar region from the plasma heating region. The shape and size of the inner volume of the SPL plasma chamber are identical to its Linac4 counterpart, except for a 4% reduction in length.

The thermal radiation model used for calculating the heat load into the source [5] predicts that the plasma chamber receives more than 90 % of the thermal load from the plasma. For this reason, efficient removal of the heat from the plasma chamber is vital for high power (HP-SPL) operation. Optimization of the heat transport is achieved by the use of AlN as the choice of material for the plasma chamber. Furthermore, the exterior surface of the ceramic plasma chamber contains a coil-like cooling circuit for optimized cooling of the chamber even during operation at high duty factors and high RF power [5].
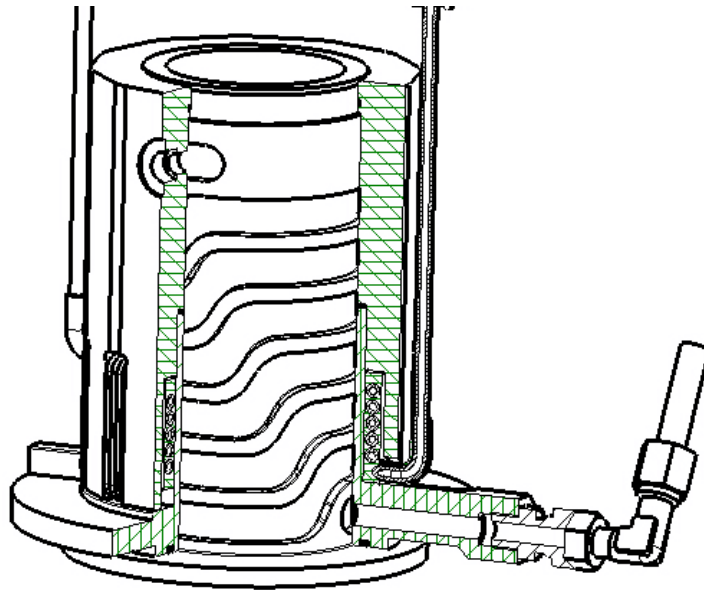
Figure 9: 3D section drawing of the ceramic plasma chamber and PEEK cooling sleeve.

The ceramic plasma chamber is surrounded by a jacket or sleeve made of Polyether ether ketone (PEEK) that confines the cooling circuit on the outside (Figure 10). The PEEK cooling sleeve is split into a front part and a back part in order to allow for the antenna to be installed. Connections for the cooling water inlet and outlet are implemented at the front and back end of the sleeve. The leak tightness of the cooling circuit is assured by three o-ring seals (one at the back end, one at the front end and one at the contact surface between the front and back part). The dimensions of the PEEK cooling sleeve have undergone several iterations to accommodate design changes to the magnet cage [6].

Two ceramic plasma chambers made of AlN ceramic have been produced externally by CeramTec (Figure 11). Several non-critical flaws (sharp edges at cooling channels, deviations of the cooling channel shape from nominal, surface roughness) were detected during inspection at CERN on the delivered item. The flaws were discussed with the producer, and a strategy for mitigation in future chambers developed. This strategy involves minor design adaptations on the outline of the cooling circuit, and changes in the manufacturing process itself. The PEEK cover was produced at the CERN workshop.
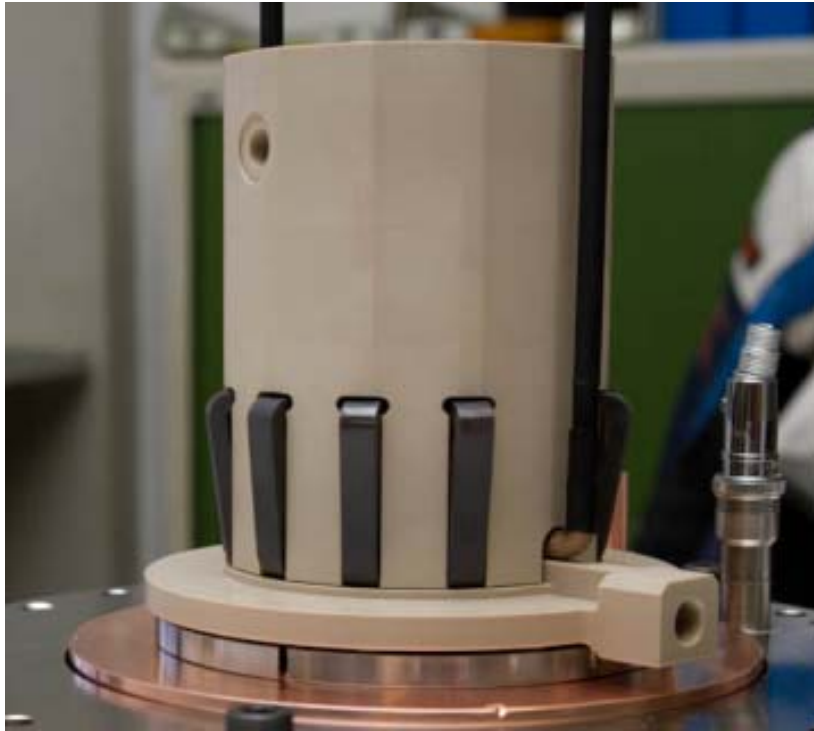
Figure 10: Ceramic plasma chamber, cooling sleeve, and ferrites during assembly.

Figure 11: AlN ceramic plasma chamber.

2.5. RF antenna and ferrites

The purpose of the RF antenna is to produce an RF electro-magnetic field that inductively couples to the plasma. The ferrites provide a return yoke for magnetic flux thus enhancing the coupling of the field into the plasma.

2.5.1. RF antenna

An image of one of the produced antennas is provided in Figure 12. The inner and outer radii of the antenna are 35mm and 40 mm, respectively. The antenna is made of hollow-tube Cu with 4 mm outer diameter and 2 mm inner diameter in order to be able to cool the antenna internally during operation. The antenna currently installed in the plasma generator prototype has 5 ½ windings, the same as the Linac4 antenna. The connection between the antenna and the matching network (Sect. 3.6) is achieved by custom Cu connectors (Figure 13) which, at the same time, provide good electrical contact and allow a shared cooling circuit of both entities. All antennas were built at the CERN workshop using a dedicated winding tool.
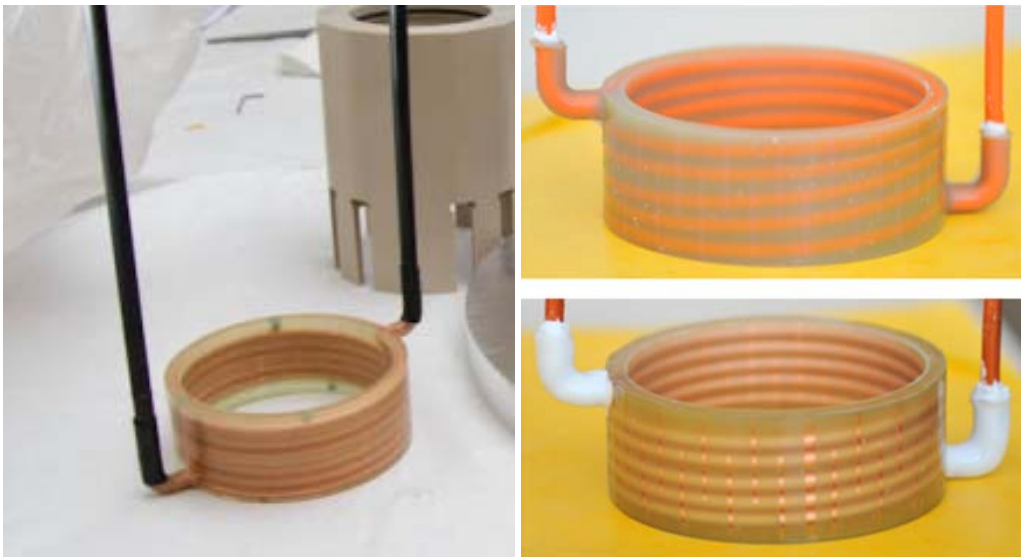
Figure 12: Left: Photo of the installed RF antenna. Right: Antenna coils with improved insulation.

When operating at high current the antenna voltage can become significant (>10 kV). Special attention must be paid to the insulation of the antenna near surrounding grounded or floating structures, such as the magnet cage (Sect. 2.6) and the extraction region (Sect. 2.7). Unwanted sparking is eliminated by increasing clearances, removing sharp corners and shielding triple junction points. Air gaps and voids in insulation systems can cause localized electric field enhancement and partial (capacitive) discharges. Care has been taken to avoid field enhancement caused by insulation permittivity mismatches.

Several insulation strategies have been tested for the antennas in order to avoid unwanted sparking. The first produced antennas comprised an epoxy molded coil with a minimum epoxy thickness of 0.3 mm, and a combined Kapton-shrink tube insulation of the antenna tips. However, these antennas suffered from partial coronal discharges on the high voltage side, and destructive shortcuts between the windings despite a minimum dielectric strength of 8 kV for the antenna coil and several tens of kV for the antenna tips were observed at one occasion (Figure 14). For this reason, the minimum thickness of the epoxy block was increased in newer antenna versions, and other insulation strategies tested, such as epoxy spraying of the antenna coil

and tips, and metallization of the outer surface of the insulator in order to short-circuit the air gap between the antenna tips and the magnet cage.

The RF antenna insulation was processed at the CERN Polymer Lab. The molding procedure for the epoxy insulation was tested on several antenna prototypes in order to exclude enclosed air bubbles that could cause partial discharge problems.
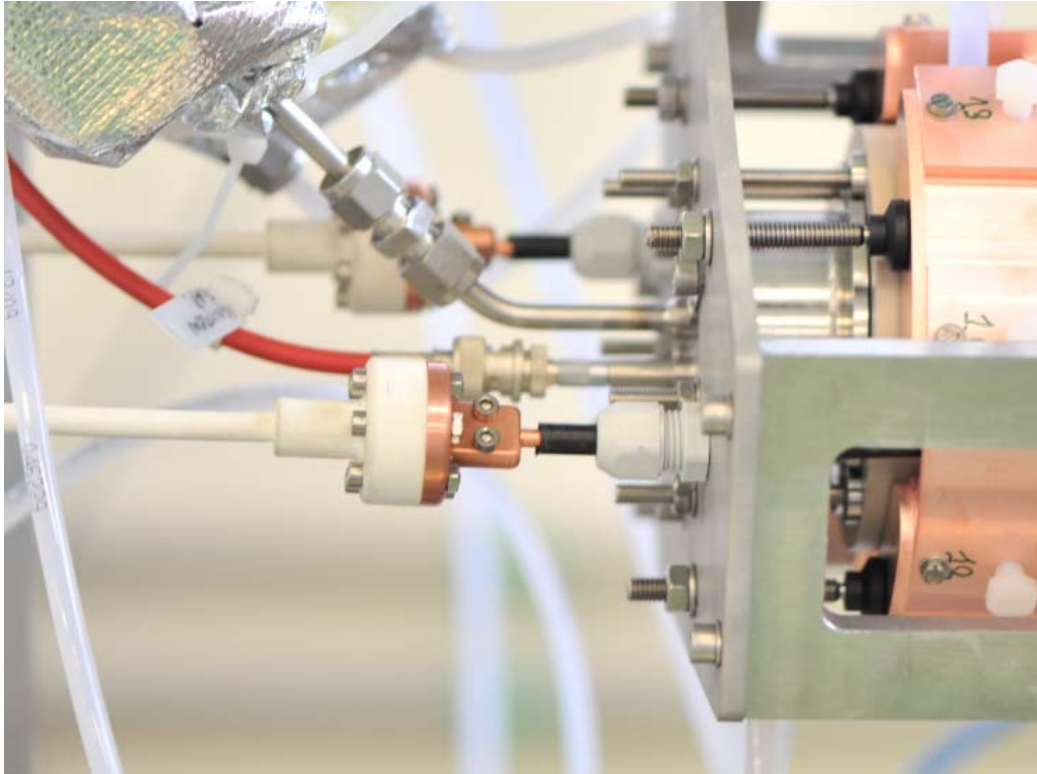
Figure 13: Photograph of the Cu connectors between antenna and matching network.

2.5.2. Ferrites

The shape of the ferrites was changed in order to reduce the heat load on the magnets and, to maximize the magnetic field strength inside the plasma chamber. Two ferrites are shown in Figure 15.

Two different sets of ferrites are available:

- Width = 8mm, Material: 4L, FerroXCube [1] (see Figure 15)
- Width = 2.55mm, Material: 8C11, FerroXCube [2]

Having two sets of ferrites allows for comparing the impact of different ferrite materials on the RF coupling. In addition, the latter set of ferrites can also be used for an evaluation on how the coupling of the RF power into the plasma changes with increasing amount of ferrite material surrounding the antenna. The 8C11 ferrites were purchased from FerroXCube. The 4L ferrites were produced at CERN from available spares.

---

[1] *FerroXCube, Hamburg, Germany*
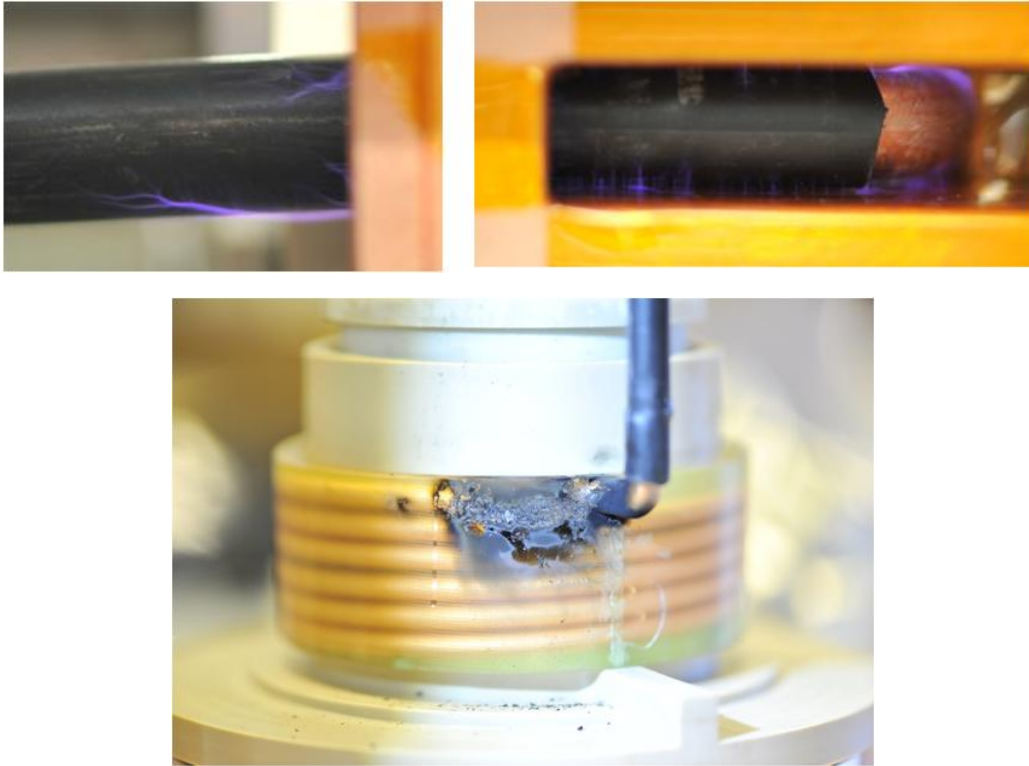
Figure 14: Top: Coronal discharges between the high voltage side of the antenna and the magnet cage due to insufficient space between the antenna tip insulation and the Cu cage. Left: Discharge at the end of the magnet cage. Right: Discharge close to the antenna coil. Bottom: Severe damage on a produced RF antenna following a series of discharges between the antenna coil and one ferrite.

Experiments on the test stand have demonstrated significant heating of the ferrites due to hysteresis losses (see Sect. 6.2.1). As a consequence, an air cooling system for the ferrites was installed at the SPL plasma generator test stand. In future experiments, the problem of overheating may be mitigated by using soft magnetic compounds with smaller hysteresis losses.

Figure 15: Two of the ferrites used in the SPL plasma generator.

2.6. Cusp magnets and magnet cage

The purpose of the cusp magnets is to provide the multi-cusp field that confines the plasma.

The magnet cage of the SPL plasma generator has seen the most significant changes of all source components. The changes were motivated by:

- (a) the optimization of the magnetic configuration,
- (b) the minimization of power losses due to eddy currents induced by the RF field.

2.6.1. Magnetic cusp configuration of the SPL plasma generator

The magnetic cusp field is a multipole magnetic configuration around the plasma chamber of an ion source plasma chamber. It reduces the plasma losses on the chamber walls, thus reducing heat loads and increasing the plasma density. In order to optimize the plasma production by the RF-coil, the gradient of the magnetic field strength should be high close to the walls of the plasma chamber in order to maximize the volume where the magnetic field strength is low. Furthermore, the magnetic field strength close to the wall should be as high as possible for optimum wall protection.

For the SPL plasma generator, dodecapole and octopole magnetic configurations were chosen. The optimum size, type and configuration of the cusp field was determined from simulations with the TOSCA module of Vector Fields Opera© (see also Ch. 4). The best results were achieved by employing offset-Halbach-type magnets [5-7], each of which consists of 3 magnets of size 4.5 x 10 x 99 mm^3 (Figure 16). This gives a total size per Halbach element of 13.5 x 10 x 99 mm^3.

Figure 16: Photograph of an offset Halbach element.

In addition to the Halbach elements, brick-shaped magnets with standard N-S magnetization and respective sizes 13.5 x 10 x 99 mm^3 and 13.5 x 10 x 70 mm^3 are employed. These magnets produce a ≈ 40% weaker field as the Halbach elements and can be used to assess the dependence of plasma parameters on the strength of the magnetic cusp field.

A total of three different magnet sets have been purchased from two different suppliers. The brick-shaped magnets and eight Halbach elements were purchased

from Vacuumschmelze [2] (material: Vacodym 633HR). Additional 18 Halbach elements were purchased from IMA [3]. The different sets are listed in Table 1.

Table 1: Available cusp magnet sets and remanences B_r.

material	producer	B_r [T]	magnetization	Size [mm^3]	# pieces
Vacodym 633HR (NdFeB)	Vacuumschmelze	1.35	N-S	13.5 x 10 x 99	18
				13.5 x 10 x 71	4
			Halbach	(3 x 4.5) x 10 x 99	8
Nd 38 (NdFeB)	IMA	1.26	Halbach	(3 x 4.5) x 10 x 99	14
				(3 x 4.5) x 10 x 71	4

2.6.2. Dodecapole and octopole magnet cages

Simulations with the Vector Fields Opera software package have shown that a Cu shielding is essential to protect the cusp magnets from overheating by the dissipation of RF power [6,7]. By measurements on a dedicated test stand (see Sect. 6.2.2), the effectiveness of this copper shielding could be shown. Thermal simulations based on the test stand results have shown a 5-fold decrease in the amount of power deposited in copper shielded magnets as compared to unshielded magnets.

The results of the Opera simulations triggered the development of dodecapole and octopole magnet cages that are entirely made of Cu. Figure 17 shows both magnet cages. The cusp magnets are contained in rectangular holes with a cross-section of 14.2 x 10.5 mm. Small wedges installed at the back end of the holes after magnet insertion prevent the magnets from falling out. The magnets are pushed inwards by plastic screws, assuring that the magnetic cusp field is as homogeneous as possible and not disturbed by any misalignment of the magnets. The magnet cage is closed at the front end by a Cu ring brazed onto the main body of the magnet cage. This Cu ring contains small holes at the position of each magnet which allow pushing them backwards when the magnet cage is disassembled. The external surface of the magnet cage contains additional screw holes which allow for mounting an optional cooling system on the outside, in the case that active cooling of the magnet cage is required during high average power operation. A cut out at the back end provides access to the plasma chamber cooling outlet. Note that in the case of the dodecapole, two of the cusp magnets had to be shortened due to the space restrictions by the plasma chamber cooling outlet, and symmetry considerations. The likelihood of sparking between the (floating) magnet cage and the extraction region is reduced by a PEEK spacer introduced between these two components.

The high density of the magnets in the dodecapole magnet cage restricts the clearance available between the magnet cage and antenna power feed. This lack of clearance caused sparking that limited the maximum antenna power achievable in the dodecapole design. The larger clearances in the octopole magnet cage allows the design power of 100 kW to be reached. The clearance problem can be overcome in future designs by simply re-routing the antenna power feed so it does not pass through the magnet cage, or by coating the outer surface of the antenna insulation with a conducting layer.

---

[2] *Vacuumschmelze GmbH & Co. KG, Grüner Weg 37, D-63450 Hanau, Germany*

[3] *IMA Ingenieria Magnetica Aplicada S.L., Avda. Rafael Casanova, 114, 08100 Barcelona, Spain*
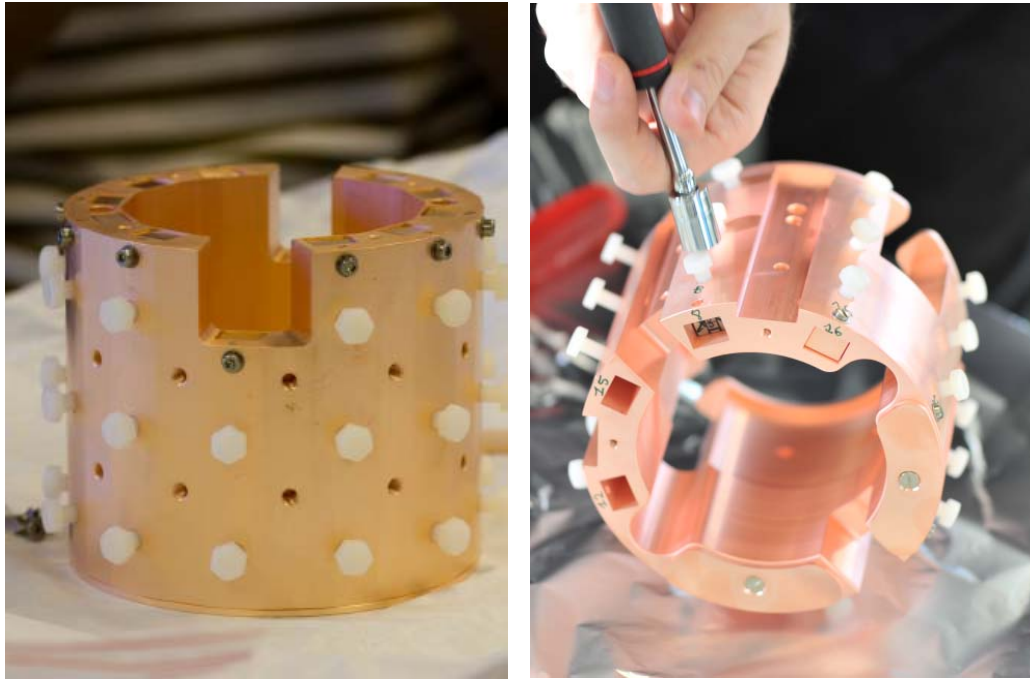
Figure 17: SPL plasma generator magnet cage. Left: dodecapole. Right: octopole.

2.7. Extraction region

The purpose of the extraction region is to provide a region for optimum H⁻ production and extraction. A 3D section view is shown in Figure 18 alongside with a photograph of the produced piece. The heat transportation away from the collar electrodes is optimized by the use of AlN ceramic for electrical insulators, the brazing of the molybdenum funnel and aperture electrodes with the insulators that separate them from each other and from the metallic body of the plasma generator (Figure 19), and an implemented cooling circuit.

The filter magnets are contained in an aluminum nitride magnet holder. Unlike the filter magnets used in the Linac4 source, the magnets of the SPL plasma generator are arc-shaped to minimize the required space, and to achieve a better radial uniformity of the magnetic filter field. Three different sets of filter magnets are available for testing (see Table 2). In order to avoid overheating of the filter magnets, they are contained in small Cu boxes (Figure 20). Simulations with Vector Fields Opera have shown that this approach reduces the dissipated RF power by one order of magnitude [6,7].

Table 2: Available filter magnet materials and remanences B_r.

material	Type	producer	B_r [T]
Vacodym 633HR	NdFeB	Vacuumschmelze	1.35
Vacodym 677HR	NdFeB	Vacuumschmelze	1.18
Vacomax 170HR	$SmCo_5$	Vacuumschmelze	0.95
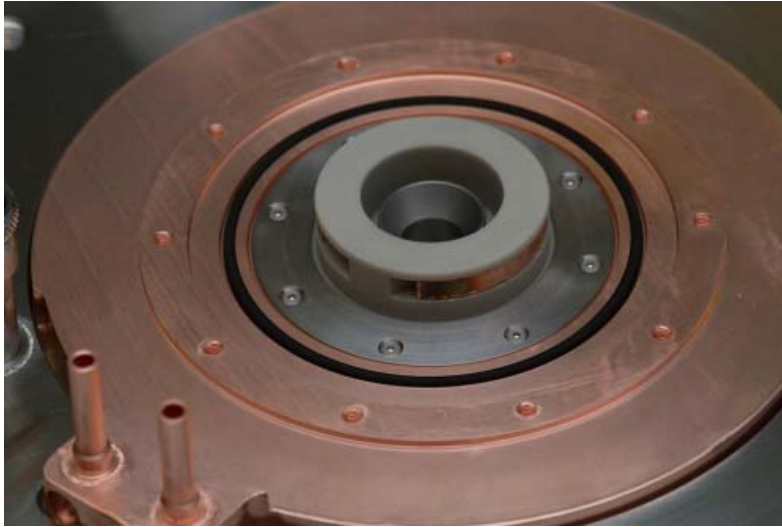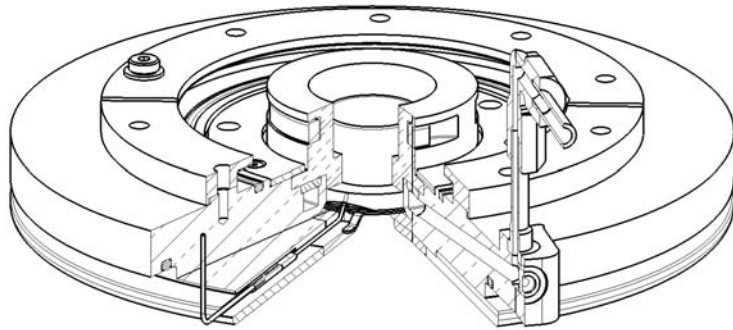
Figure 18: Extraction region. Top: 3D CAD view. Bottom: Photograph of the produced piece.

Figure 19: Brazed electrode assembly consisting of the funnel and aperture electrodes, the separating aluminum nitride insulators, and the electrical connections.
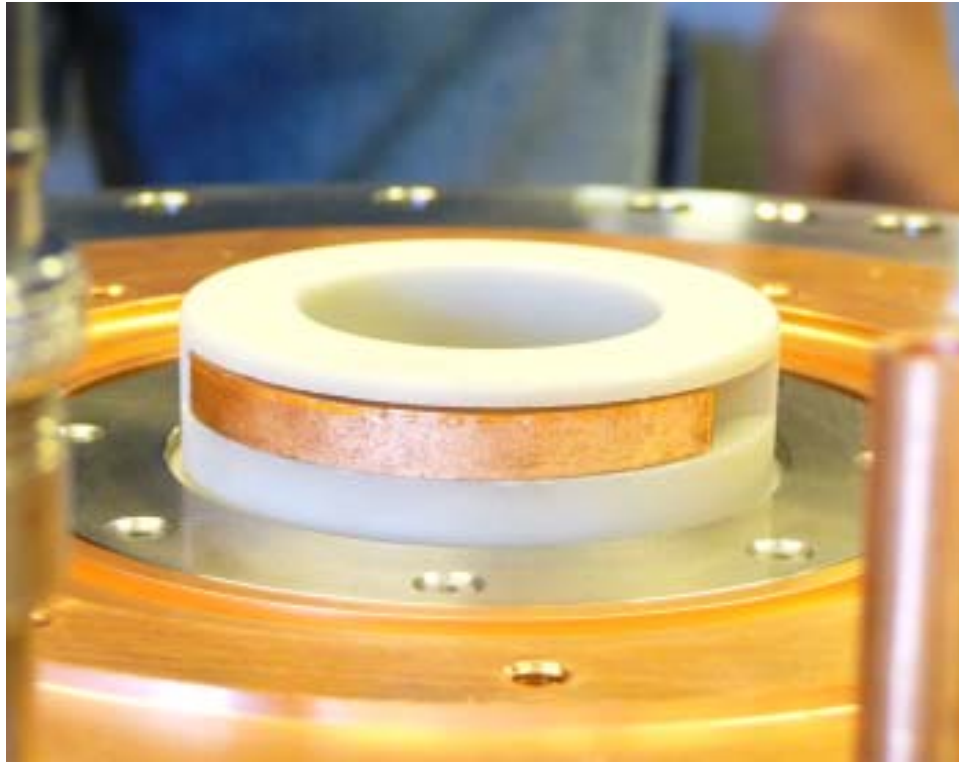
Figure 20: Cu shielded filter magnet.

2.8. Mechanical support

The purpose of the mechanical support is to provide a flange on which to mount the whole plasma generator. A 3D view of the mechanical support is shown in Figure 21. The mechanical support consists of a DN-200 flange connected to a DN-150 for installation at the test stand, a tripod stainless steel structure, and a back plate.

The plasma generator is clamped onto a DN-200 flange at the front end. Further positioning and mounting of the plasma generator components in axial and radial direction is made possible by a series of screws and shims (Figure 22).

At high powers significant antenna voltages >10 kV are reached. This produced sparking problems where the antenna passed through the back plate. To prevent the sparking the sizes of the holes in the back plate have been increased, and the plastic feed-throughs removed.
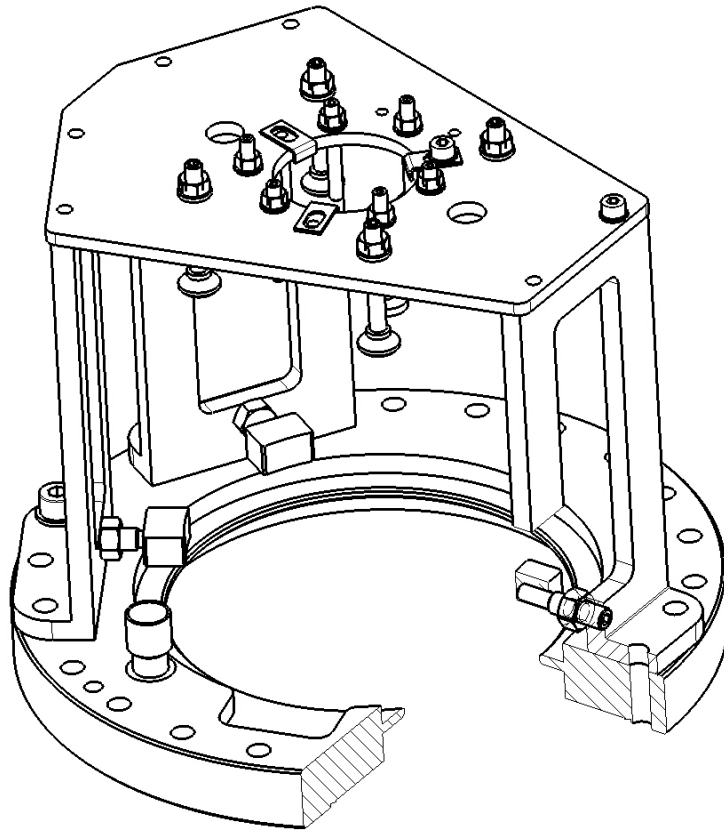
Figure 21: 3D view of the mechanical support of the SPL plasma generator.
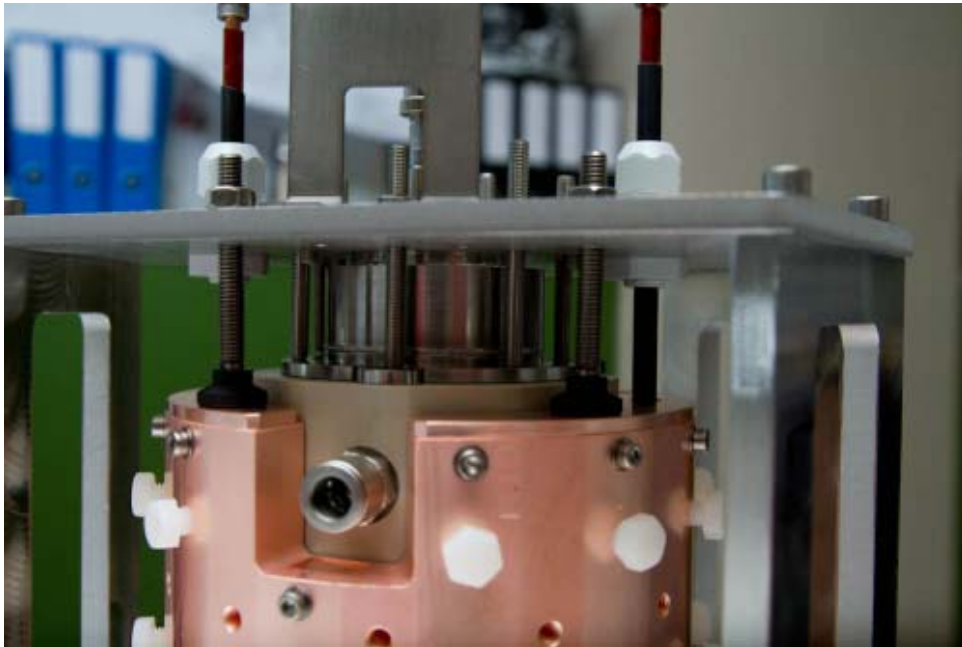
Figure 22: Mounting screws for the plasma chamber, PEEK cooling sleeve, and the magnet cage. The white plastic holders of the antenna tips suffered from coronal discharges and were removed in later tests.

3. Test stand and experimental setup

The SPL plasma generator test stand in room 357-R-005 has seen numerous updates and additions since the last deliverable report [6]. This section provides an updated review of the test stand and its subsystems.

A sketch of the test stand room [8], illustrating the position of the most important subsystems of the experimental setup, is shown in Figure 23. A short summary of each subsystem is provided, followed by detailed descriptions in the subsections.
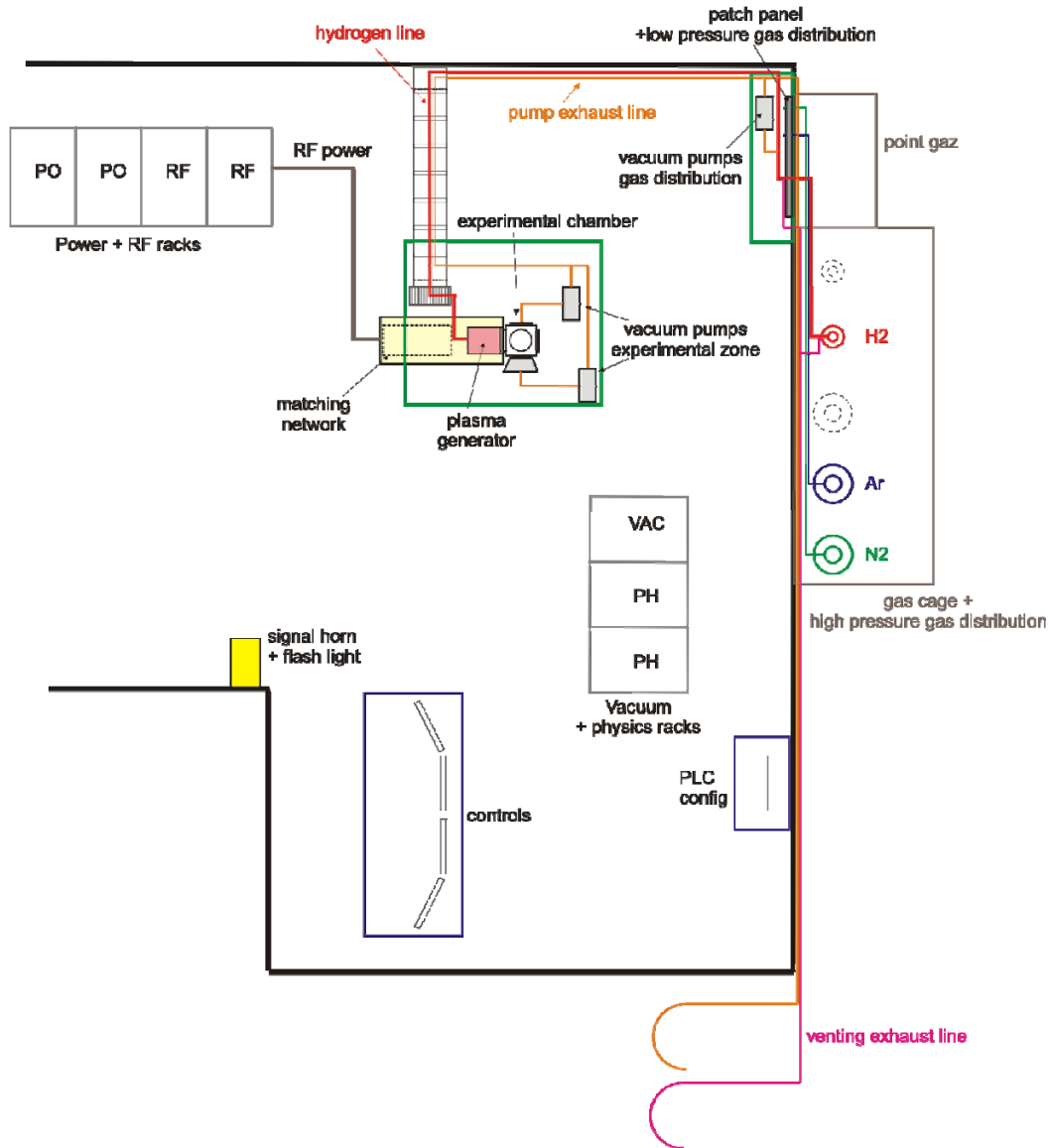
Figure 23: General layout of SPL plasma generator test stand in Room 357-R-005. The gas system, the experimental vacuum chamber, the racks for RF generation (PH), vacuum control (VAC) and measurement and triggering are indicated (PH).

Gas distribution and vacuum system: The high pressure hydrogen, nitrogen and argon gas cylinders are located outside the building. The low pressure gas distribution and experimental vacuum chamber are classified as explosive risk areas and constantly monitored by hydrogen calibrated gas detectors. The H_2 supply line,

high voltage power transformer and RF generator are interlocked by the flammable gas detection system.

The vacuum system comprises three pumping zones:

a) Rest gas analyzer (A mobile pumping group comprising a 60 l/s turbo molecular pump and roughing pump);
b) Low pressure gas distribution (60 l/s turbo molecular pump and roughing pump);
c) Experimental chamber (2×500 l/s, each in series with a roughing pump).

The pressure inside the vacuum tank is measured with three pressure gauges optimized for different pressure ranges between 10^{-8} mbar and atmospheric pressure. The exhausts of the experimental chamber pumps and gas distribution pumping systems are evacuated on the roof of building 357.

Air cooling: An air cooling system prevents the ferrites located around the RF antenna from overheating.

RF Generator: The high voltage power transformer and the RF amplifiers are installed within four racks. A single coaxial cable feeds the matching network of the RF circuit supplying the plasma generator RF antenna. The matching network and the plasma generator are located within a Faraday cage for safety. A frequency switch can be triggered as soon as the plasma light is detected, allowing for an optimization of the RF coupling for the ignition phase and the pulse mode. An oscilloscope is used for monitoring the forward and reflected power, the antenna current, and other RF related parameters.

Physics and vacuum racks: The physics and vacuum racks are shown in Figure 24. The leftmost rack contains the control units of the vacuum pumps and the control unit of the pressure gauges. The middle rack contains: the function generators for the gas pulse and the RF signal; the pulse generators controlling the timing of experiment and diagnostics; and an oscilloscope for signal analysis and visualization. The rightmost rack contains the power supplies of the piezo valve, the ignition element, the collar electrodes, and the electro valves of the cooling water; the gas detection unit; and a light amplifier for plasma light detection.

Monitoring & controls: Several PLCs provide the communication between the Labview-based control and monitoring system and the experiment, check the status of the experiment, generate visual warnings, and disable the power supplies in case a critical parameter is out of the accepted range, a critical component is inoperable, or the gas safety system triggers an alarm.

The Labview control and monitoring system monitors all parameters with a slow time response (i.e longer than1 second), such as the cooling water and gas temperatures and pressures. High frequency signals, such as the RF forward and reflected power, are recorded via oscilloscopes. A set of 2 PCs and four screens comprise the control system. A third PC is used for configuring the PLCs with the program Step7.

Figure 24: Left: High voltage and 2MHz RF generator. Right: Vacuum and controls racks.

Measurements and diagnostics: The test stand has several diagnostic tools which allow the performance of plasma generator and its components to be assessed.

The vacuum chamber, the gas line and cooling circuits are all equipped with Pt-100 temperature gauges to monitor the heat flow and experimental conditions. An infrared camera (Fluke Ti-32) is available to map external surface temperatures and, through a Germanium window, also the temperature of the extraction region of the plasma generator.

The magnetic field of each permanent magnet is mapped using a 3D Hall probe mounted on an arrangement of motorized stages from Zaber technologies. The B-field of single standard N-S and Halbach type magnets is mapped by a multi-axis system setup comprising three linear stages oriented in x-y-z direction. The axial and radial magnetic field distributions inside the dodecapole and octopole magnet cages are determined by mounting the cages on a rotary stage. A small test bench is available for measuring the RF power dissipated in the magnets and ferrites. This test bench comprises a hollow PMMA cylinder with insertion holes for magnets and ferrites, an RF antenna of the same dimensions as the one used in the SPL plasma generator, and a Faraday cage.

A rest gas analyzer connected to a laptop is used to determine the composition of the residual gas for impurity detection. A second laptop controls an optical spectrometer used for measuring the intensities of the molecular and atomic hydrogen lines, and for detection of pollutants in the plasma. A digital camera triggered by the control system is used to record optical emission from the plasma during ignition and during the RF pulse. A plasma generator mockup comprising a transparent (quartz) plasma chamber can be installed at the experimental vacuum chamber for studies of the gas dynamics and for plasma ignition tests. A transparent extraction plate for the SPL plasma generator will allow the plasma volume to be viewed through the collar. A Langmuir probe will be used to measure the ion and electron densities and temperatures.

3.1. Experimental vacuum chamber

The experimental chamber (Figure 25) is a three axis cross comprising six DN-150 flanges. The plasma generator or its Quartz mockup is mounted on the horizontal flanges closest to the hydrogen supply line. The opposite flange can be equipped alternatively with: the rest gas analyzer; a Quartz window for visual inspection and optical measurements; a Germanium window for thermal monitoring of the extraction region; a flange with an internal optical fiber holder for spectroscopic measurements; or the Langmuir probe.

Views of the Germanium window and the optical fiber holder are shown in Figure 26. The Germanium window (ø = 80 mm, d = 3 mm) is clamped onto a DN-150 flange equipped with a fitting groove and a vacuum seal. A rubber disc reduces mechanical stresses. During periods where no thermal images are being taken, the window is protected against the plasma by a mechanical shutter located inside the vacuum chamber.

Of the two remaining horizontal flanges, one is equipped with one of the turbo molecular pumps (see also Sect. 3.4). The second one has a viewport for the optical fibre and holds an internal mirror (Figure 27). This mirror makes plasma light detection and RF frequency switching possible even if the flange opposite to the plasma generator is used by different diagnostics.

The top flange is equipped with several gauges for vacuum diagnostics and N_2 injection. The bottom flange hosts the second turbo molecular pump (Sect. 3.4).
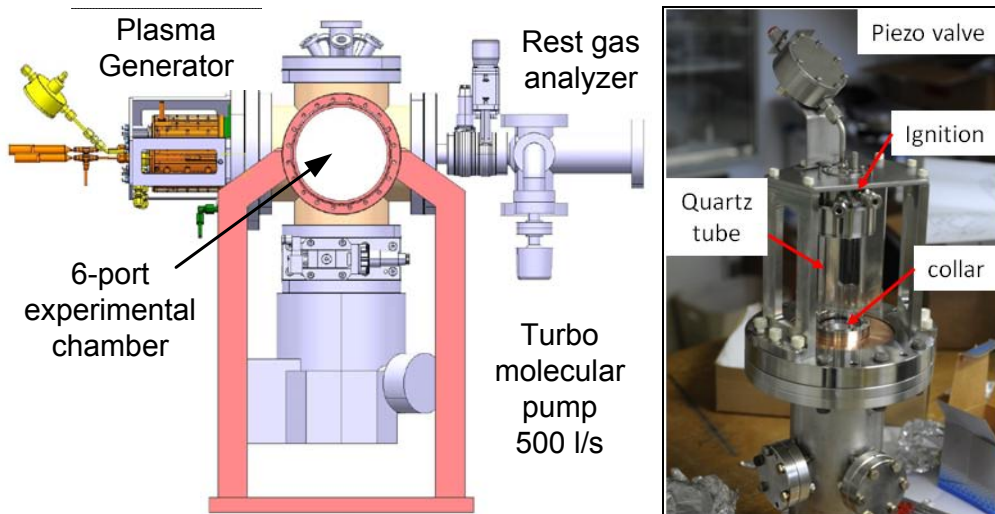
Figure 25: Left: Scheme of the experimental chamber with the plasma generator and, as an example of a diagnostic device, the rest gas analyzer. Right: A mockup dedicated to plasma ignition studies can be coupled to the experimental chamber instead of the plasma generator.
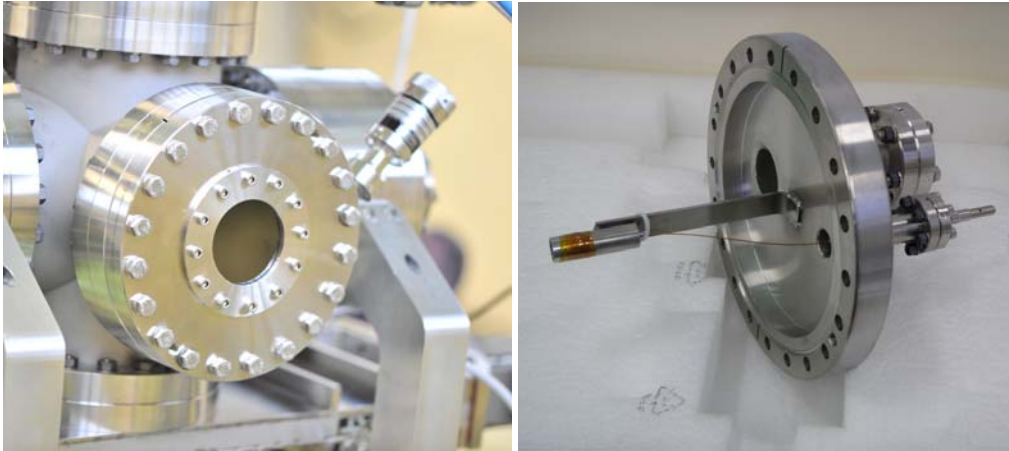
Figure 26: left: The Germanium window installed on the experimental chamber. Right: Optical fibre holder.
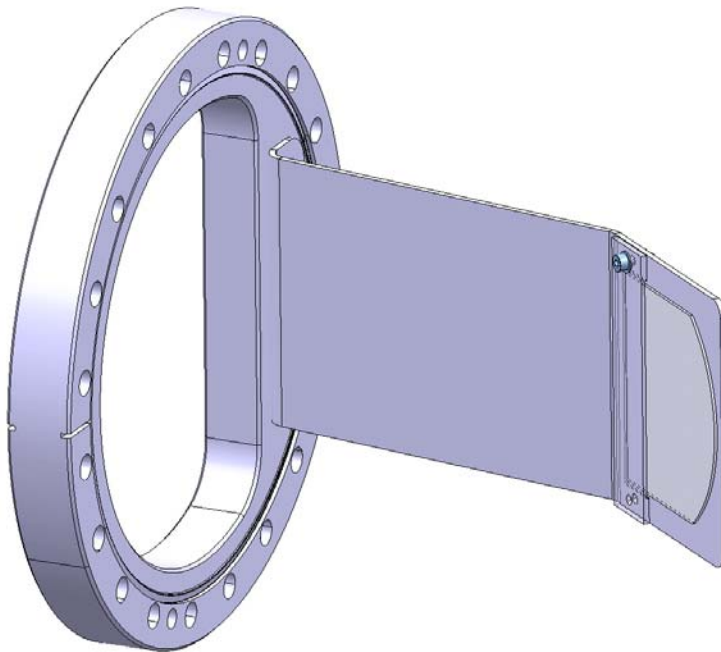
Figure 27: 3D view of the flange equipped with a mirror for plasma light detection.

3.2. Faraday cage

The plasma generator and the RF matching network are enclosed in a Faraday cage. A view of the assembly is shown in Figure 28. The Faraday cage is split into two parts in order to allow for separate access of the plasma generator and the matching network. Two view ports serve as access points for monitoring the temperatures of the magnet cage, the ferrites, and other components with the thermal camera.
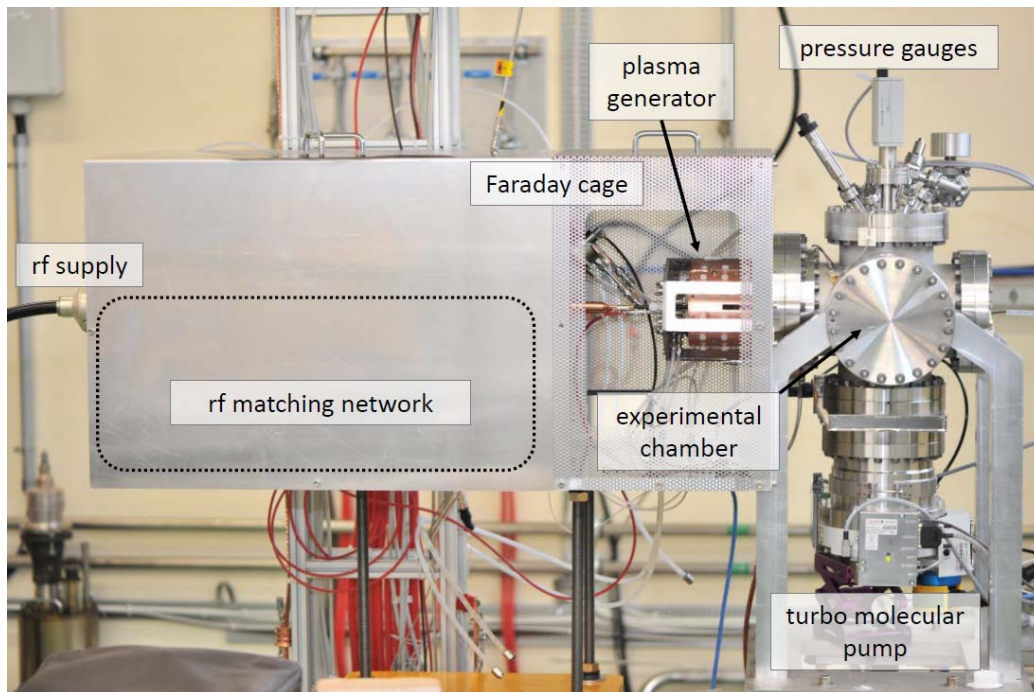
Figure 28: Side view of the test setup, showing the experimental chamber, the plasma generator, and the Faraday cage. The second turbo molecular pump was installed after the photo had been taken.

3.3. Gas system and gas safety installations

The test stand can be run with several types of gases (N_2, Ar and H_2). Additional spare gas lines for potential use of other gases (e.g. CH_4 and He) are available.

The gas bottles are stored outside of building 357 in a ventilated metallic cage. Each bottle is connected to an individual gas line that runs through the wall and ends at a patch panel close to the test stand. The gas pressure is reduced from bottle pressure to a maximum of 5 bars by a pressure reducer.

From the patch panel, the gas is redistributed to a second panel (low pressure gas distribution panel, Figure 29) that serves as an interface between the patch panel, the experiment, and the vacuum and exhaust systems. The low pressure gas distribution panel contains, for each gas type, reduction manometers and precision pressure gauges that allow the gas pressures to be set to their nominal values. Two vacuum pumps in series (1x mechanical, 1x turbo pump) can be used for purging the gas pipes before startup or after an intervention to avoid a potential hazardous mixture of H_2 with air, or for fine adjustment of the pressure inside the H_2 line.

The experimental setup is supplied with H_2 or Ar by means of a single stainless steel pipe. The piezo valve of the plasma generator is coupled to the pipe via a flexible stainless steel hose. An additional gas line supplying N_2 and limited to atmospheric pressure is connected to the top flange of the experimental chamber and can be activated in case of an intervention. The gas injection through the piezo valve is regulated with a waveform generator (Agilent 33220A).

Several gas safety systems minimize the risk of a hazardous event involving flammable H_2. H_2 gas pumped by the vacuum system or released through the overpressure valves is transported away by two exhaust lines that vent to

atmosphere on the roof of building 357. The pump exhaust line is constantly flushed with N_2 to ensure a non explosive N_2-H_2 gas mixture.

Two flammable gas detectors (type OLC-50) are installed in metallic hoods above the gas panels and the experimental zone. Both are coupled to a central unit (MX-32) that triggers a gas alarm in the case of a potentially hazardous H_2 concentration. The interlock scheme applied in case of a gas alarm is depicted in Figure 30.

Figure 29: Gas distribution system. Top: Patch panel. Bottom: Low pressure gas distribution.
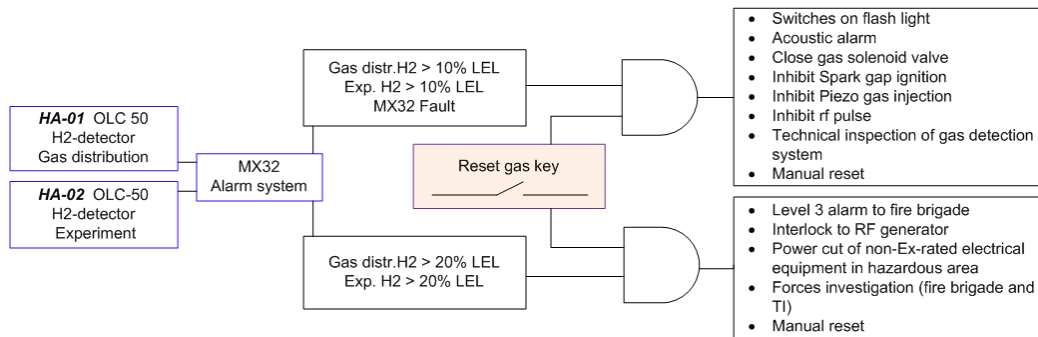
Figure 30: Interlock scheme for H_2 operation. The Lower Explosive Limit (LEL- H_2 = 3.5% vol. in air) is used to set maintenance warning (10% LEL) and alarms coupled to the interlock circuit (20% LEL).

3.4. Vacuum and pumping system

The vacuum system consists of a MV-112 piezo valve for gas injection, the ignition element (electron gun), the ceramic plasma chamber and the main vacuum tank. This vacuum tank is equipped with six DN150/160 vacuum flanges which are partly used for turbo molecular drag pumps and experimental tools. The top flange is equipped with three complementary gauges for pressure measurement with 5% to 10% precision from high vacuum ($p \approx 10^{-8}$ mbar) to atmospheric pressures. Two spare gauges (CMR 275 and PBR 260 from Pfeiffer vacuum) are also available. The vacuum gauges are selected with the following overlapping measurement ranges (Figure 31):

- APR 260, 0.1 -1100 mbar, Pfeiffer Vacuum
- CMR 375, 10^{-5} – 0.11 mbar, Pfeiffer Vacuum (CMR 275, $1 \cdot 10^{-5}$-0.11 mbar)
- PKR 261, 10^{-9} – 1000 mbar, Pfeiffer Vacuum (PBR 260, 10^{-8}-10^{-2} mbar)

The gauges are controlled with a MaxiGauge TPG 256 A unit from Pfeiffer Vacuum which allows simultaneous reading of the three gauges (the PBR, CMR and PKR gauges can only be used on ports 4-6). The analog output signals can be looped through to monitor the pressure curves directly on the oscilloscope. This makes it possible to record the gas pulse itself as the PBR260 and PKR261 gauges provide the required sampling rate, but show a pressure dependent time delay of typically 10 ms caused by the gauge electronics.

The bottom flange and one horizontal flange are equipped with Pfeiffer Vacuum TMU521 turbo molecular pumps coupled in series with one Edwards 12 mechanical pump each. The nominal pumping power of the turbo molecular pumps is 450 l/s for H_2. All vacuum pumps are connected to a secured exhaust pipe which is flushed constantly with N_2 to avoid H_2 air mixtures.

A separate pumping system is available for the QMA 125 quadrupole mass spectrometer for rest gas analysis and plasma process monitoring (rest gas analyzer, Figure 32 right). The QMA 125 is bakeable UHV standard equipped with a small turbo molecular pump (60 l/s, Pfeiffer TMU-071) and an Edwards 12 mechanical fore-pump. The RGA is connected to the experimental chamber via a retractable aperture reduction and a metallic valve.

Figure 31: Left: top flange equipped with APR 260 (steel), CMR 375 (red) and PKR 261 (grey) pressure gauges. Right: MaxiGauge pressure gauge control unit.
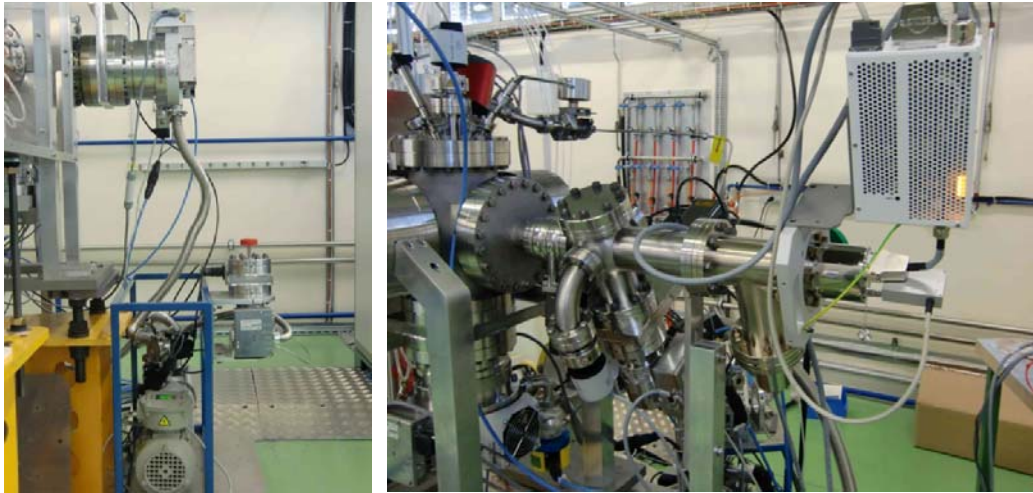
Figure 32: Left: side view of the experimental setup, showing one pumping unit with TMU521 mounted on vacuum chamber and an Edwards12 forepump (TMU071 optional). Right: Rest Gas Analyzer with additional PKR261 pressure sensor

3.5. Cooling and temperature control systems

Plasma chamber: During operation, the plasma generator and the matching network are cooled by a total of five cooling circuits (Figure 33). The injection and return water temperatures are individually measured via Pt-100 resistance thermometers. Flow interlocks are installed on each cooling circuit. A patch panel located close to the experiment distributes the cooling lines to the individual plasma generator circuits.

Piezo valve: The piezo valve is sandwiched between two water-cooled Cu plates for temperature stabilization. The cooling water temperature is set by an industrial closed loop controller (LAUDA Alpha RA8) with a precision of 0.1 °C. Typically, the temperature is set to 22.0 °C, however the piezo valve temperature may rise by a few degrees during high power operation because of the conduction of heat from the ignition element through the stainless steel gas pipe.

Ferrites: A filtered compressed air distribution system operating at a maximum pressure of 5 bars cools each ferrite individually.
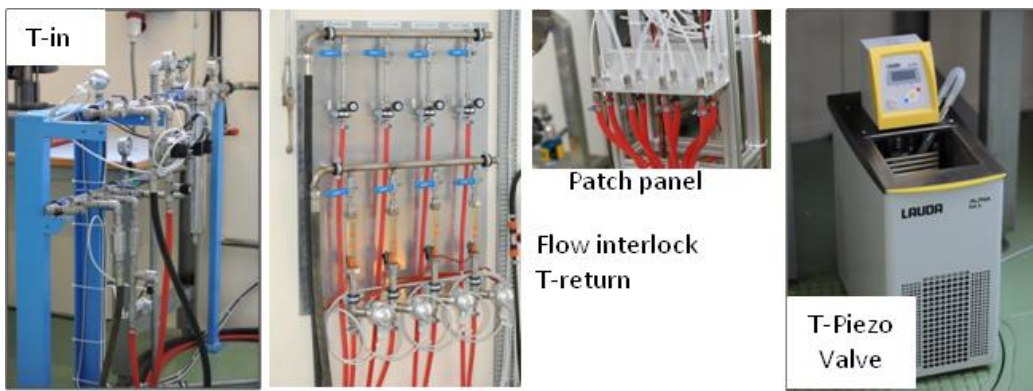
Figure 33: Views of the water cooling system. From left to right: the demineralized water distribution, the flow interlock and temperature measurement, and the patch panel leading to the individual plasma generator circuits. The temperature controller of the piezo valve is shown in the rightmost image.

3.6. HT-power converter, RF generator and matching network

The RF generator [9] of the SPL plasma generator (Figure 24) provides 100 kW, 2 MHz bursts of up to 2 ms duration at 50 Hz repetition rate for the plasma heating. Figure 34 shows a block diagram of the RF generator. The system is designed as an upgraded version of the one installed at Linac4. The higher duty cycle imposed by the increased repetition rate (50 Hz vs. 2 Hz) and increased pulse duration (1.2 ms vs. 0.4 ms) required upgrading the 22 kV HV power supply and overall system cooling. The complete system including the power supplies, RF low-power and high-power sections, interlocks and timings has been built, installed and tested on a 50 Ω load at nominal parameters. A high directivity directional coupler present at the power stage output allows measuring the forward and reflected waves from which the contribution of the plasma to the circuit's impedance can be deduced. A servo loop controlling the forward power as well as frequency switching ability allows optimization of the power transmitted to the plasma despite the impedance variation at plasma ignition. Two identical function generators (TTi TG 5011) define the RF frequencies and the shape and total power of the RF signal. Two different RF frequencies are used to optimize the plasma during ignition and during the pulse.

A photograph of the water-cooled RF matching network is shown in Figure 35. This version supersedes a prototype which was used in several measurements but did not contain any possibilities for active cooling. The coil and the pipes connecting the antenna to the circuit are made of silver-coated hollow-tube Cu with inner and outer diameters of 4 mm and 6 mm, respectively. Special Cu connectors assure a good electrical contact to the antenna and, at the same time, connect the matching network to the antenna cooling circuit. Consequently, the coil, the connecting pipes and the antenna form one single cooling circuit. A Pearson Model 150 current monitor located at the grounded end of the matching network is used to measure the antenna current.
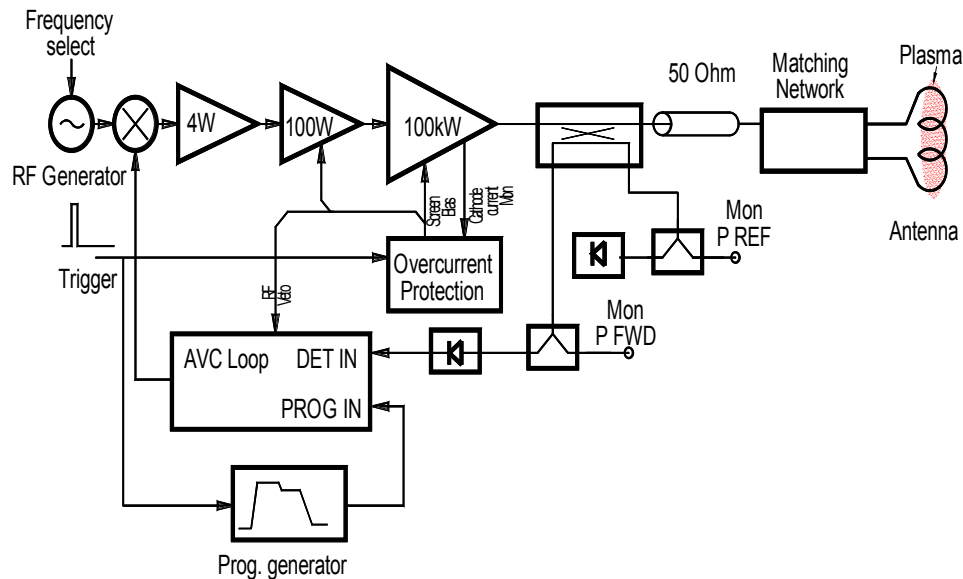
Figure 34: Block diagram of the RF generator.
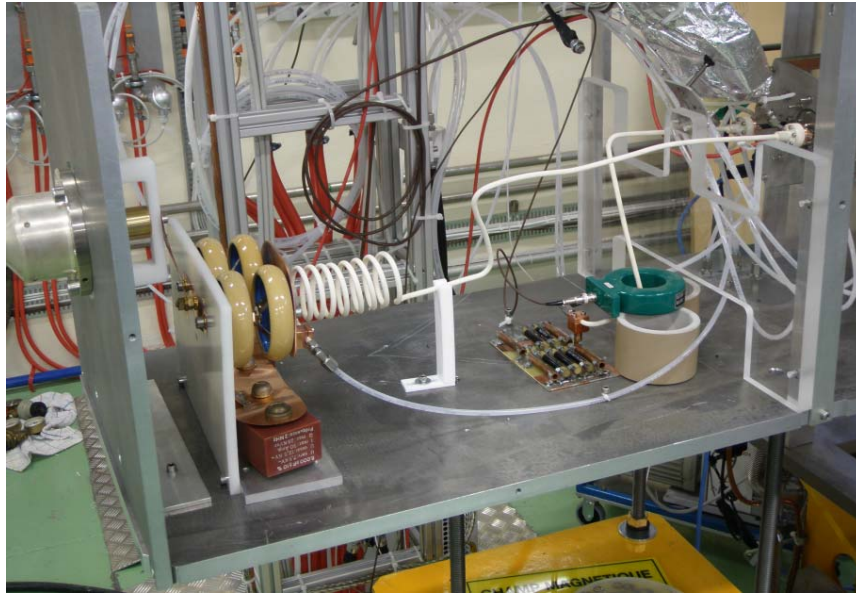
Figure 35: RF matching network.

Figure 36 shows the overall circuit and the corresponding relations. The antenna is basically a coil and thus characterized by its own inductance and losses (L_{ANT}, R_{ANT}). In series with this impedance the plasma contribution can be modeled as additional inductance and resistance (L_{PLASMA}, R_{PLASMA}). To provide adequate loading to the final amplifier the sum of the two individual contributions must be transformed into R_M=50 Ω (see Figure 36). As the system is almost working at a fixed frequency this is achieved by adding a series and a parallel capacitor (C_S, C_P). Obviously, good matching conditions can only be obtained either with or without plasma, but not at the same time. The additional lumped coil (L_S, R_S) makes the tuning of the circuit easier. The circuit is then connected to the transmission line and the final amplifier output.

The component values of the SPL plasma generator matching network are listed in Table 3. All of them have been characterized with low level measurements and the overall circuit response cross-checked with PSpice simulations. Details on these measurements are given in Ch. 8.
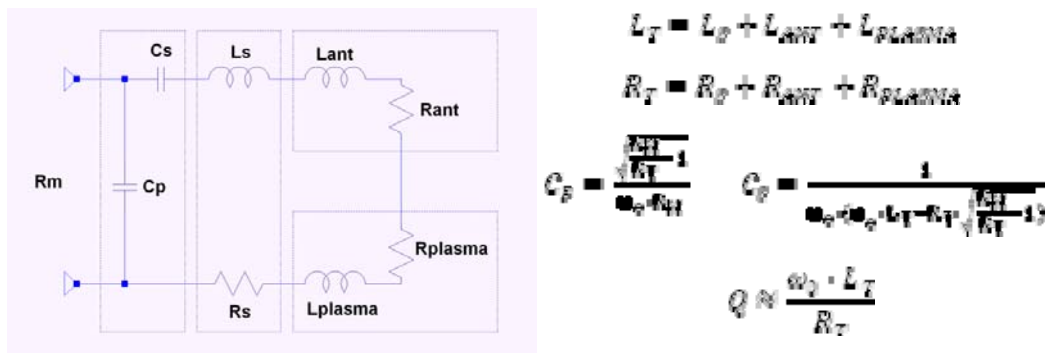
Figure 36: Matching network and antenna circuit, indicating the nomenclature of the individual components.

Table 3: Summary of matching network parameters.

L_{ANT}	2.4 µH
R_{ANT}	0.15 Ω
L_S	2.22 µH
R_S	0.14 Ω
C_S	1.505 nF
C_P	14.5 nF
Cable Z_0	50 Ω
Cable length	34.1 ns

3.7. Power supplies and plasma light amplifier

The test stand comprises two pulsed and two cw power supplies for various subunits of the SPL plasma generator, plus two modules for optical measurements.

The ignition pulser power supply (Fug MCP 140-1250) delivers a pulse of up to 1000 V limited to 10 A for a duration of up to 100 µs at a maximum rate of 50 Hz. A +1000 V DC supply is backed by capacitors, the output is switched using a high voltage bipolar MOSFET. A selectable series resistor limits the output current.

The Piezo valve is driven by an in house assembled power supply capable of delivering -10 V to +100 V. The power supply has two inputs which are both amplified 20x then summed. Using an arbitrary waveform generator on one input and a DC level on the other any combination of DC offset and pulse shape is possible to drive the valve.

The Plasma extraction plate and Collar electrode supplies are identical and consist of a Fug NTN 140-65 +/-65 V 2 A DC supply. The output of the power supplies is backed by a 22000 µF capacitor to allow a peak current of 10 A for 1.2 ms during the beam pulse and to limit the voltage droop to 2% when operated at 30 V.

The photosensor power supply comprises three photosensor modules housed in a 19" chassis. Each module consists of a Hamamatsu H10722 photomultiplier and optical filter assembly powered with +/-5 V dDC which is generated by a DC-DC convertor from a +5 V DC supply. The gain is controlled by a 10 turn potentiometer connected across the photosensor's 1.2 V reference output. The gain setting is monitored on a precision 4 1/2 digit LCD voltmeter module. The analog output signal is then connected directly to an oscilloscope.

The plasma light amplifier comprises a receiver module containing a photodiode and an amplifier providing an analogue output signal proportional to the visible light intensity for display on an oscilloscope. A comparator circuit triggers a digital pulse generator stage with an adjustable delay and pulse width when the light intensity passes a preset threshold. The digital output is then available to indicate the presence or absence of the plasma.

3.8. Magnetic field mapping

As noted in Sect. 2.6, different types of cusp magnets (Halbach elements and standard N-S magnetized ones) have been ordered from two different producers. For quality assurance a magnetic field measurement test stand has been set up. This test stand is fully automated and includes 3 remotely controlled motorized linear drives as well as a rotary stage. A three axis Hall magnetometer (Metrolab

THM1176) with integrated temperature sensor is used for magnetic field measurements. The sensitivity of the Hall probe ranges from 0.1 mT to 20 T and is therefore suitable for near- and far-field measurements. The movement of the linear and rotary stages and the read out of the Hall probe is controlled by a LabView program. A MatLab script is used for data analysis. The positioning accuracy of the Zaber stages is ±8 µm whereas the magnet positioning and mechanical stability of the Hall probe combine to a reproducibility of ±0.1 mm. Positioning is thus the most crucial task when performing a measurement.

Two setups have been realized. For the measurement of single magnets, the magnet is fixed at a predefined position and a 3-dimensional field scan performed by using the three linear drives for x-y-z movement of the Hall probe. For measuring of the cusp field of the octopole and dodecapole magnet cages, the linear stage assembly is changed, and the cage mounted on the rotary stage where a mechanical centering disk is used to align the cusp. Figure 37 illustrates the two measurement setups. Figure 38 shows a typical field map from single magnet measurements and a comparison with simulated data. Figure 39 illustrates the field distribution inside the dodecapole magnet cage.
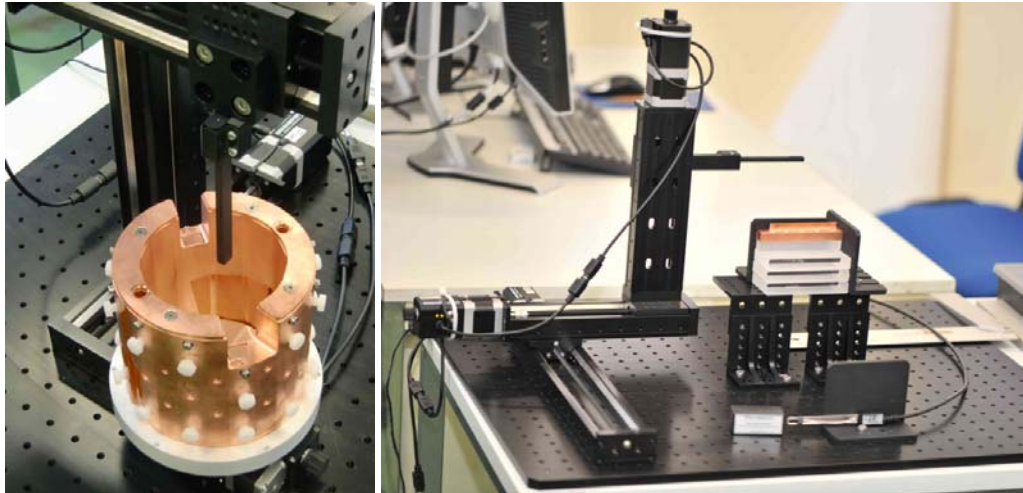
Figure 37: Magnetic field measurement test stand. Cusp field measurement setup with magnetic cage on rotational table (left) and single magnet measurement setup (right) here with a copper shielded magnet.
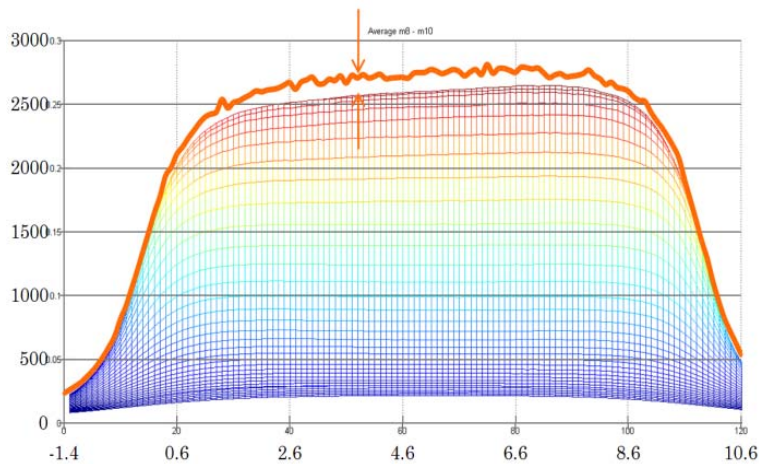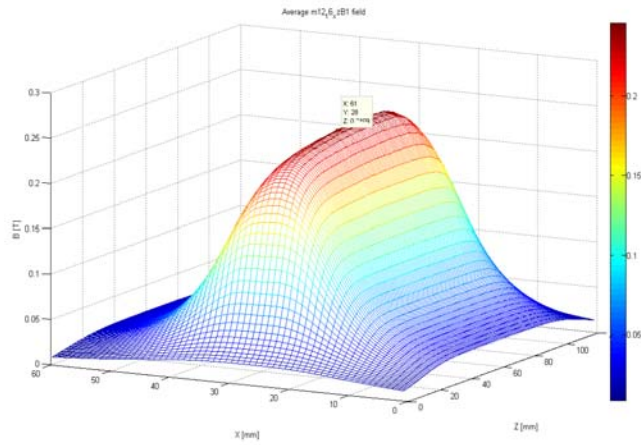
Figure 38: typical field maps of a single magnet measurement (B total or B perpendicular to the plane?) in a parallel plane 5.5 mm above magnet surface (top) and comparison of measurement data to simulation results (bottom) which shows a deviation of only 2-3 mT (10%) most probably introduced by the magnet strength and positioning. In the lower image, the units of the ordinate and the abscissa are cm and Gauss, respectively.
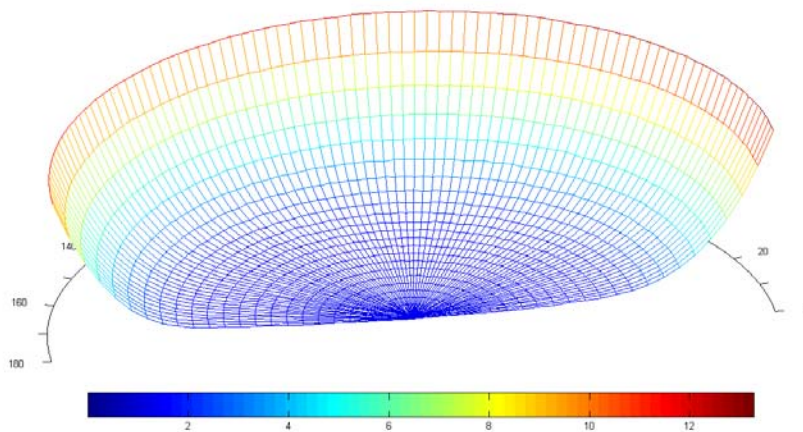
Figure 39: Polar coordinate field map of the total magnet field in the plasma area for the dodecapole magnet cage equipped with 12 Vacuumschmelze N-S magnets. The outer measurement radius (24 mm) corresponds to the inner diameter of the AlN plasma chamber. The colour scheme gives the B-field strength in mT.

34

3.9. RF heating test bench

A test bench has been designed and fabricated in order to study the power dissipation by eddy currents in the magnetic components of the SPL plasma generator [7]. A 3D view of the test bench is shown in Figure 40. The test stand contains a number of slots for shielded and unshielded cusp and filter magnets. Furthermore, it allows the insertion of ferrites to assess their influence on magnet heating and to estimate hysteresis losses. The RF field is produced by a water-cooled antenna of the same dimensions and number of windings as the one used in the SPL plasma generator. Except for the base plate and the Faraday cage, all test stand components are made of poly-methyl methacrylate (PMMA) in order to avoid unwanted shielding effects. During testing, the temperatures of the installed magnets and ferrites are constantly measured by means of thermal imaging. All measured surfaces have been partly painted with the same type of black paint in order to uniformize their emissivities ε. Using a water bath with defined temperature, $\varepsilon \approx 0.80$ has been determined for the paint. In order to assess the reduction in power dissipation by shielding the magnets, boxes made of 0.5 mm thick Cu have been produced for one cusp magnet and one pair of filter magnets (Figure 41).
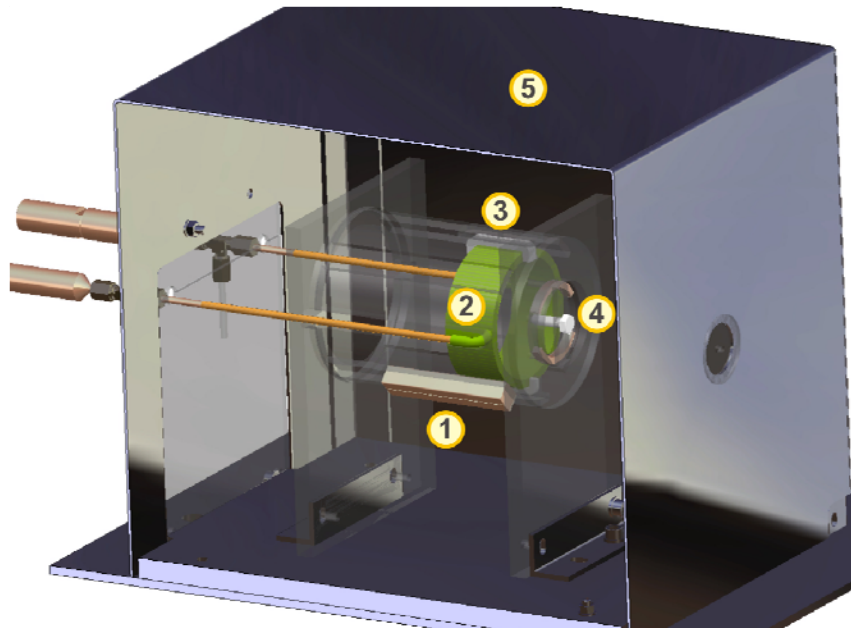
Figure 40: Layout of the test bench for power dissipation measurements. 1: cusp magnet. 2: antenna. 3: ferrite. 4: filter magnets. 5: Faraday cage.

Figure 41: Cusp magnet with Cu housing used in the RF heating tests.

3.10. Plasma diagnostics

Many of the plasma parameters, such as the plasma potential, the electron and ion densities, and their temperatures, have an influence on the beam extracted from an ion source. In the particular case of an H^- source, the extracted beam current and the beam emittance are influenced by these parameters because the efficiencies of H^- production and destruction and the co-extracted e^- current depend critically on the plasma conditions. Therefore, plasma diagnostics is an important tool for characterization, understanding and optimization of an H^- source.

In the SPL plasma generators, the following invasive and non-invasive diagnostic devices and techniques are available:

Optical spectrometry of the visible light generated by the plasma. Of particular interest are the emission lines of the Balmer series of atomic hydrogen, and the emission bands originating from molecular hydrogen at optical wavelengths. In addition, optical spectrometry helps also in tracking down plasma impurities (residual gases, atoms and compounds sputtered away from the walls) that leave their fingerprints in the wavelength regime covered by the spectrometer and the optical system.

The plasma light is captured by a lens head into which a quartz fiber is glued. Lens head and fiber can be mounted opposite of the plasma generator either in front of the quartz window, or in a dedicated holder coupled to the inside of a DN-150 flange.

Plasma spectrometry can be performed with a fast ($\geq$ 4 ms integration time window) spectrometer (Ocean Optics 4000) with standard SMA connector for a quartz fiber. A database of elemental and molecular spectral lines for line identification is available. Alternatively, the light can be transmitted to the plasma light amplifier to monitor the total plasma light intensity. This amplifier also creates a trigger signal when the plasma light intensity is above a threshold value which can be used for RF frequency switching (see also Sect. 3.6). As an additional option, single emission lines and bands can be selected by a number of optical filters, and their intensity recorded by a photomultiplier tubes (PMTs). Two beam splitters allow the measurement of more than one emission line at once. Several filters with central wavelengths between 400 and 650 nm can be used to study the time development and intensity of the most important Balmer lines (H_α, H_β, H_γ and H_δ). Additional absorbers help reducing the light intensity of the strongest emission lines (mainly H_α and H_β) to a level that can be handled without problems by the PMTs.

The interpretation of the spectra (determination of ion densities, electron densities, and temperatures, etc) requires a collisional radiative model of the plasma such as the one developed at the Max Planck Institute of Plasma Physics, Garching, Munich.

Rest gas analyzer: the QMA 125 can be operated for gaseous elements but also in plasma monitoring (ions and neutrals) mode as it is placed in direct view of the plasma.

Langmuir probe: Langmuir probe measurements are the most established method for measuring the plasma potential, electron and ion densities and temperatures. A Langmuir probe (Henniker Scientific Impedans ALP RF-300) with RF broadband compensation and 80 MHz sampling rate has arrived, it will be used to measure these data during operation. The Langmuir probe comprises vacuum bellows and a linear drive that allows axial movements over a range of 450 mm. The system will be mounted on the flange opposite to the plasma generator so that the probe tip can access the plasma volume through the aperture of the plasma electrode. Off-axis

measurements are currently not foreseen because of the sensitivity of the measured parameters on magnetic fields, and difficulties in off-axis probe positioning.

RF-coupling: The RF generator presented in Sect. 3.6 can provide a 2 MHz RF signal with up to 100 kW power. However, in reality not all the RF power is used for plasma heating as a fraction of RF power is always reflected or dissipated elsewhere in the circuit. In order to measure the power coupled into the plasma and to characterize it continuously, the forward and reflected voltage and the antenna current are simultaneously recorded by an oscilloscope and analyzed by a MatLab script. Together with the measured matching network parameters (see Sect. 3.6), this yields time resolved values for the plasma impedance, plasma resistance, and the reflected power.

3.11. Timing

The timing of the experiment is based on two 8-channel pulse generators (Quantum Composers QI-9520). One pulse generator triggers all power supplies involved in the plasma generation (piezo valve, plasma ignition, RF antenna, extraction collar). The second pulse generator is used to synchronize the measurement systems (oscilloscopes, rest gas analyzer, photo camera, optical spectrometer, and Langmuir probe) with the experiment. An outline of the timing system is presented in Figure 42.
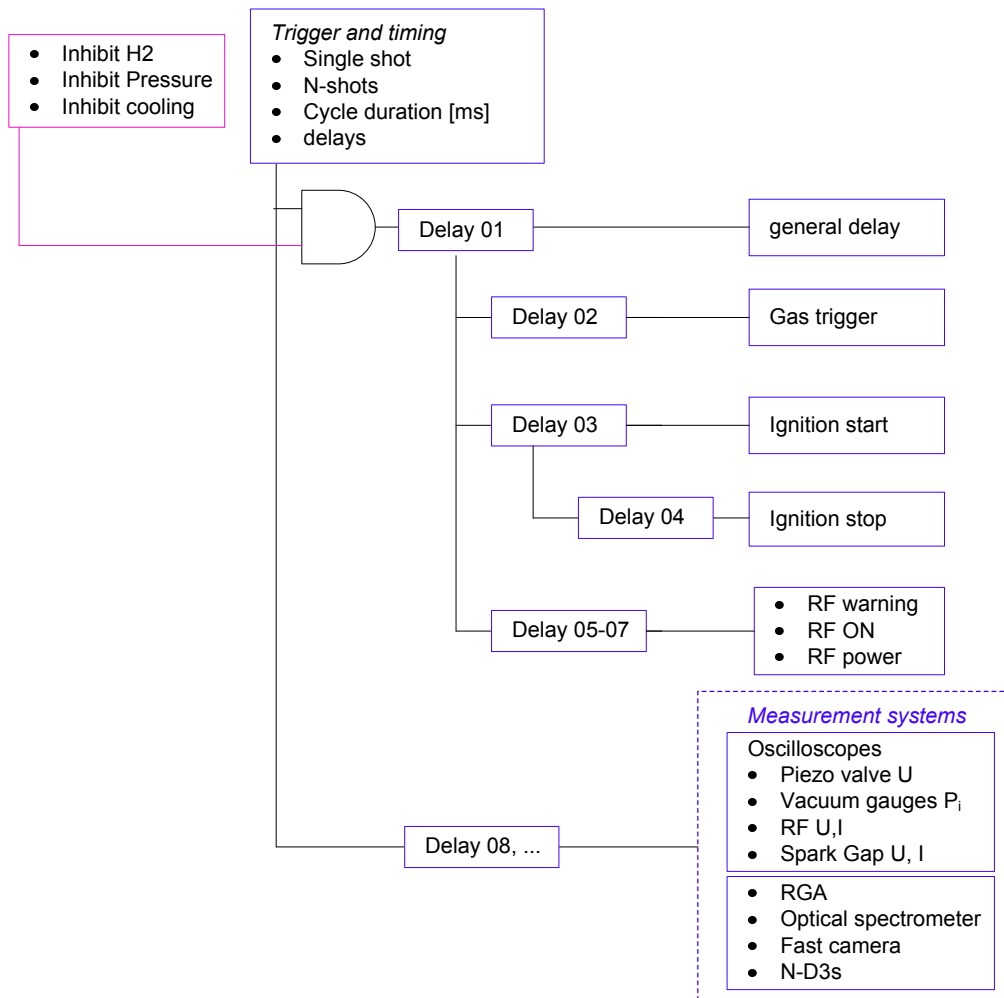
Figure 42: Triggering system of the plasma generation and fast data acquisition.

3.12. Slow control and data storage

The test stand involves a data acquisition (DAQ) system for slow control and processing and storage of experimental data. A schematic outline of the DAQ system is shown in Figure 43. It involves input and output modules connected to a PLC with Step7 configuration for data processing, and a Labview program that monitors and stores the data from the sensors in real time, visualizes the status of the interlock system, and regulates the piezo valve DC offset. The data exchange between Labview program and PLCs is achieved via Ethernet. The PLC is responsible for reading sensors, making operations and executes the safety interlock system (see Sect. 3.13).
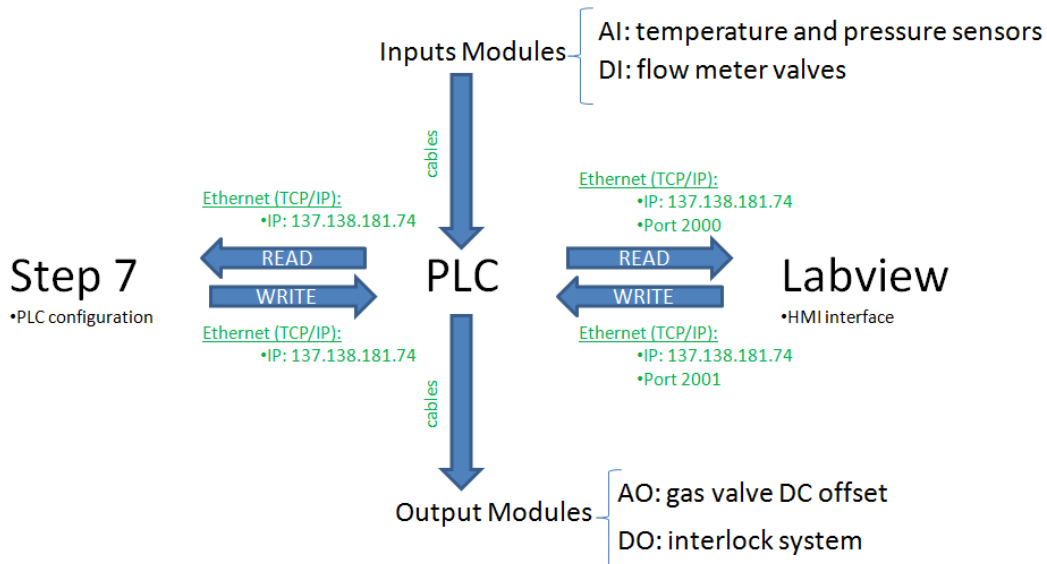
Figure 43: Outline of the Step7 and Labview based slow control data acquisition chain.

3.13. Safety Interlock system

The main task of the safety interlock system is the prevention of damage to the equipment during operation and to minimize the risk of life-threatening hazards during an intervention. The PLC is responsible for executing the interlock system. For testing and certain operation modes (e.g. operation of the mockup or the RF heating test bench), one or more hardware overrides can be set manually. A safety switch included in the Labview interface assures that the manual overrides are not activated accidentally. The interface also monitors the state variables of the interlock system in real time. The hardware protection interlock system that disables the RF system and the power supplies is triggered in the case of one of the following events:

- the gas safety system triggers a gas alarm (see Sect. 3.3)
- the outlet temperature of the cooling water rises above 70 °C for any of the cooling circuits
- the coolant flow is lower than a threshold value for any of the cooling circuits
- the N_2 flow is below 5 l/min
- the pressure inside the plasma chamber is larger than 10 mbar
- the Labview monitoring and data acquisition system of the experiment (see Sect. 3.14) stops working.

Figure 44 shows a screenshot of the Labview interlock system real time interface.
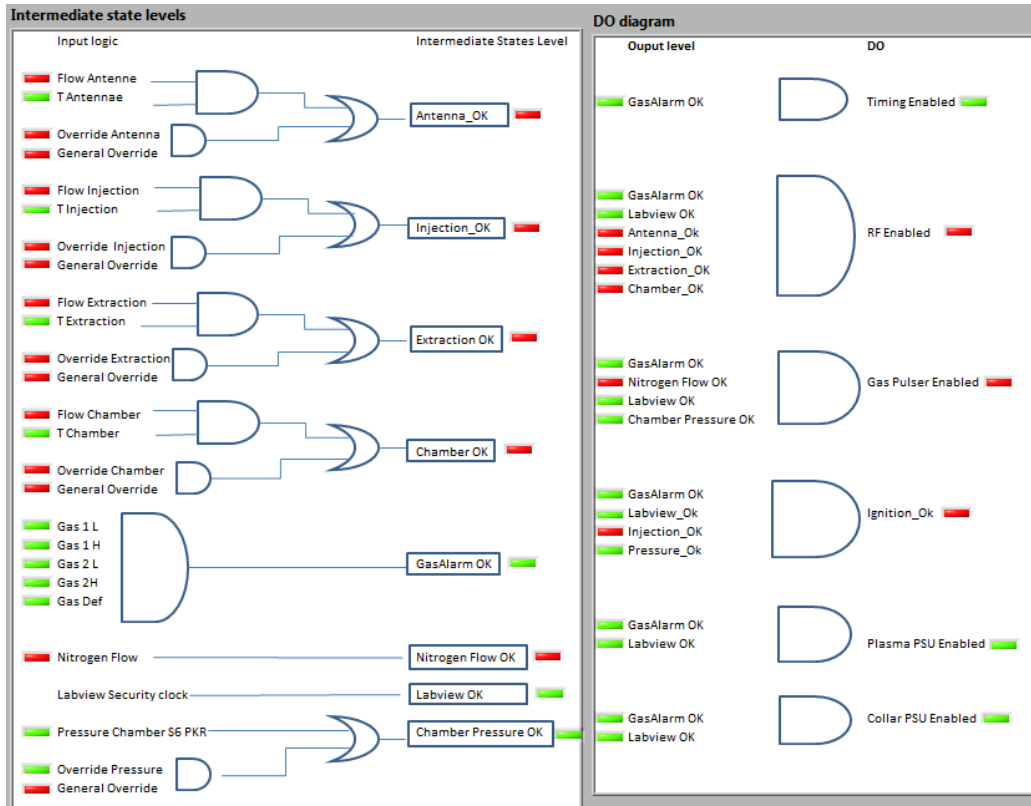
Figure 44: Screenshot of the Labview interlock system real time interface.

3.14. Monitoring and data acquisition system

The interface screen of the Labview program is divided into several tabs which control the writing of data into the PLC, serve as interface for the interlock system, show real-time graphics of pressures and temperatures, calculate and visualize the heat flow, and allow to configure the program.

The Labview program is also responsible for storing the data in a file. This data file is saved by default in a folder located on a CERN server, which avoids losing data in the event of a computer crash. Data storage is performed during each Labview iteration, whose period is set to once per second. The data stored during each Labview iteration is summarized below:

- The PLC time and real time of the measurements
- the readings of the three pressure gauges installed at the experimental chamber
- the cooling water inlet temperature and the outlet temperatures of each cooling circuit
- the temperatures of the equipment
- the Hydrogen and Argon backing pressures
- the analog output values of the PLC
- the interlock system variables states.

39

4. Magnetic field configuration and permanent magnet characterization

The magnetic cusp field is created by a multipole arrangement of permanent magnets. It confines the plasma within the chamber, protects the chamber walls from critical heat loads, and increases plasma density. A higher order magnetic multipole (8-12 poles) was chosen to ensure a strong field gradient near the chamber walls for improved confinement (see Sect. 2.6).

To determine the size, type and configuration of the cusp field, simulations with the TOSCA module of VectorFields Opera© have been performed. The SPL plasma chamber cusp field was dimensioned such that the strength and orientation of the magnetic field close to the plasma chamber wall and within the plasma area resembled that of the Linac4 source as closely as possible. As a consequence of the larger outer diameter of the SPL plasma chamber and the presence of the cooling sleeve, the distance of the magnets to the inner wall of the plasma generator is considerably larger than in Linac4: While in the Linac4 source the radial distance of the magnets from the center of the plasma chamber is 35 mm, it is 46 mm (dodecapole) and 49.5 mm (octopole), respectively, for the SPL plasma generator. This would result in a drastic decrease of magnetic field strength near the chamber walls if the same types of magnets would be used.

As the mechanical constraints prohibit a sufficient increase of magnet size, a Halbach-type configuration was used to enforce the magnetic field towards the source center. In this configuration, the standard N-S magnets are replaced by 13.5 x 10 x 99 mm sized offset-Halbach elements consisting of 3 magnets of size 4.5 x 10 x 99 mm. The magnetization directions of these magnets are visualized in Figure 45.
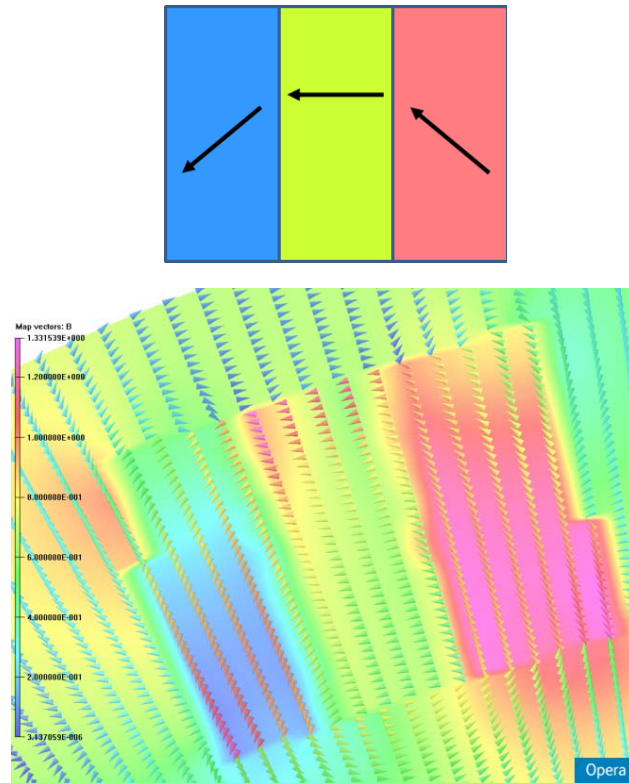
Figure 45: Top: Magnetization direction in an offset Halbach element with offset angles of 45 degrees. Bottom: Cut through a simulated Halbach element, showing the field vectors. In both cases, the Halbach elements are aligned in counterclockwise direction.

A Halbach element can have a clockwise (cw) or counterclockwise (ccw) orientation. In order to create the multipole cusp configuration, cw and ccw oriented Halbach elements are alternately positioned around the plasma chamber. Between the Halbach elements the magnetic field is purely radial. The U-shaped ferrites located at this position reinforce these radial components.

Figure 46 shows a magnetic field plot along a cut through the plasma chamber and the transversal B-field strength along the chamber wall for this cutting plane. Small perturbations of the maximum field strength in the range of ± 5% are present. These are due to missing ferrites at the positions of the antenna tips, and to two magnets that had to be shortened because of the plasma chamber cooling outlet (Sect. 2.4). The field strength drop from chamber wall to center is shown in Figure 47 for the dodecapole and the octopole magnet configurations.

According to the simulations, the magnetic field strength drops from more than 19 mT at the chamber wall to a few µT in the center. The non-zero field strength is possibly due to the smaller number of ferrites compared to the cusp magnets which effectively leads to a superposition of a dipole field onto the multipole cusp field.
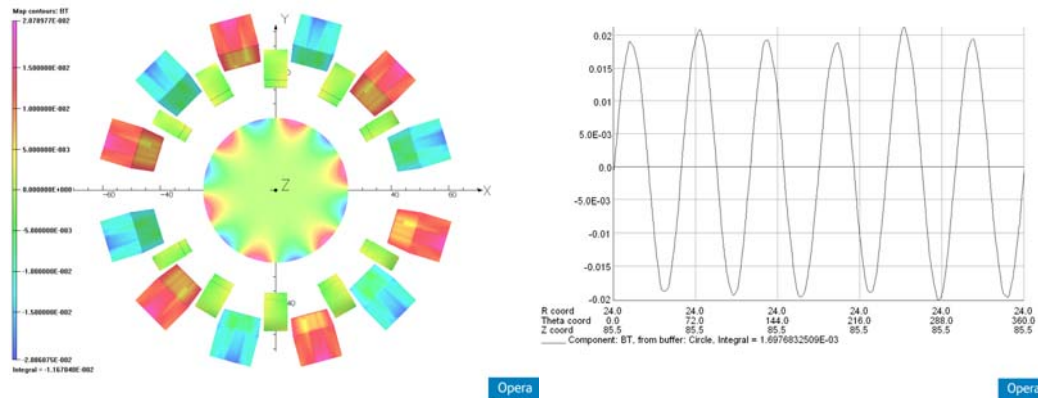
Figure 46: Left: Dodecapole configuration of Halbach elements with NiZn Ferrites (green) and a magnetic field map in the chamber. Ferrites are shown in green, cw and ccw oriented Halbach elements in red and turquoise, respectively. Right: Tangential magnetic field along the chamber wall at the circular edge of left field map, both plotted for z = 85.5 mm which corresponds to the center of the RF antenna. All fields in Tesla.
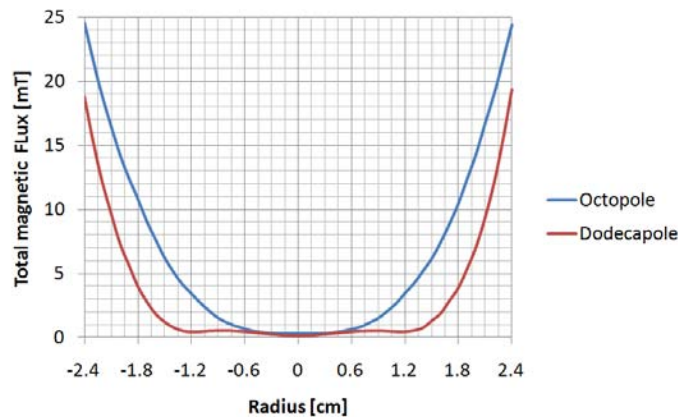
Figure 47: Radial plot of the total magnetic field across the plasma chamber for the dodecapole (red) and the octopole (blue) magnetic configuration.

The calculated field maps can be used to study the confinement effect on single electrons. In order to visualize the electron confinement, a 40 mm wide beam of 5 eV electrons originating in the center of the plasma region was simulated. Figure 48 shows the electron trajectories for different configurations after numerous reflections. Despite an asymmetry introduced by the initial conditions, the electron loss lines are well characterized. The simulations indicate a possibly better plasma confinement for the SPL configurations.

The lower right picture of Figure 48 shows a photograph of the plasma chamber of the SPL plasma generator after operation at 50 Hz, 1.2 ms and up to 50 kW RF power with the octopole magnetic configuration. The observed loss lines correspond directly to the radial field maxima of the simulations where most electron losses are expected.
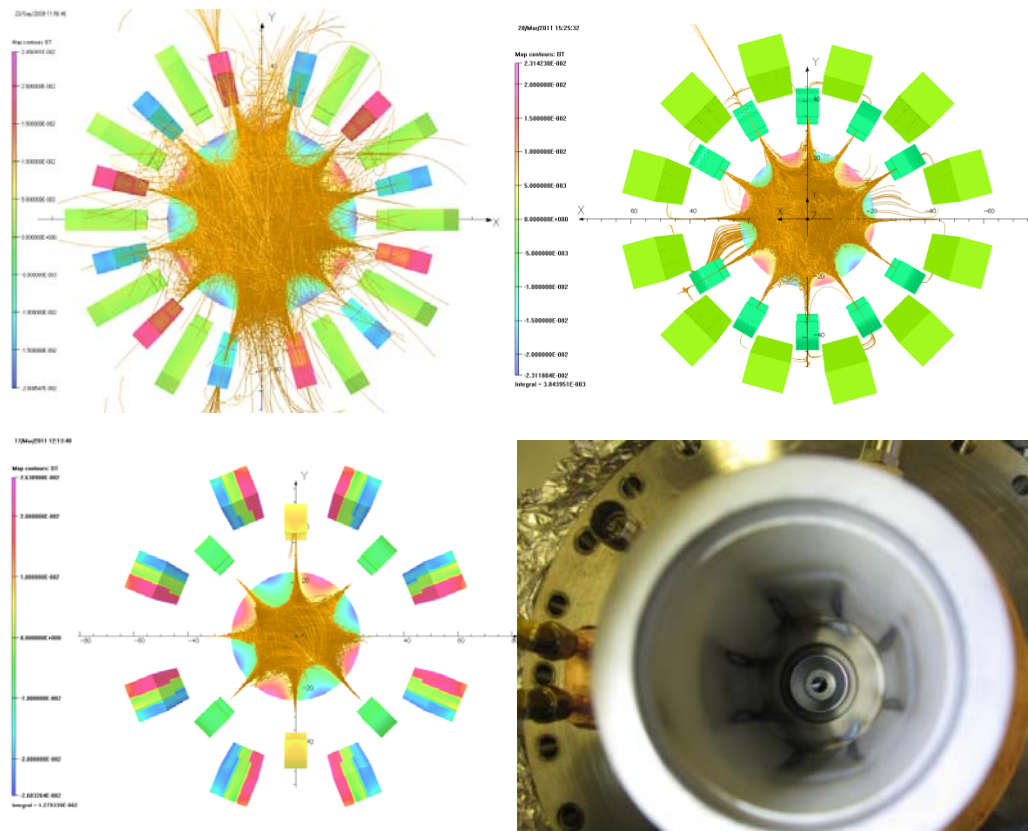
Figure 48: Visualization of electron confinement in the Linac4 source (top left), the SPL plasma generator dodecapole Halbach cusp configuration (top right), and the SPL plasma generator octopole Halbach cusp configuration (bottom left). The image at bottom right shows the losslines inside the plasma chamber after high power operation with the octopole cusp configuration.

5. Hydrogen plasma characterization and monitoring

Invasive methods such as Langmuir gauge measurements provide key information on the plasma electron density and temperature, however the geometry of the Linac4 H^- source and the SPL plasma generator prevents a use during high voltage operation. Besides this, operation and tuning of an H^- source is likely to benefit from non-invasive diagnostic methods, such as monitoring of the plasma optical emission and the RF coupling into the plasma. These features should therefore be implemented into the control system of the Linac4 and SPL H^- ion sources.

The Optical Emission Spectroscopy (OES) technique applied to the determination of H^- ion densities in hydrogen plasma ion sources was proposed by Fantz and Wünderlich [10]. The monitoring technique relies on measurement of the H_α, H_β and H_γ lines. As shown in [10], the Balmer line intensities can be used to determine the H^- and e^- densities and their temperatures. However, a time dependent collisional radiative model adapted to the plasma conditions in the Linac4 source and the SPL plasma generator will be required in order to allow for such a type of analysis.

The light collection geometries in the Linac4 source and the SPL plasma generator are illustrated in Figure 49. In both cases, the collected plasma light is transferred to the photo detector or spectrometer by a shielded quartz fibre. Generally, the quartz viewing port of the Linac4 source copied from the design of DESY proved to be very efficiently collecting the plasma light, whereas the light intensity detected in the SPL plasma generator through the aperture of the plasma electrode turned out to be relatively low. For both systems, the short pulse duration was a challenge in the measurements. This motivated the selection of a trigger able fast spectrometer, a photodiode amplifier, and photomultipliers. The significant difference between the light collection geometries should be part of a future detailed analysis.

The first results of light emission measurements obtained on the Linac4 ion source and during the commissioning of the test stand were published in [8] and are presented in the following sections. As the plasma conditions and therefore, plasma light emission are likely to be influenced by the extraction of H^- and e^- from the ion source during H^- pulses, all measurements presented herein were performed with an unbiased extraction system.
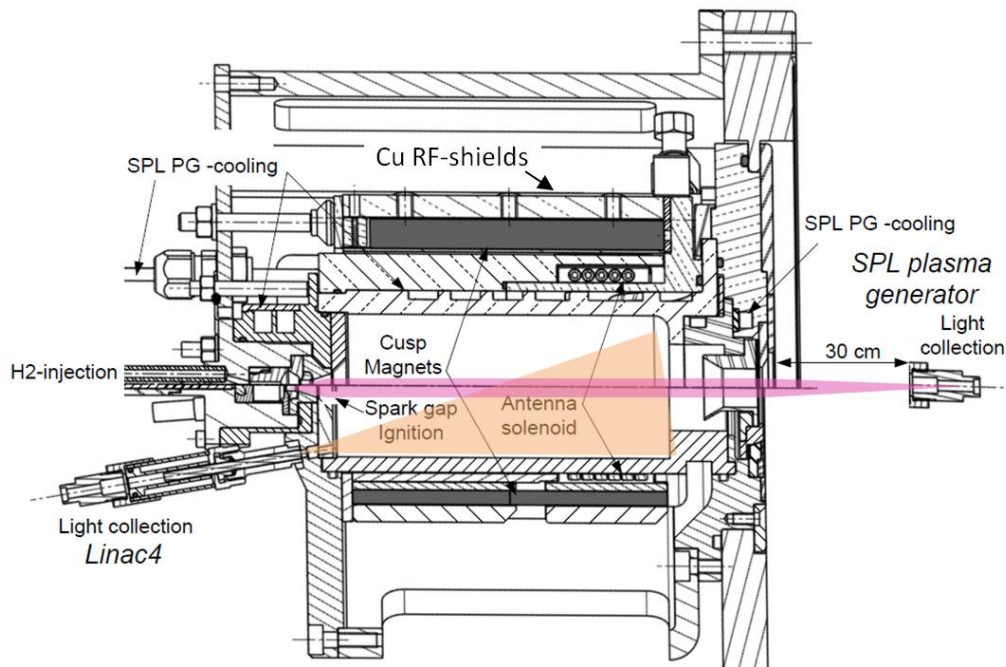
Figure 49: Illustration of the differences induced by the cooling and magnet shielding between the SPL plasma generator (top) and the Linac4 ion source (bottom). The quartz viewing port of the Linac4 plasma chamber and the direction of light collection of the SPL plasma generator are indicated.

5.1. Plasma light measurements results

The potential of the method is illustrated in the following paragraphs via measurements made on the Linac4 ion source operated without ion or electron

extraction and on the SPL plasma generator. The light signals were collected by a SFH250 photodiode coupled to a tunable amplifier.

As pointed out in Sect. 3.6, the RF frequency is switched at the beginning of the RF pulse in order to optimize the coupling during plasma ignition and during the pulse. The effect of the RF frequency switch operation mode is illustrated in Figure 50 for the Linac4 source. The frequency at which best ignition conditions are met (1.946 MHz for the assembled source and matching network) differs from the frequency at which the best energy transfer is obtained (2.0 MHz). Consequently, the most stable plasma conditions are obtained while starting the RF at 1.946 MHz and, on plasma light appearance, switching to the plasma tuned frequency. This is confirmed by the light measurement which also illustrates the plasma ignition delay resulting from operation at 2.0 MHz alone.

Figure 51 presents the piezo valve and RF power control signals, the plasma ignition spark gap current and the clearly separated light signals issued from the spark gap current and from the RF heated plasma. Trends on variation of operation parameters are illustrated in Figure 52 by means of measurements achieved at the Linac4 source. The RF coupling efficiency during these measurements was 70% according to ref. [9]. Clearly, the figure shows that the light intensity is growing as a function of the RF power in a non-linear fashion. More light is gathered for 2.0 MHz operation than for 1.946 MHz operation, hinting again at better RF coupling with 2.0 MHz. A similar behavior was observed in the SPL plasma generator.
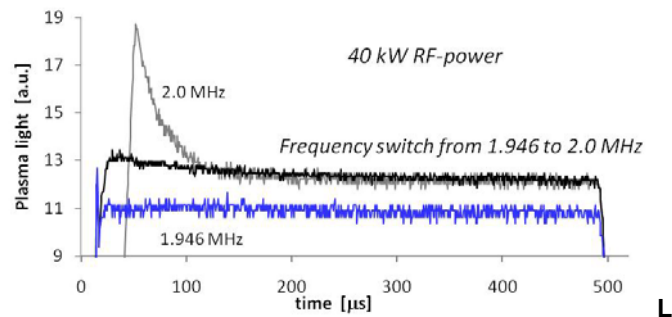
Figure 50: Light emission of the fastest ignition RF frequency (1.946 MHz), best energy transfer RF frequency (2.0 MHz) and switch from 1.946 to 2.0 MHz few μs after plasma ignition (note offset scale).
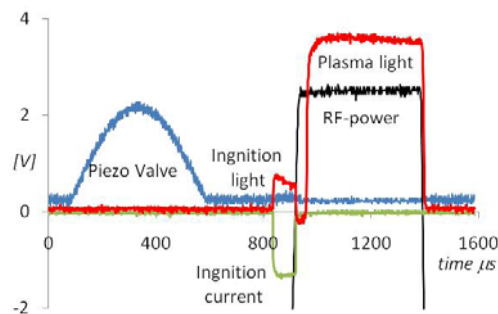
Figure 51: Ignition and plasma generator light emission at the SPL plasma generator, the gas valve signal, the ignition spark gap current and the 20 kW (2.06 MHz) RF power control pulse are shown.

44
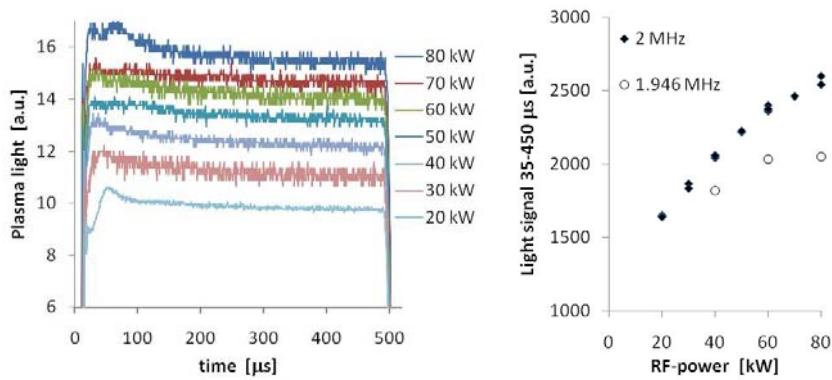
Figure 52: Left: Plasma light intensity recorded for 0.5 ms RF-pulse duration at the Linac4 ion source. The RF frequency is switched from 1.946 to 2.0 MHz at plasma ignition, its power is indicated. Right: Evolution of the light intensity (integral from 350-450 µs) at RF-frequencies of 1.946 and 2.0 MHz.

5.2. Emission spectrometry measurements

Emission spectrometry measurements were obtained with a fast Ocean Optics USB4000 spectrometer (Figure 53). The acquisition window of this spectrometer can set as low as 4 ms. The dynamic range of this spectrometer of slightly below two orders of magnitude. In order to avoid saturation of the H_α and H_β lines during our measurements at the Linac4 source, a two orders of magnitude aperture reduction obtained by a 0.2 mm diameter diaphragm was introduced and provided good measurement conditions for both lines.

The RF-power dependent H_α and H_β intensities and the H_β/H_α ratios are presented in Figure 54 for measurements at the Linac4 source. The intensities of both lines increased linearly with the RF power. The H_β/H_α ratio measured for the flat section of the 0.5 ms pulses increased with RF power (20-80 kW) from typically 6 to 14 %.

Figure 53: Trigger able fast spectrometer Ocean Optics USB4000 featuring a minimal light collection time of 4 ms and a dynamic range of typically 60. Also visible are the USB cable, the light fiber and the trigger cable.
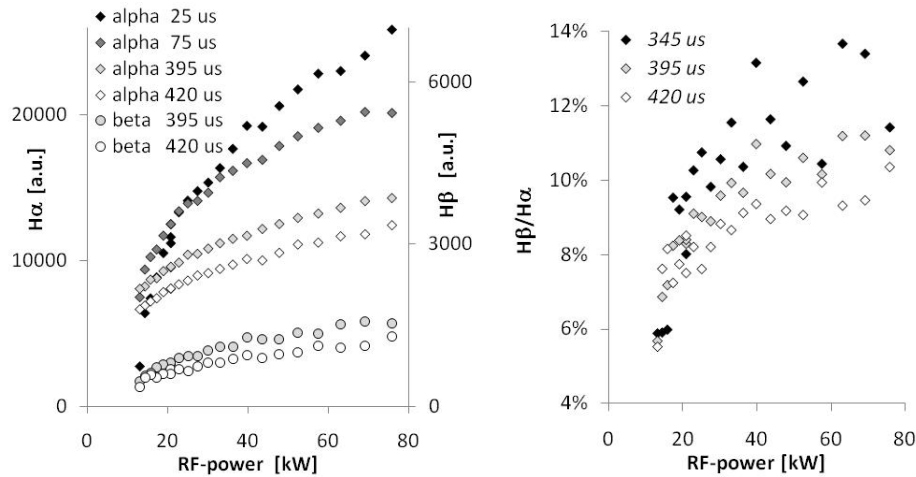
Figure 54: Left: H_α and H_β lines intensities measures at the Linac4 ion source. Right: H_β/H_α ratios extracted from these data. The average integration time [µs] is indicated.

The minimum integration time of the spectrometer of 4 ms is larger than the pulse durations in the SPL plasma generator and the Linac4 source (1.2 ms and 0.5 ms, respectively). In order to visualize the development of the line intensities during a pulse, integral measurements obtained by a variable delay trigger of the 4 ms acquisition window were derived. The delay trigger was set such that the acquisition window covered only a fraction of the pulse. The rise of the plasma light was measured by approaching the end of the measurement window and the plasma light tail by moving the start of the acquisition window. By scanning the setting of the delay trigger and differentiating the measured intensities, a time-resolved signal could be retrieved.

The results of measurements at the SPL plasma generator are presented in Figure 55. An RF power of 20 kW was used. The time resolved measurements of the H_α and H_β line intensities exhibited a delayed rise of the H_β line of typically 100 µs. The delays of the H_γ and H_δ lines were even larger and amounted to 150 µs and 200 µs, respectively. The H_β/H_α ratio increased from 0% to an average ratio of 18% between 200 and 500 µs and then, dropped smoothly to 17% by the end of a 1.2 ms pulse.

Figure 55 shows that at least four orders of magnitude dynamic range are required to cover the H_α, H_β, H_γ and H_δ lines during a measurement without saturating the H_α line. The technical solution chosen to cover this dynamic range is shown in Figure 56. The measurement system is based on narrow band filters covering one Balmer line each, Wratten filters acting as absorbers and Hamamatsu H10722 photomultipliers and makes real time measurements of up to three Balmer lines at once possible. The amplifiers of the photomultipliers can be tuned individually and allow for a band width of up to 2 MHz.
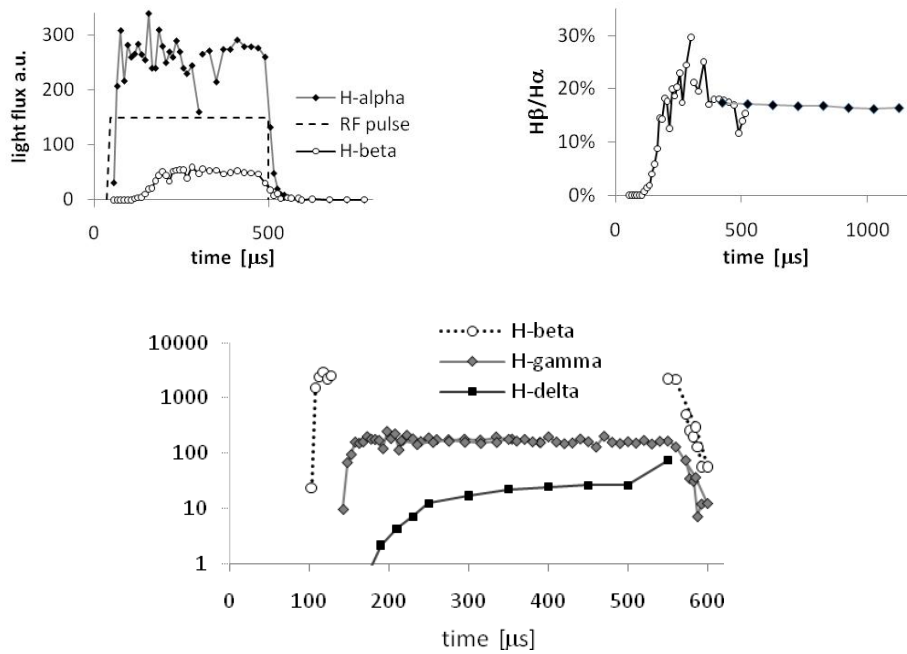
Figure 55: Upper left: H_α and H_β line profiles measured on the SPL plasma generator heated by a 20 kW RF power pulse of 500 µs duration. Upper right: H_β/H_α ratio derived from the line profiles (white circle) and H_β/H_α ratio measured over the last 150 µs of plasma pulses from 500 µs up to 1.2 ms duration (black diamonds). Bottom: Illustrative measurement of the delayed appearance of the H_β, H_γ and H_δ lines. The ordinate gives the intensity in log scale.

Figure 56: Real time measurement of up to three Hydrogen lines will be achieved with the Hamamatsu phototubes light detection system. The optical fiber is connected through a filter (10 to 40 nm FWHM) and attenuation box. The amplifier gain is tuned individually with a 10 turn potentiometer; its driving voltage is indicated at the mV level.

6. Analysis of the thermal equilibrium

During testing of the SPL plasma generator and the magnet heating test stand, the temperature distribution was constantly monitored at various positions with the Fluke Ti32 thermal camera. Wherever feasible, the measured surfaces were painted with black paint ($\varepsilon = 0.8$) in order to eliminate the effect of different surface emissivities.

47

6.1. SPL plasma generator

Thermal camera measurements were performed for the magnet cage, ferrites, and, by viewing through the Germanium window, also for the collar region (Figure 57). Measurements were done during both low duty cycle and high duty cycle runs, with the emphasis on the latter. Monitoring the surface temperatures with increasing average power allowed for the validation of thermal models, and for the identification of possible weak spots of the current design from the thermal point of view. In parallel to the thermal camera measurements, the cooling water inlet temperature and the outlet temperatures of each cooling circuit monitored by the DAQ system made it possible to assess the power dissipated on each component of the plasma generator.
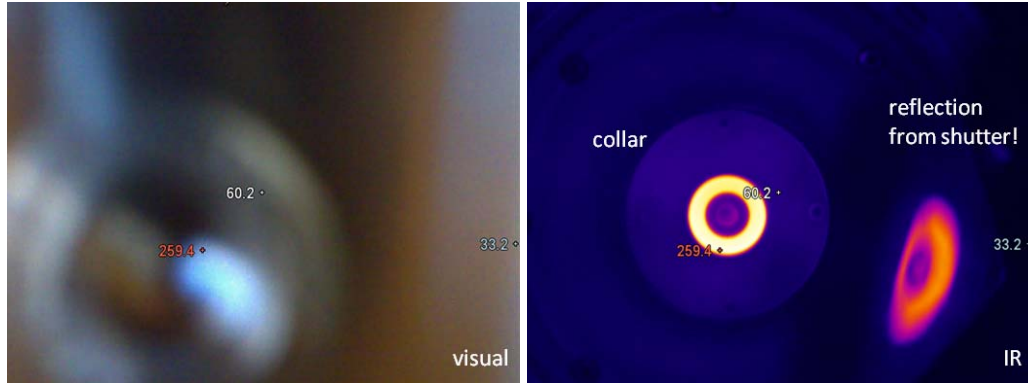
Figure 57: View through the Germanium window with the thermal camera. The window is opaque in the visual range (left image), but transparent in the infrared (right image). The given temperatures are calculated on basis of the thermal emission for ε = 0.8 were emissivity corrected before analysis. The hottest region corresponds to the AlN disk of the brazed collar.

6.1.1. Coolant temperature and dissipated power

Figure 58 illustrates the development of the cooling water temperatures during a typical test situation. This test was performed for the nominal pulse length (1.2 ms) and repetition rate (50 Hz) foreseen for HP-SPL operation. During the test, the RF power was increased stepwise from 20 to 50 kW. Since the matching conditions of the circuit change with increasing RF power because of a slight temperature dependence of the matching network parameters (Sect. 3.6), the RF frequency was tuned each time after changing the power settings. The increase of the piezo valve temperature was caused by heat conduction from the ignition element through the connecting gas pipe.

The outlet temperatures of the cooling circuits follow the increase in RF power very closely, implying that the fraction of total power dissipated per cooling circuit is approximately constant at each power level. If ΔT assigns the temperature difference between the cooling water inlet and outlet temperatures, the power dissipated in each cooling circuit during an RF pulse (P_{diss}) can be calculated by the formula

$$P_{diss} = \Delta T \cdot Q \cdot C_p / DF \tag{1}$$

Where Q is the coolant flow rate in l/s, C_p the specific heat capacity of water (C_p = 4181 J/kgK at 298 K), and DF the duty factor, i.e. the product of the pulse length in s and the repetition rate in Hz. Note that the inlet and outlet temperatures have to be corrected for instrumental effects (Pt-100 sensor offsets) before the calculation of ΔT to avoid systematic errors.
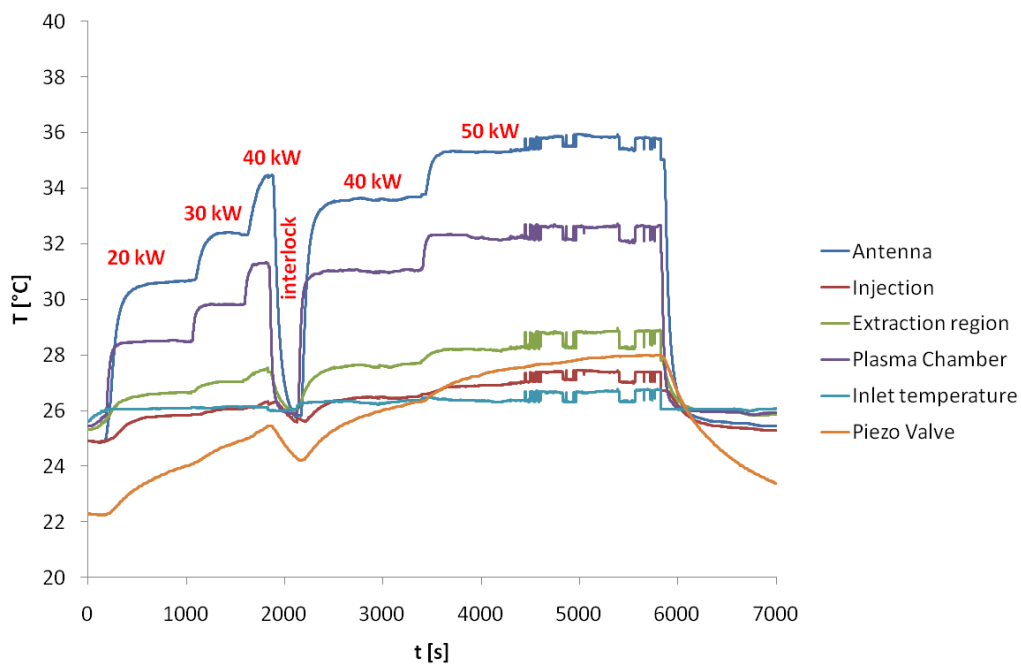
Figure 58: Development of the cooling water outlet temperatures during a typical test situation. During the test, the power was increased stepwise by 10 kW. The pulse length and repletion rate were 1.2 ms and 50 Hz, respectively. The drop observed at t ≈ 2000 s occurred after an interlock trigger that switched off the experiment temporarily.

6.1.2. RF settings and coupling efficiency

As discussed in Sect. 3.6, the shape of the RF signal and the RF power are defined by a function generator. The height of the function generator signal reflects the delivered RF power P_{RF} in a logarithmic scale. Accordingly, setting the upper level of the signal to 2 V should correspond to P_{RF} = 10 kW and an upper level setting of 3 V to P_{RF} = 100 kW. However, a calibration of the RF system was performed in order to assure that P_{RF} delivered by the RF generator does correspond to the predicted values.

The importance of the calibration of the RF system is outlined in Figure 59. This graph shows, for two series of measurements performed with the octopole magnet cage, the coupling efficiency for several RF power settings. In each case, P_{RF} was set by the upper level setting of the function generator signal. As before, the pulse length (1.2 ms) and repetition rate (50 Hz) used in the measurements correspond to the nominal values for SPL plasma generator operation.

The first series, measured before recalibration of the system, indicated that the coupling efficiency decreases with increasing RF power. This effect has disappeared in the second series which was measured after recalibration. This suggests that the apparent decrease in coupling efficiency observed in the first measurements originated from the calibration of the RF system.

Table 4 summarizes the power dissipated per cooling circuit for the second series of measurements and for P_{RF} = 20 kW and P_{RF} = 40 kW. The results show that between 50% and 60% of the total power are dissipated in the plasma. For the injection and the antenna, the fraction of dissipated power does not change with P_{RF}, while an increase with P_{RF} is observed for the plasma chamber and the extraction region.

The measured reflected power is of the order of 10% of the total power (see Sect. 8.3), the RF power radiated away or dissipated in the Cu cage and the ferrites amounts to typically 20%.

Table 4: Power removed from the plasma generator per cooling circuit, for two different power measurements. The values for P_{diss} correspond to the pulsed values.

Cooling circuit	$P_{RF} = 20$ kW		$P_{RF} = 40$ kW	
	P_{diss} [W]	% of total	P_{diss} [W]	% of total
Antenna	3030	15.15%	6105	15.26%
Injection	339	1.69%	684	1.71%
Plasma chamber	8681	43.41%	20528	51.32%
Extraction region	1203	6.02%	2693	6.73%
Sum	13253	66.26%	30010	75.03%
Sum (without antenna)	10223	51.11%	23905	59.77%
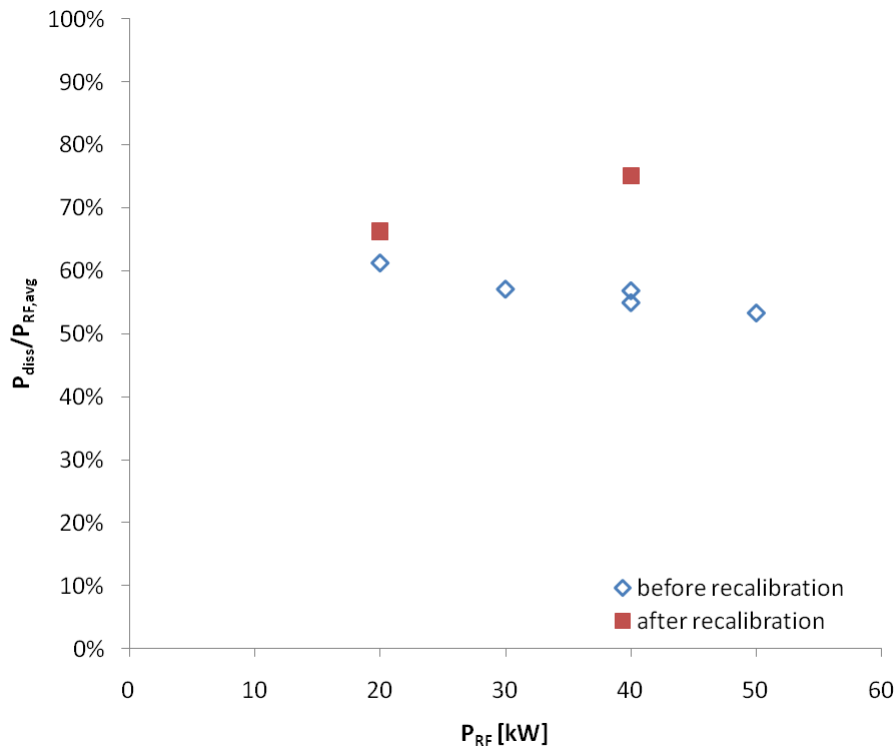
Figure 59: Development of the measured coupling efficiency $P_{diss}/P_{RF,avg}$ before and after calibration of the RF system.

6.1.3. Results from thermal imaging

The thermal camera is used for monitoring the temperature of the Cu magnet cage and the ferrites, and for the collar region. Measurements of the collar region are only performed during runs where the Germanium window was installed at the flange on the opposite side of the plasma generator. Typically, the development of the temperature is monitored over a period of several tens of minutes per RF power

50

setting in order to allow the temperatures of the components to stabilize. The temperature of the collar AlN disk, aperture electrode, and the collar SS clamp are obtained through the Germanium window. The emissivities ε of the latter three components are estimated as 0.9, 0.13 and 0.4, respectively.

The results of the temperature measurements performed so far are summarized in Table 4 for various forward RF powers. In all cases, the equilibrium temperatures are obtained for a duty factor of 6%. Open symbols correspond to measurements performed before recalibration of the RF system, filled symbols to measurements performed after recalibration.

The graph shows that the temperatures of the components rise approximately linearly with the RF power. A surprising result of the measurements is the unexpectedly large temperature gradient between the brazed collar region and the adjacent stainless steel components. Subsequent studies of the collar region with a thermal ANSYS model showed that such temperature gradients could only be achieved for the case of weak thermal coupling between the involved parts. This is a particular problem as a linear extrapolation of the available data suggests that collar temperatures could reach almost 500 °C for 100 kW operation, which is beyond the maximum operating temperature of the brazing ($\approx$ 400 °C) (Figure 60). This observation implies that the thermal contact conductances between the brazing region, the Cu adapter plate, and the stainless steel cover is considerably lower than expected and should be improved. Checking the tolerances indeed identified a 0.1 mm gap that could explain this observation.
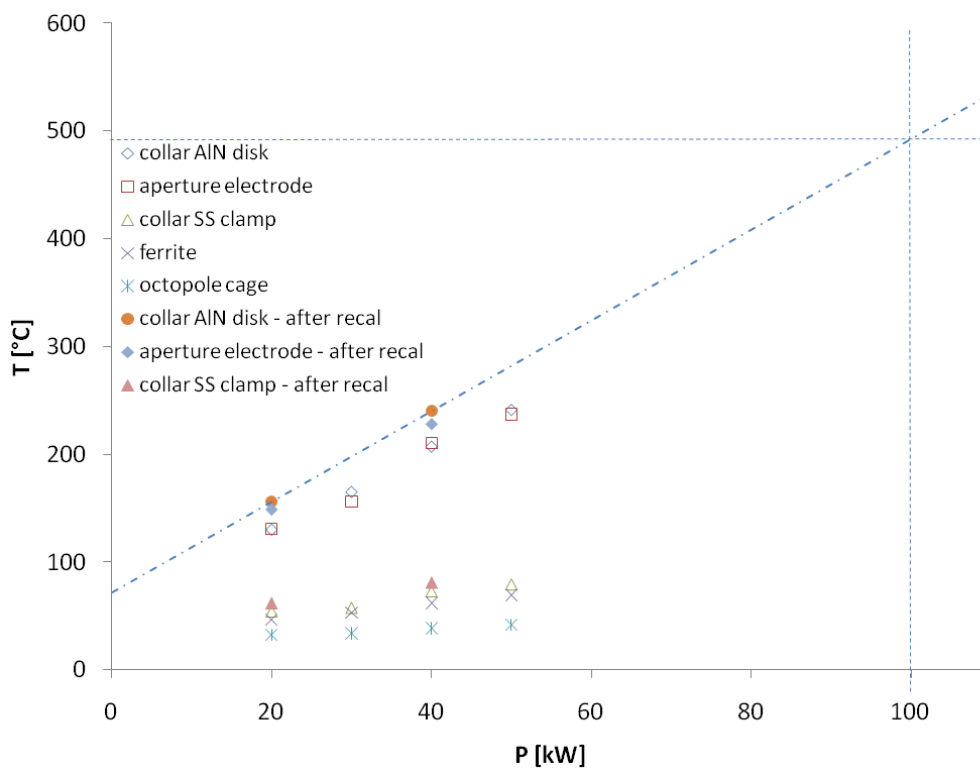
Figure 60: Equilibrium temperatures of different plasma generator components. Open symbols: measurements before recalibration of the RF system. Filled symbols: measurements after recalibration.

6.2. RF-induced Eddy currents on magnets and ferrites

Electromagnetic simulations of the SPL plasma generator performed previously with the FEM program Vector Fields Opera suggest ohmic losses of several tens of watts in the NdFeB cusp and filter magnets for a peak antenna current I_{peak} of 350 A [6,7]. Without any countermeasures, these high ohmic losses would likely result in magnet temperatures above their Curie temperature T_{Curie}. Some power is also expected to be dissipated in the ferrites because of hysteresis losses but could not be modeled at the time the previous report was issued. It should also be noted that extrapolation to 100 kW from the measurements at the SPL plasma generator test stand suggest a even higher I_{peak} between 450 A and 480 A, which would increase ohmic losses even further by a factor of almost two. Therefore, efficient ways to reduce the dissipated power are mandatory in order to operate the plasma generator at 100 kW.

In [6,7], it was shown that shielding the magnets with Cu could help to decrease the dissipated power by one order of magnitude. In order to validate this hypothesis experimentally, two NdFeB cusp magnets – one enclosed in a Cu box, one unprotected – were installed on the RF heating test bench (Sect. 3.9) and their temperatures recorded for different RF power settings. To estimate the hysteresis losses in the ferrites, one 4L ferrite and three stacked 8C11 ferrites of the geometry used in the SPL plasma generator were also tested. The temperature of all components was monitored with the thermal camera during the tests. As in the measurements performed with the SPL plasma generator, the monitored surfaces were partly painted black with the same of paint in order to create surfaces with known and uniform emissivity. The emissivity of the ferrites was measured by means of a water bath and was also found to be close to 0.8.

The RF matching network did not include water-cooling at the time the experiments were conducted, so the antenna current was kept below 200 A during high duty factor runs in order to keep the temperatures of the matching network in an acceptable range. The experiences gathered during these measurements triggered the re-design of a water-cooled RF matching network (Sect. 3.6).

6.2.1. Ferrite heating tests

The ferrite heating tests were conducted for a pulse length of 1 ms and an antenna current of 174 A at the start of the experiment, corresponding to 36% of the current expected for 100 kW operation. The measurement strategy consisted in starting with 1 Hz operation and then increasing the pulse frequency stepwise to 2, 5, 10, 20, and finally 25 Hz as soon as the ferrite temperature reached an equilibrium value. It is noted that during all measurements, the antenna current showed a pronounced decrease with time in spite of initial matching (Figure 61). This decrease is most likely to be related to the variation of the parameters matching network and the ferrites contribution to the load as a function of their temperature.

Figure 62 shows a thermal camera image of the test setup comprising the two types of ferrites. Both types of ferrites are found to heat up significantly during the RF heating tests. Figure 63 shows the time development of the ferrite temperature during the tests. The ferrite temperature does not increase linearly with the repetition rate but flattens more and more with increasing repetition rate. A major part of the effect probably comes from temperature induced demagnetization of the ferrites. In fact, the temperatures observed at 25 Hz operation are close to the Curie temperatures T_C of the materials reported by the producer [11].
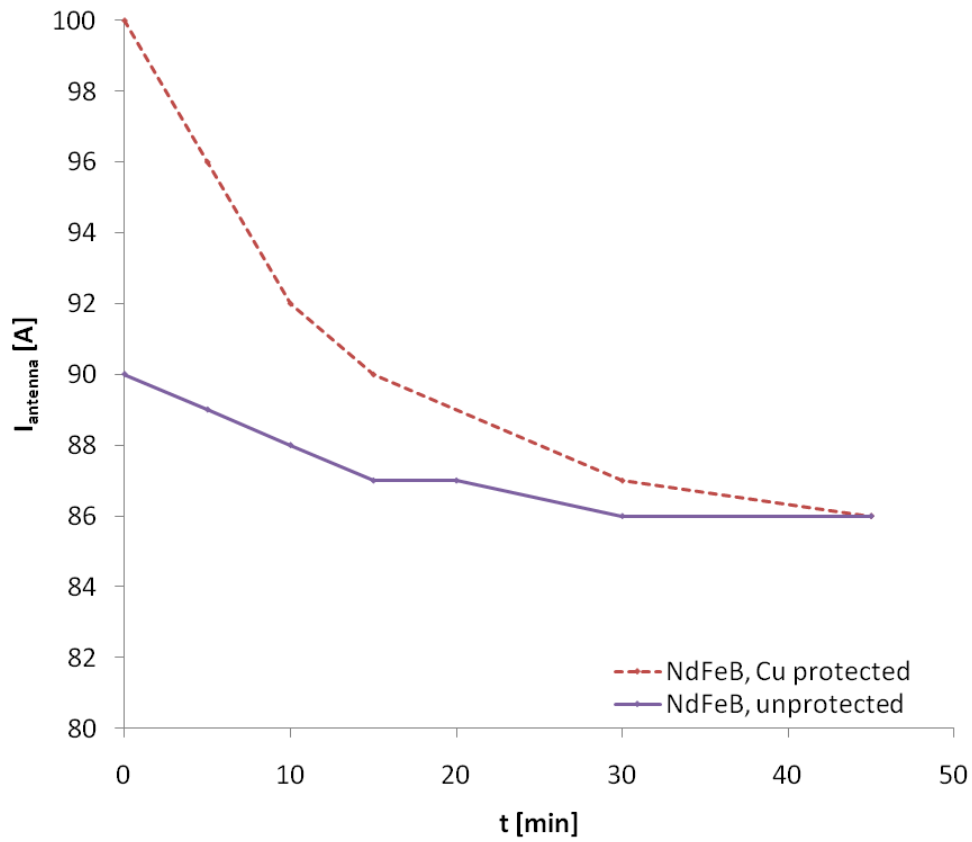
Figure 61: Time development of the antenna current $I_{antenna}$ during two measurements with the unprotected and the Cu protected NdFeB cusp magnet.
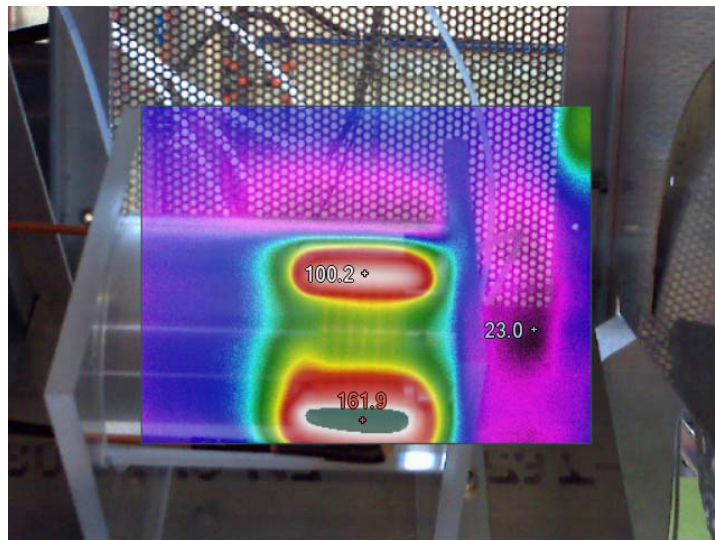
Figure 62: Thermal camera image of the RF heating test bench. Top ferrite type 8C11. Bottom: ferrite type 4L.
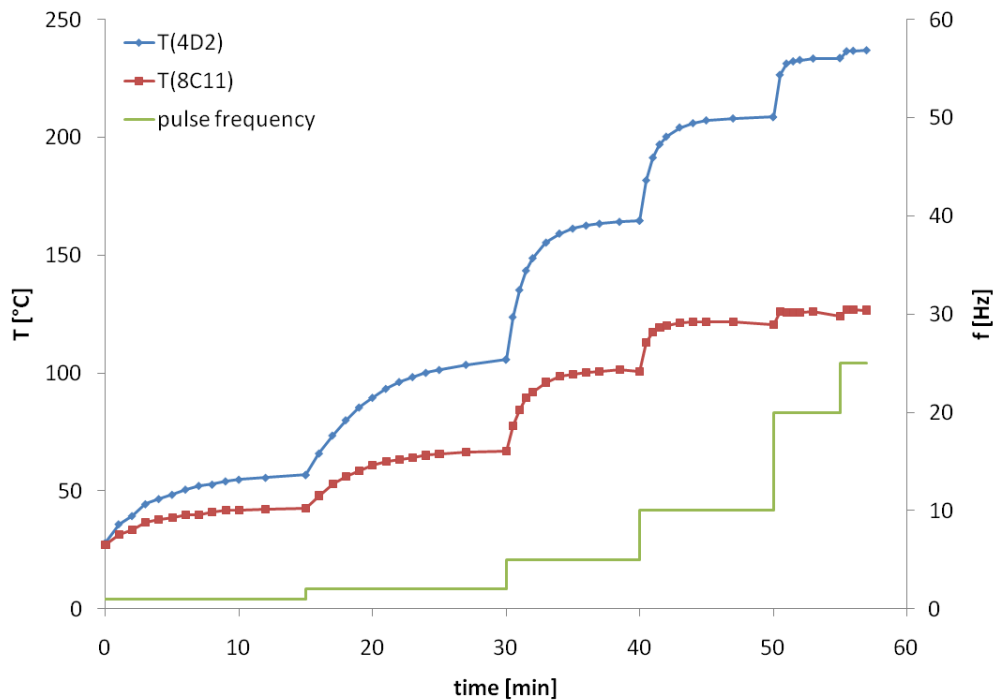
Figure 63: Time development of the temperatures of 4L and 8C11 ferrites during the RF heating test. The green line shows the development of the pulse frequency during the measurements.

6.2.2. Magnet heating tests

The magnet heating tests were conducted for a pulse length of 1 ms and a repetition rate of 50 Hz. For both the unprotected and the Cu protected magnet, measurements were performed for three different initial settings of $I_{antenna}$. As before, a decrease in the current was observed during each measurement.

Figure 64 shows typical heating up curves for the unprotected and the Cu protected magnet. During both measurements, the antenna current dropped from an initial value of 90 to 100 A to a value of I_{eq} = 86 A when thermal equilibrium was reached. The graph shows that, as predicted in the work presented in [6], the Cu protected magnet exhibited a much lower equilibrium temperature than the unprotected magnet. The same trend is also seen for I_{eq} = 67 A and I_{eq} = 120 A (Figure 65).

6.2.3. Magnetic field measurements vs. RF heating

Figure 65 shows that the temperature of the unshielded magnet is above the maximum operating temperature of the used type of magnet (Vacodym 633HR; T_{max} = 110°C [12]) for $I_{antenna}$ > 70 A. In order to assess the temperature induced magnetic losses, the magnetic field was mapped before and after each eddy current induced heating test, after the magnet had cooled to room temperature. The field mapping was performed with the magnet measurement bench presented in Sect. 3.8. Figure 66 a-d compare the inital B-field strength along the z-x plane of the magnet with those measured after each thermal cycle. In each case, the Hall probe tip was positioned 5.5 mm above the magnet surface.
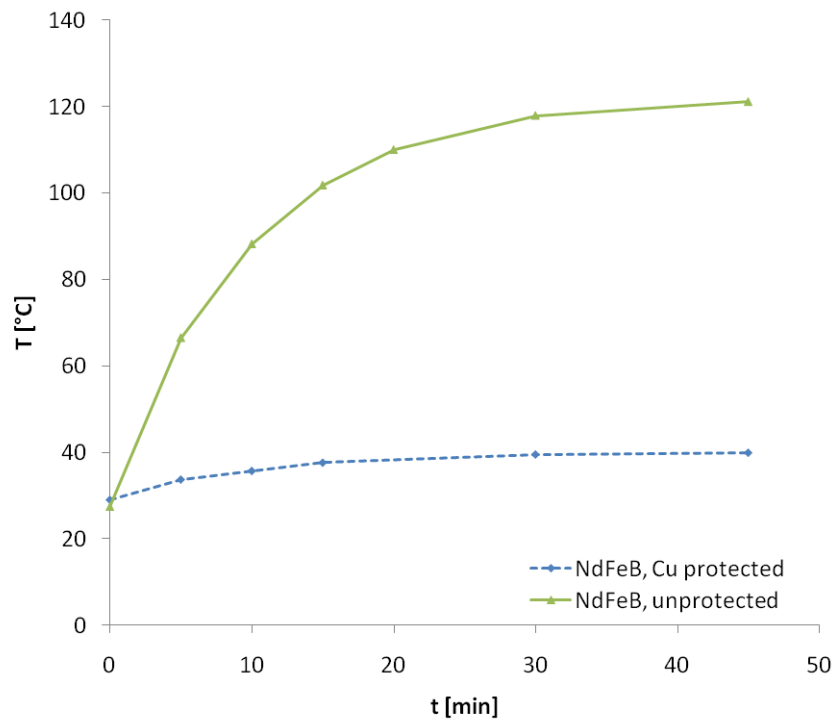
Figure 64: Time development of the surface temperatures of the unprotected and Cu protected NdFeB cusp magnet. In both cases, $I_{antenna}$ = 86 A at equilibrium.
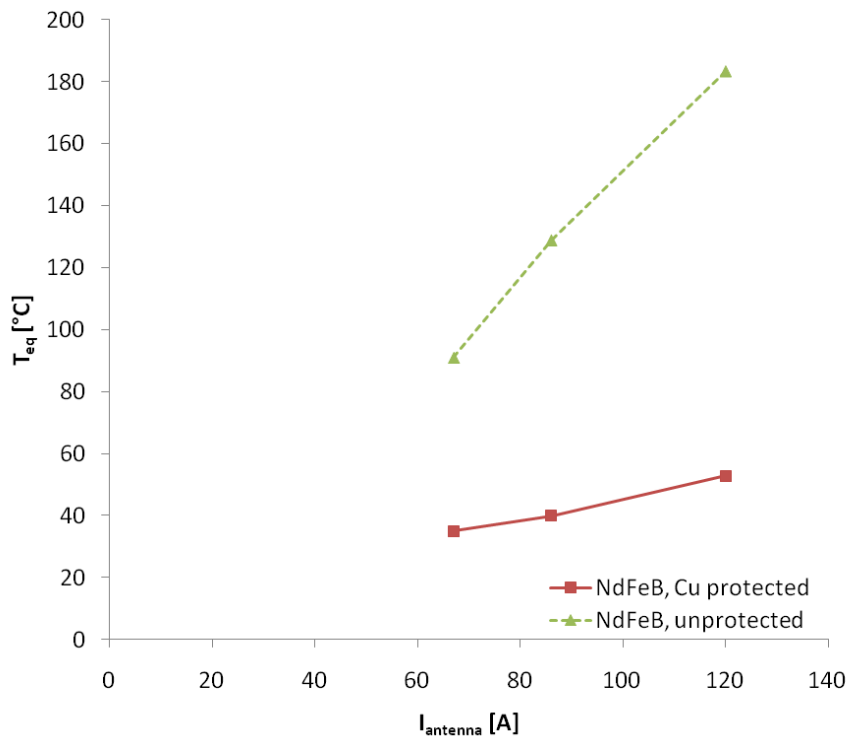
Figure 65: Equilibrium surface temperatures observed in the unprotected and the Cu protected NdFeB cusp magnet for different antenna currents. In both cases, $I_{antenna}$ corresponds to the antenna current measured after temperature stabilization.

No changes in the B-field are evident for magnets subjected to T_{eq} = 91°C (Figure 66 b). For T_{eq} = 129°C, no significant changes of the field strength are observed at the front and the back end of the magnet, however a decrease of more than 10% is detected in the center. Finally, for T_{eq} = 183°C the field strength has decreased over the whole magnet by about 50% of the initial value. This demonstrated the necessity of the Cu shielding implemented in our multicusp system.
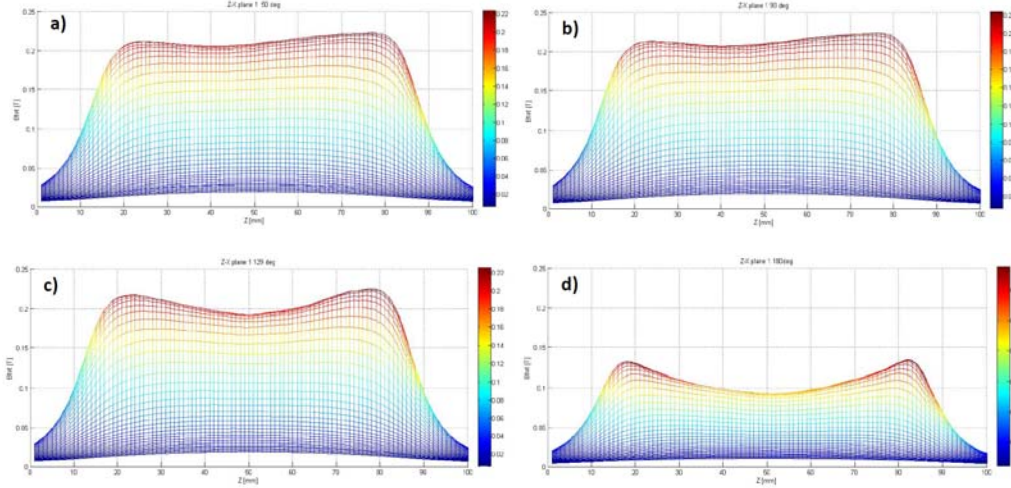
Figure 66: Degradation of the B-field strength with the equilibrium temperature. a) before the measurement. b) after heating up to T_{eq} = 91°C. c) after heating up to T_{eq} = 129°C. d) after heating up to T_{eq} = 183°C. Identical scales are used for each plot.

6.2.4. Comparison with thermal and electromagnetic modelling

The results of the measurements are used as input data for thermal and electromagnetic finite element models of the RF heating test bench. The power dissipated in the magnets and ferrites is estimated by a thermal model using ANSYS Workbench (Figure 67). For the ferrites, it is assumed that the power is dissipated uniformly in the whole volume. For the magnets, a surface heat load is applied in order to simulate the exponential decay of the ohmic losses with increasing depth inside the material. The test stand components are assumed to be cooled by heat sinks at the front and back ends of the PMMA cylinder and at the antenna, by emission of thermal radiation, and by convective air cooling. The radiative heat transfer coefficient h_r is modeled by the expression

$$h_r = \varepsilon \cdot \sigma \cdot (T - T_0) \cdot (T^2 + T_0^2)$$

(2)

Where σ = 5.67·10⁻⁸ W/m²K⁴ is the Stefan Boltzmann constant and T and T_0 are the surface and environmental temperatures, respectively. For modeling the convective heat transfer coefficient h_C, a laminar thin-layer model from [13] is used:

$$h_C = \frac{k}{L} \cdot Nu_L$$

(3)

where k is the thermal conductivity of air, L the length of the surface, and Nu_L the Nusselt number for laminar flow,

$$Nu_L = A \cdot \bar{C}_l \cdot (Ra \cdot \sin\theta)^{1/4}$$

(4)

A is a geometry-dependent constant (A = 1 for a flat surface, = 0.773 for a cylinder), $C_l \approx 0.5$ a function of thermal diffusivity α and kinematic viscosity v of air, θ the surface inclination, and Ra the Rayleigh number,

$$Ra = \frac{\rho^2 \cdot g \cdot \beta \cdot \Delta T \cdot L^3 \cdot C_P}{v \cdot k}$$

(5)

with the air density ρ, expansion coefficient β and specific heat capacity C_P, and the gravitational acceleration g. Wherever possible, temperature dependent specific heat capacities and thermal conductivities of the materials are used, otherwise constant literature values for room temperature are used. Thermal contact conductances are calculated by the model of Cooper et al. [14], assuming a pressure $P = m \cdot g \cdot sin\theta/A$, where *m and A are the mass of the body and the area of the contact surface, respectively.*.

The electromagnetic model (Figure 67) is used for validating the values of P_{diss} following from the thermal model for the unprotected and Cu protected magnets. Since the hysteresis losses in the ferrites cannot be calculated with the standard Opera licenses available at CERN, a special license (DEMAG) was purchased in order to be able to conduct these calculations and study the demagnetization of the ferrites during the heating up phase.

The thermal model was validated by means of transient simulations. For the model containing the magnet, both the heatup and the cooldown phase were modeled. For the ferrites, only the cooldown phase was modeled because of the expected nonlinearity between the antenna current and the hysteresis losses during the heating up phase. The curves yielded by the transient model were then compared by the experimentally observed development of the temperatures. For the modeling of the magnet heatup, a time-dependent heat load proportional to $I_{antenna}^2$ was used to simulate the changing $I_{antenna}$ during the measurements [15].

The simulated heatup and cooldown curves are compared to their experimental counterparts in Figure 68 a-d. The figures show that the simulations reproduce the experimental values very well, illustrating the validity of the thermal model.

Figure 69 shows the power dissipated per ferrite required to produce the temperatures observed experimentally at the different repetition rates. Clearly, the curves exhibit the expected pronounced nonlinear behavior. As noted before, this nonlinearity is a consequence of demagnetization of the ferrites with increasing temperature. The curves also show that the power losses in the 8C11 ferrites are lower than for the 4L ferrites, in agreement with expectations from the hystereses of both materials.
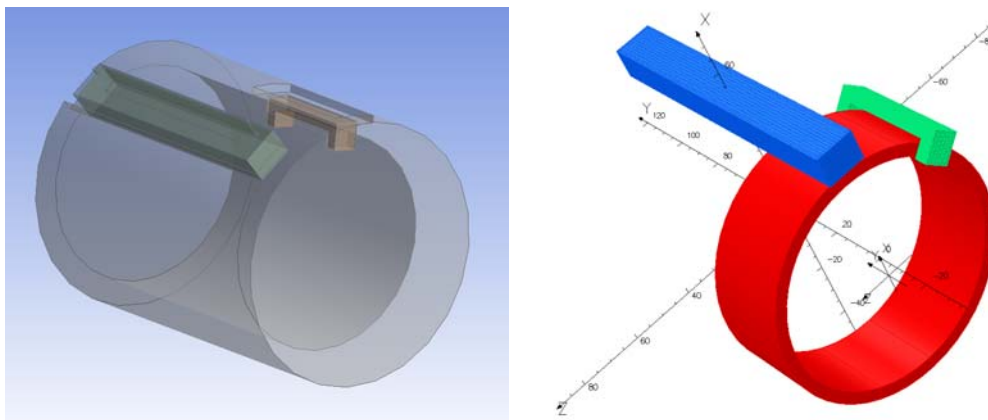
Figure 67: Finite element models of the RF heating test bench. Left: ANSYS Workbench thermal model. Right: Vector Fields Opera electromagnetic model.
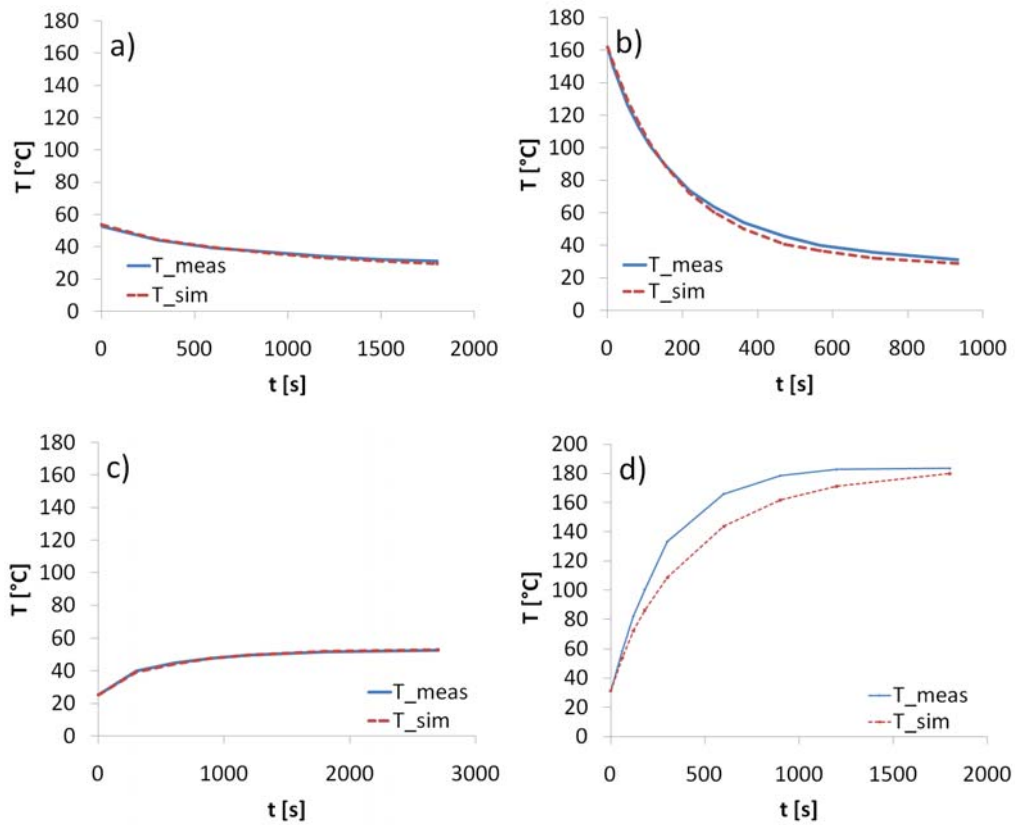
Figure 68: Comparison of simulated and measured heatup and cooldown curves. a) cooldown of Cu protected NdFeB magnet. b) cooldown of 4L ferrite. c) heatup of Cu protected NdFeB magnet. d) heatup of unprotected NdFeB magnet.
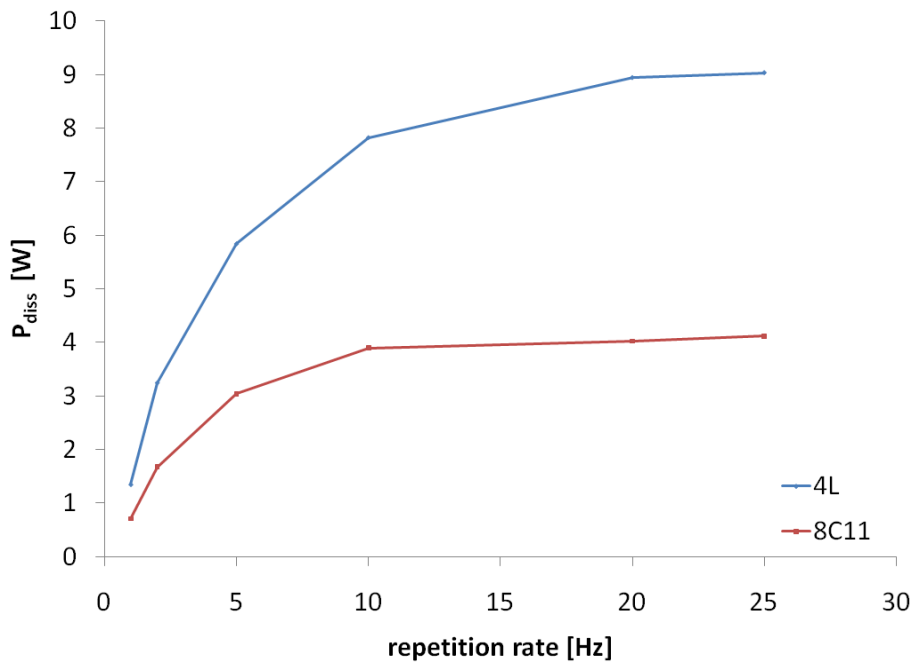
Figure 69: Power dissipated per ferrite for different repetition rates.

Figure 70 shows the power dissipated in the magnets that is required in order to reach the observed temperatures. The given antenna currents correspond to those observed after thermal equilibrium had been reached. The graph shows that the power dissipated in the Cu shield is five times less than the power dissipated in the unprotected magnet, again exhibiting the positive effect of the Cu shielding. However, a comparison with the electromagnetic model shows that the power levels expected from the Opera simulations are lower by a factor of four or five. The reason for this discrepancy is to be investigated.
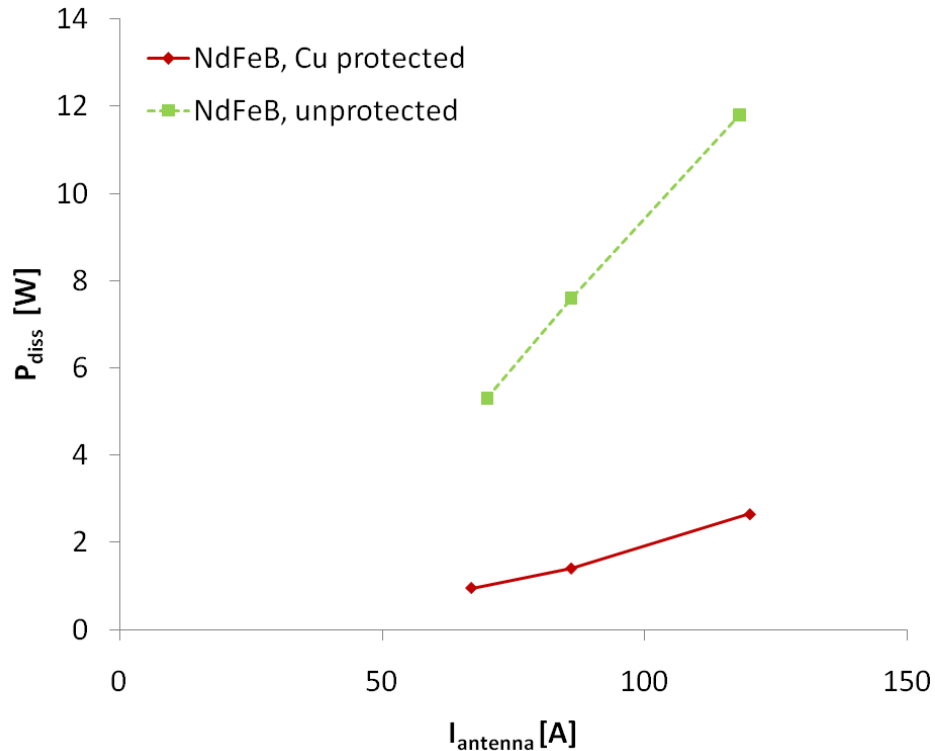
Figure 70: Required power dissipated per ferrite in order for the thermal model temperature to match the measured value, for different antenna currents $I_{antenna}$.

7. Analysis of the gas dynamics

To estimate the expected gas load for the pumping system an analytical conductance model has been used [16]. Knowing the input and output hydrogen pressure and the size of the opening channel in the Piezo valve makes it possible to estimate the gas throughput per pulse depending on the gas conductance of the opening channel. The gas channel of the Piezo valve is disk shaped. The gas is flowing radially from the outside towards the center of the disk where it leads into an outflow pipe. This disk-shaped channel can be approximated by a series of rectangular ducts of decreasing width. The height of the channel corresponds to the movement measured with a Laser vibratometer and varies from 0 to 11 μm (at 110 V maximum) following the modulated voltage signal applied to the valve. From this, it is possible to calculate the time dependent conductances. Assuming a 500 μs long gas pulse, an input pressure of 1350 mbar and a neglectable output pressure, the model yields a gas throughput per pulse of $3.7 \cdot 10\text{-}3$ mbar·l.

From the geometry of the system it is possible to calculate the molecular and viscous gas conductances of each connection between the components of the vacuum system. Namely: a virtual chamber on the vacuum side of the Piezo valve (which is

actually just a small tube), the electron gun volume, the plasma chamber, and the vacuum tank (Figure 71). The molecular gas conductances of the piping and orifices which connect these four chambers are calculated as proposed by ref. [16], yielding 0.042 l/s, 0.261 l/s and 3.98 l/s for C1, C2 and C3 respectively. These values comprise approximations for conical ducts to act as a series of short ducts and orifices. Calculated conductances are only valid in the molecular flow regime, which is the main domain of the system. Nonetheless a combination of molecular and viscous conductances was used, which results in pressure dependent conductances, to maintain accuracy even for higher pressures.
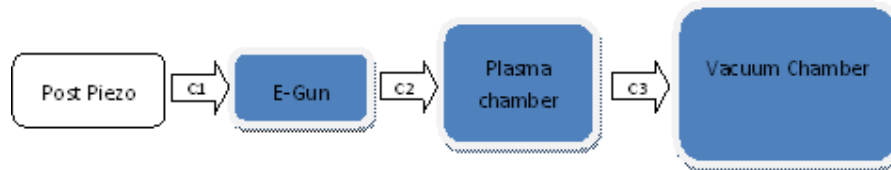
Figure 71: Scheme of the analytical model. The respective total molecular conductances of C1, C2 and C3 are 0.042 l/s, 0.261 l/s and 3.98 l/s.
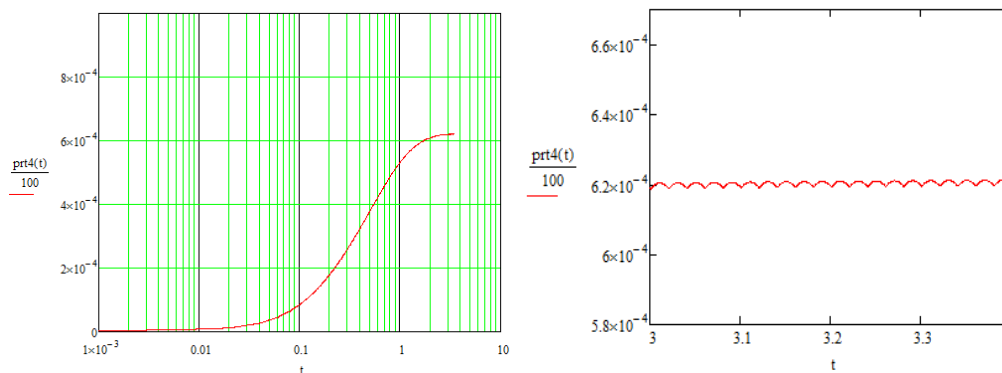
Figure 72: Calculated pressure rise in the main vacuum chamber when the source is set to 50 Hz repetition rate (left) and the pulsing pressure signal in the vacuum chamber after equilibrium was reached (right). In both cases, pressure values are in mbar.

Knowing the gas input from the Piezo valve it is possible to calculate the propagation of the gas pulse through the vacuum system and the resulting pressure curves in the four introduced chambers. Figure 72 shows such a calculated pressure as a function of time, for the vacuum chamber. The abscissae give the pressure in mbar. The left curve shows typical behavior at the start up of the gas injection and indicates that after a few seconds of 50 Hz operation, equilibrium is already reached. The right curve exhibits the pressure fluctuations for equilibrium conditions. Note that single pulses can be easily distinguished in the calculated results whereas measurements are superposed by massive noise (Figure 73).

From the results of the simulations, the average gas load for 50 Hz operation is estimated to be 0.186 mbar l/s for which the pumping system was designed. A TMU521 turbo molecular drag pump (Pfeiffer Vacuum - 450 l/s for H_2), backed by a TMU071 turbo molecular drag pump (Pfeiffer Vacuum - 42 l/s for H_2) and an Edwards 12 m^3/h mechanical forepump, controlled with a single pumping control unit (CERN-PS-standard), are chosen to take the gas load.

The maximum throughput of the vacuum pumps (Figure 74) is 9.5 mbar l/s (TMU521) and 0.58 mbar l/s (TMU071) N_2 at nominal speed, which is well above the injected gas flow. At first consideration, this pumping system should therefore have been sufficient to cope with the imposed gas load. However, measurements revealed that

60

the average pressure observed during 50 Hz operation was $6.4 \cdot 10^{-3}$ mbar (CMR 375) although a pressure of $4 \cdot 10^{-4}$ mbar was expected. A detailed analysis showed that during a gas pulse, the pressure in the vacuum chamber can reach such high values that the pumping power starts deteriorating. Using of the TMU071 in series of the TMU 521 yielded a 35% decrease of the maximum pressure for 1-2 Hz injections, however with higher repetition rates no significant improvement could be detected (Figure 73). Accordingly, the pumping system was upgraded to a version comprising two TMU521 turbo molecular drag pumps backed with single Edwards $12 m^3/h$ forepumps. Doubling the pumping power resulted in a decrease of maximum pressure to $1\text{-}2 \cdot 10^{-3}$ mbar, corresponding to a reduction by a factor of four. A third TMU521 could be added to maintain a stable pressure regime throughout the gas pulse.
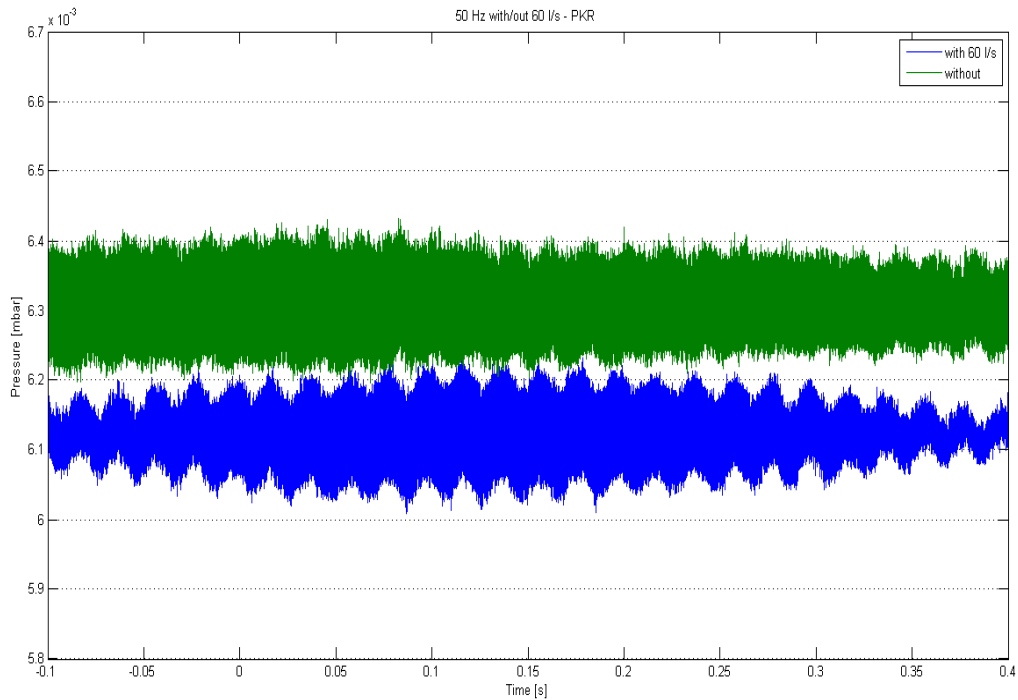
Figure 73: Pressure in vacuum chamber at 50 Hz repetition rate with (blue) and without (green) TMU071 backing pump.

Figure 74: Left: TMU521 turbo molecular pump backed with a TMU071 turbo molecular pump.. Right: Edwards 12 roughing pump.

In order to reduce the amount of gas injected per pulse to a minimum, a new gas injection scheme has been tested. By optimizing the timing between the gas and RF pulses and the ignition spark (Figure 75), stable plasma operation was achieved for gas pulses as short as 188 µs. However, it should be noted that the gas amount is also strongly affecting the RF-plasma coupling. For this reason, a full optimization of the system can only be achieved with parallel optical emission and light intensity measurements and RF reflected power determination.
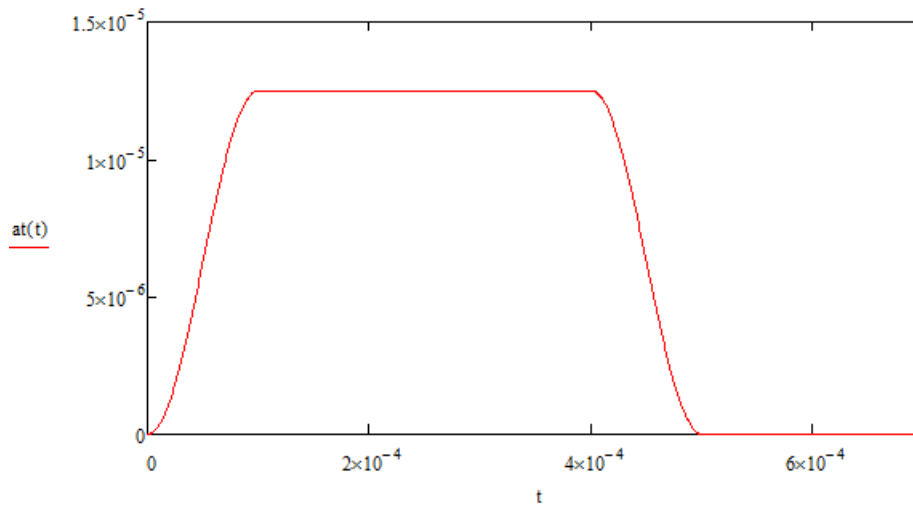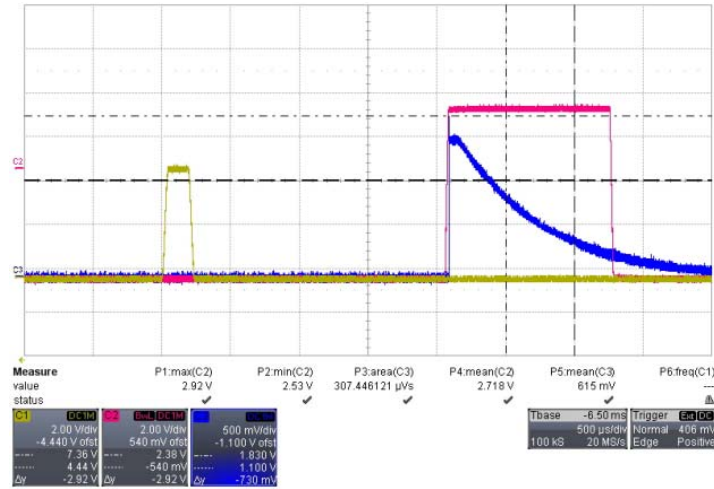
Figure 75: Top: Standard timing of gas pulse (yellow), the ignition voltage (blue), and the RF pulse (red). Bottom: opening of the Piezo channel in meters over time, actuated with a sine like rise and fall for protection of the Piezo valve while the plateau length determines amount of gas injected, the amplitude is generally set to a maximum of 110 V.

8. Characterization of the plasma impedance and resistivity

The RF generator used at the SPL plasma generator test stand (see Sect. 3.7) can provide up to 100 kW power in an 2 MHz RF signal, but not all of the power is actually coupled to the plasma and therefore used for plasma heating. A fraction of the forward power are always reflected back to the RF generator if there is a mismatch between the matching network impedance to the 50 Ω Impedance load expected by the RF generator.

The matching network impedance depends critically on the plasma which, when ignited, acts as a serial impedance that changes the matching conditions. Moreover, if the source settings are changed (e.g. the amount of gas injected per pulse or the timing for the RF pulse), the matching will be affected again. It is thus important to measure the coupling on a continuous basis.

8.1. PSpice simulations

In order to make sure that the behavior of the matching network is well understood a PSpice simulation of the circuit was performed and compared with data measured with a network analyzer (Figure 76). The measured resistances, capacitances and inductances of the RF circuit components (see Table 3) have been fitted to PSpice simulations. As shown in Figure 76, the simulated and measured impedance curves are almost congruent.
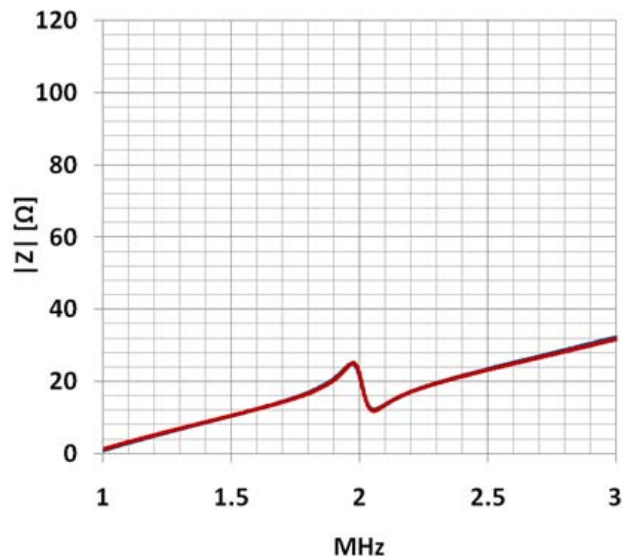
Figure 76: Matching network impedance, comparison of measurement at directional coupler (red) and PSpice simulation (blue).

8.2. Description of Method

During source operation, three measurements are performed simultaneously: The forward and reflected voltages are both monitored at the directional coupler. The antenna current is measured using a Pearson Model 150 current transformer. The full voltage signals are divided into user defined intervals. A preset of 2 RF periods was chosen, which allows an analysis of each interval similar to a windowed Fourier analysis. This setting allows a coupling analysis every 1 µs and, at the same time, leaves enough measurement points per window to assure an accurate analysis. prepared script was written to evaluate all parameters at the actual RF frequency. The absolute value of the forward/reflected voltage Fourier spectrum at the preset frequency corresponds to the voltage amplitudes, whereas the ratio between the real and imaginary parts reflects the tangent of the phase angles.

Amplitude and respective phase angle of the voltage signals can be used to obtain the overall impedance of the circuit as well as forward and reflected power. As the circuit and its components are well measured at low power it is possible to calculate back to the plasma inductance and resistance. Deducting antenna and matching network resistance again yields the plasma resistance. The phase relations of the forward and reflected voltages show if stable conditions apply during a pulse.

For the RF coupling analysis, online and offline measurements have been implemented. The online script continuously reads out the scope and evaluates the data approximately every 30 seconds. It is also possible to store interesting traces directly on the scope to analyze them with the offline script.

8.3. Results

Figure 77 shows typical plots produced by the offline analysis tool. The top graphs show the measured amplitudes of forward and reflected power and the antenna current, the graphs at the bottom the calculated phase angle between forward and reflected power and the plasma resistance, once derived from the forward and reflected voltages and once from the antenna current. All calculated values exhibit a drift during the pulse, reflecting slight changes of the plasma impedance and resistance.
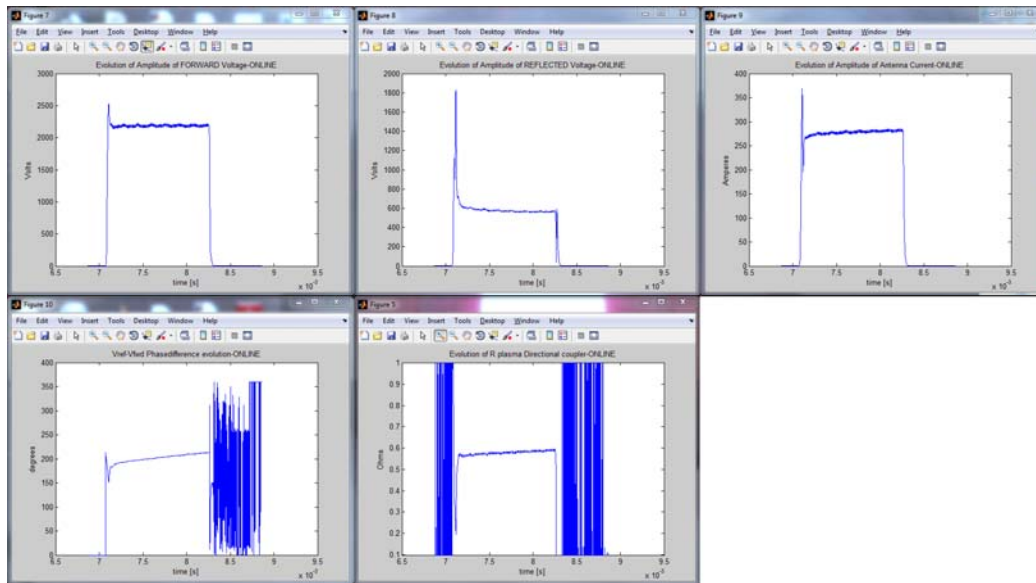
Figure 77: Typical output of the RF coupling analysis. The top graphs show the measured amplitudes of forward and reflected voltage as well as antenna current. The bottom graphs show analysis results as phase angle between the forward and reflected voltage and the plasma resistance calculated from the forward and reflected voltages.

Figure 78 shows the forward and reflected power for an optimally matched system and for 48 kW forward power. Once the plasma is stabilized after the ignition phase, only 6-10 % of the power are reflected which proves an excellent impedance matching.

Certainly the aim of the matching is to guide as much power as possible into the plasma in a stable and controlled way. Although for the above measurement over 90 % of provided power is dissipated in the circuit, only a fraction is dissipated in the plasma. Figure 79 compares the forward power with the power dissipated in the plasma for the plasma resistance calculated from the forward and reflected voltages. 43 - 28 % of the forward power is dissipated in the plasma, which shows that the coupling can still be improved.
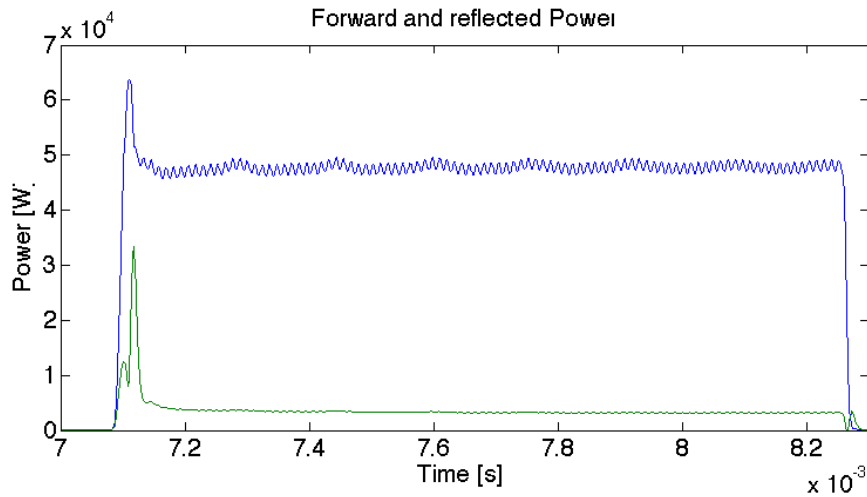
Figure 78: Forward and reflected power calculated from directional coupler measurements for an optimally matched system.
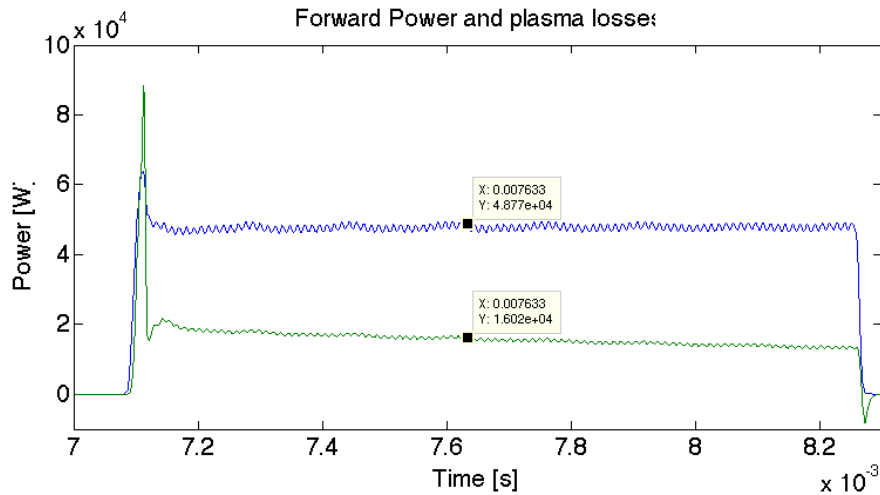
Figure 79: Forward power and power losses in the plasma calculated through plasma resistance and antenna current.

9. RGA measurements

The rest gas inside the vacuum chamber was analyzed by a quadrupole mass spectrometer QMA 125 from Pfeiffer. Figure 80 shows preliminary results on the ion current of the different species for two different situations: spectrometer volume separated from the main vacuum (RGA curve) and spectrometer volume connected to the vacuum chamber (vacuum chamber curve). The measurement was obtained one week after the plasma generator had been operated for the last time. An analysis of the rest gas during plasma generator operation is scheduled. The vacuum pressure of the spectrometer volume is slightly higher than that inside the vacuum chamber (6.3×10^{-8} mbar rather than 4.9×10^{-8} mbar).
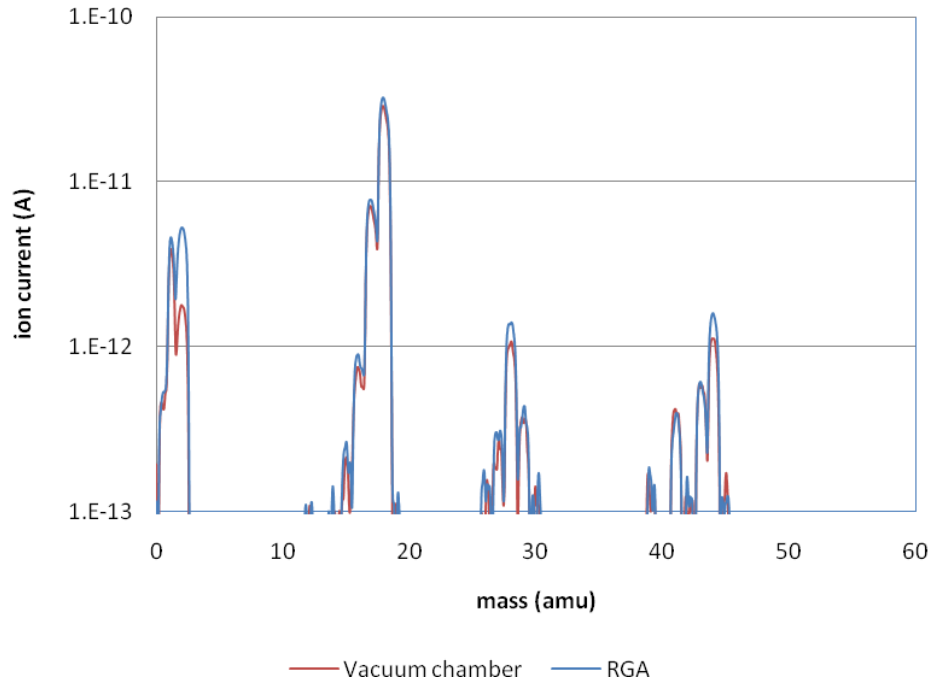
Figure 80: Rest gas analyzer spectrum of the vacuum chamber.

Table 5 summarizes the different detected species and their respective ion current intensity. The error corresponds to the normalized difference between the measured mass and the known mass of the probable detected element.

The predominant particle species inside the vacuum chamber is H_2O followed by OH and H. Other clearly identified molecules are CO_2, N_2 and H_2 and traces of Ar from the injection gas. More interestingly, it is possible to recognize the presence of Al, AlN and AlO as a result of the decomposition of the ceramics plasma chamber. Other species are present in smaller amounts.

Table 5: Gaseous particle species identified with the RGA inside the vacuum chamber, and their respective ion current intensity.

Mass of detected species (amu)	Ion current intensity ($\times 10^{-12}$ A)	Detected species
1.16	3.939	H
2.00	1.800	H_2
12.13	0.109	C
14.09	0.101	N
15.94	0.760	O
16.92	7.198	OH
17.92	29.060	H_2O
28.02	1.075	CO / N_2
39.23	0.131	Ar
44.00	1.129	CO_2

10. Proposal for a high flux hydrogen pumping system

In some applications H_2 is injected locally in the vacuum systems of particle accelerators; for example this is the case in proton sources and antimatter experiments. The large majority of the injected gas is not used for the intended process and, as a consequence, must be pumped to preserve the vacuum in the nearby beam pipes.

The traditional pumping solution consists in evacuating the gas by turbomolecular pumps. Indeed, this approach has the advantage of removing definitively the gas from the accelerators; in addition it offers high pumping rates at relatively high pressures, about 10^{-1} mbar.l.s^{-1} at 10^{-3} mbar respectively. Such pumps are in general installed very close to the gas source. The gas escaped from the first stage of pumping is generally trapped by ion pumps. Unfortunately this solution is far to be optimized. In fact, only a fraction of the gas molecules are intercepted by localised pumps, the rest being transmitted in the beam pipe, missing the pump aperture. In addition, hydrogen removal by ion pumps is not efficient (low sputtering rate by H_2 ions) and leads to hydride formation, which provokes cathode expansion and eventually short circuits and pump failure.

A better solution would consist in installing a distributed pump along the beam pipe, just after the first stage of mechanical pumping, as it would capture the gas much more efficiently. A feasible pumping technique that guarantees such implementation is surface chemical adsorption, namely getters and above all non-evaporable getters (NEG). After thermal activation in vacuum, such materials can absorb hydrogen up to a quantity limited by the bulk hydride formation. The main requirements to provide an ideal pumping at room temperature are:

- high hydrogen solubility
- low hydrogen dissociation pressure (possibly in the high-vacuum range)
- high hydrogen diffusivity
- high sticking probability, namely high pumping speed.

These characteristics are not entirely fulfilled by a single element. Elements of the 4th group, in particular Zr which is the common base for NEG material, have a very low dissociation pressure, but a limited solubility in the α FCC phase, a relatively low diffusivity at room temperature and a sticking probability of about 10^{-2} for molecular hydrogen. In the 5th group, because of the BCC crystallographic structure, diffusivity is orders of magnitude higher, but the dissociation pressure is also much higher and sticking probability does not differ from the ones encountered in the nearby groups. The 10th group, in particular Pd, shows a remarkable anomaly for the sticking probability of hydrogen: values close to 1 have been measured by several authors. Unfortunately, in this group the dissociation pressure is incompatible with the needed high flux rate and high-vacuum.

For the future pumping system of the Linac4 and SPL sources a combination of different layers of transition metals is proposed. The multilayer pump would associate at each metallic stratum a different function in a way to satisfy globally the whole list of requirements. The first layer, the one in contact with the gas phase, should have the highest sticking probability and, as a consequence, a thin Pd film is the obvious choice. The use of Pd alloys could be necessary instead of pure Pd. In fact, this catalyst is known to have a deep energy well for atomic hydrogen onto its surface. This results in pile up of gas on the surface and obstacle to the gas transfer into the material bulk, with the inevitable increase of the dissociation pressure. The potential well can be levelled off by the addition in Pd of other elements, for example Ag.

Once hydrogen atoms have entered the metal, they have to be removed as fast as possible from the surface. In this respect, V is the right choice since at room temperature it has one of the highest diffusivity for H amongst the transition metals. The final storage for the H atoms could be assured by Zr, Ti or their alloys in form of sheets. It would be important to select materials that can tolerate hydride precipitation without major losses of mechanical properties.

The mandatory tests will start with the characterisation of the PdAg/V/Zr structure. Sticking probability and pumping capacity at different pumping fluxes are to be measured and the surface contamination by other reactive gases, i.e. water vapour and CO, tested. In a second step, other metals will be considered as an alternative to V and Zr. In particular, the structure, texture and grain size of the H storage metal will be considered. The regeneration of the hydrogen pump by heating will also be studied as the kinetics of hydrogen desorption at different heating temperatures. Finite element calculations will help with the interpretation of the experimental results.

11. Conclusions and Outlook

The sLHC-pp 7.1 project is completed, all deliverables were met. An operational plasma generator was successfully produced and tested. The plasma generator was extensively operated at low repetition rate up to the nominal 100 kW peak RF power and at 50 Hz repetition rate up to 3 kW average power. During these tests the validity of the cooling model was demonstrated, the plasma was fully characterized via optical emission spectroscopy of hydrogen's Balmer lines with 25 µs time resolution. A method based on an electrical equivalent circuit was developed and allows the precise measurement for each RF cycle of the effective coupling of the RF into the plasma. These innovative results were published in refereed conferences.

The first prototype is promising and will be further operated to systematically study the influence of each operation parameters around its nominal value. The result is a relevant contribution to the upgrade of CERN's Linac4 ion source. The project allowed training of fellows and students. Innovative results were published and the information gathered is key input to the design of new prototypes for the Linac4 ion source.

Further studies on plasma coupling, interpretation of the optical emission spectroscopy or pulse to pulse monitoring of the plasma parameter are now possible. An innovative method to drastically improve the H_2 pumping power is proposed. The experimental results will be provided by the operational test stand that is well suited to address the challenges of Linac4 or future versions of the SPL plasma generator.

A. References

[1] D. Küchler, T. Meinschad, J. Peters, and R. Scrivens, Rev. Sci. Instrum.79 (2008), 02A504

[2] J. Peters, The HERA Volume H⁻ Source, PAC05 Conference Proceedings, TPPE001, p. 788 (2005)

[3] M. Baylac, F. Gerigk (ed.), E. Benedico-Mora, F. Caspers, S. Chel, J.M. Deconto, R. Duperrier, et.al., CERN Report No. 2006-006, (2006)

[4] J. Lettry, M. Kronberger, R. Scrivens, E. Chaudet, D. Faircloth, G. Favre, J.-M. Geisser, D. Küchler, S. Mathot, O. Midttun, M. Paoluzzi, C. Schmitzer, and D. Steyaert, Rev. Sci. Instrum. 81 (2010) 02A723

[5] E. Chaudet, D. Faircloth, G. Favre, J.-M. Geisser, M. Kronberger, J. Lettry, S. Mathot, O. Midttun, P. Moyret, C.-S. Schmitzer, R. Scrivens, D. Steyaert, Design of a high duty factor plasma generator. SLHC WP 7.1.1 Deliverable report, 09/2009

[6] E. Chaudet, A. Castel, J.-F. Ecarnot, D. Faircloth, G. Favre, F. Fayet, J.-M. Geisser, M. Haase, A. Habert, J. Hansen, S. Joffe, M. Kronberger, D. Küchler, J. Lettry, D. Lombard, A. Marmillon, J. Marques Balula, S. Mathot, P. Moyret, D. Nisbet, M. O'Neil, M. Paoluzzi, L. Prever-Loiri, J. Sanchez Arias, C.-S. Schmitzer, R. Scrivens, D. Steyaert, H. Vestergard, M. Wilhelmsson, Construction of the plasma generator and sub-systems, SLHC WP 7.1.1 Deliverable report, 09/2010

[7] M. Kronberger, E. Chaudet, G. Favre, J. Lettry, D. Küchler, P. Moyret, M. Paoluzzi, L. Prever-Loiri, C. Schmitzer, R. Scrivens, D. Steyaert, Magnetic Cusp Configuration of the SPL Plasma Generator. AIP Conf. Proc., accepted for publication.

[8] J. Lettry, S. Bertolo, A. Castel, E. Chaudet, J.-F. Ecarnot, G. Favre, F. Fayet, J.-M. Geisser, M. Haase, A. Habert, J. Hansen, S. Joffe, M. Kronberger, D. Lombard, A. Marmillon, J. Marques Balula, S. Mathot, O. Midttun, P. Moyret, D. Nisbet, M. O'Neil[a], M. Paoluzzi, L. Prever-Loiri, J. Sanchez Arias, C. Schmitzer, R. Scrivens D. Steyaert, H. Vestergard, M. Wilhelmsson, Measurement of optical emission from the hydrogen plasma of the Linac4 ion source and the SPL plasma generator. AIP Conf. Proc., accepted for publication.

[9] M. M. Paoluzzi, M. Haase, J. Marques Balula, D. Nisbet, CERN LINAC4 H⁻ Source and SPL plasma generator RF systems, RF power coupling and impedance measurements. AIP Conf. Proc., accepted for publication.

[10] U. Fantz and D. Wünderlich, New Journal of physics 8 (2006), 301.

[11] Soft Ferrites and Accessories data sheet, FerroXCube, USA

[12] Vacodym 633 HR Data sheet, Vacuumschmelze GmbH & Co. KG, Germany

[13] W. M. Rohsenow, J. P. Hartnett, Y. I. Cho (eds.), Handbook of Heat Transfer, Third Edition. McGraw-Hill (1998)

[14] M. G. Cooper, B. B. Mikic, M. M. Yovanovich, Thermal Contact Conductance. Int. J. Heat Mass Transfer 12, 279 (1969)

[15] D. Faircloth, M. Kronberger, D. Küchler, J. Lettry, R. Scrivens, Finite element thermal study of the Linac4 plasma generator, Rev. Sci. Instr. 81, 02A722 (2010)

[16] J. M. Lafferty, Foundations of Vacuum Science and Technology. NY Wiley (1998)